

THESIS

FATIGUE CRACK PROPAGATION IN UNDERWATER CARBON FIBER REINFORCED
POLYMER (CFRP)-RETROFITTED STEEL PANELS

Submitted by

Anuj Valsangkar

Department of Civil and Environmental Engineering

In partial fulfillment of the requirements

For the Degree of Master of Science

Colorado State University

Fort Collins, Colorado

Fall 2015

Master's Committee:

Advisor: Hussam Mahmoud

Guillermo A. Riveros
Frederick W. Smith
Troy Holland

Copyright by Anuj Valsangkar 2015

All Rights Reserved

ABSTRACT

FATIGUE CRACK PROPAGATION IN UNDERWATER CARBON FIBER REINFORCED POLYMER (CFRP)-RETROFITTED STEEL PANELS

Steel structures, such as hydraulic structures and ships operate in harsh wet and corrosive environments and can suffer significant deterioration. The deterioration typically manifest itself in the form of corrosion, fatigue cracking, or a combination of both. While these corruptions or cracks are typically viewed as nuisance, if left unrepaired, they can threaten the integrity of the structure. Repairing these fatigue using the conventional repair methods can be proven to not only be time consuming but also ineffective. Recent advances on the use of CFRP to retrofit structures has shown to be a viable solution for increasing fatigue life of structures made of metals such as different types of steels, aluminum, etc. Although large number of studies have been conducted to evaluate the use of CFRP for retrofitting metal alloys and the promising potential of such has been well-demonstrated, the application has been primarily focused on the aerospace and bridge industries. As a result, very few studies have been concerned with retrofitting metallic structures under wet and corrosive environments.

With the above mentioned motivations, there is a clear need to conduct studies to evaluate the viability of using CFRP to repair underwater metal structures. To this end, a new experimental setup is devised to allow for underwater testing of large-scale steel panels. The purpose of this experimental study is to provide a first-of-its-kind benchmark data by which the potential for using CFRP for underwater fatigue repairing metallic structures can be assessed. In this study, four large scale steel panels were tested, three of which repaired with CFRP patches, under different environmental conditions (three remaining to be tested for a total of seven specimens). The main

focus is evaluate the effect of CFRP on crack growth rate. Since the application in this study is pertain to water navigation structures used in rivers, the effect of fluvial sediments as well as salt are considered in the study. The use of salt allowed for accelerated corrosion in the specimens to represent actual condition of deteriorated panels. The in-air and underwater results showed an increase in fatigue life with use of CFRP in comparison to bare specimens.

ACKNOWLEDGEMENTS

I would like to thank my adviser Dr. Hussam Mahmoud for his technical guidance over the past two years without which I would have not finished the project. I would like to thank my committee members Dr. Guillermo A. Riveros, Dr. Frederick W. Smith and Dr. Troy Holland for giving their valuable insights throughout the completion of project. I would like to also acknowledge Dr. Riveros for his many visits to Colorado State University (CSU) and the structural laboratory at CSU to discuss the project progress and provide his input on ways forward.

I would like to thank my parents for their unconditional love and support throughout my life. I also would like to thank my brother Shrikant whose love and friendship kept me motivated while completing the project. I would love to thank my grandfather for his teachings.

I am extremely thankful to graduate students Mehrdad Memari, Bashir Ahmadi and undergraduate students Erick Ritter and Monica Prycel for their help in the project. I am thankful to Junior Garza and Matthew Szydlowski of Engineering Research Center facility of CSU for their tremendous and unconditional help in the structures lab.

I am grateful towards US Army corps of engineers for funding this project.

At the end I would like to thank all my friends Tejas Doshi, Akshat Chulahwat, Nikhil Naole, Anshuman Rajwar, Tushar Ganguli and Bhavik Mistry who were always there for me through ups and downs during my graduate studies.

TABLE OF CONTENTS

ABSTRACT.....	ii
ACKNOWLEDGEMENTS.....	iv
TABLE OF CONTENTS.....	v
LIST OF TABLES.....	ix
LIST OF FIGURES.....	x
Chapter 1 Introduction.....	1
1.1 Problem Statement.....	1
1.2 Objective and Scope.....	3
1.3 Organization of Thesis.....	5
Chapter 2 Background and Literature Review.....	6
2.1 Fracture Mechanics.....	6
2.2 Linear Elastic Fracture Mechanics.....	7
2.3 Strain Energy Release Rate.....	9
2.4 Stress Intensity Factor.....	10
2.5 Fatigue Category Details.....	11
2.6 Fatigue Rate Curve.....	13
2.7 Fatigue Crack Growth Rate Models.....	14
2.7.1 Constant Amplitude Fatigue Loading Models.....	14
2.7.1.1 Paris Model.....	15
2.7.1.2 Walker Model.....	16
2.7.1.3 Forman Model.....	17
2.7.1.4 Collipriest Model.....	18
2.7.1.5 Frost and Pook Model.....	19
2.7.1.6 Pugno Model.....	19

2.7.1.7 Wheeler Model.....	20
2.7.1.8 Willemborg Model.....	21
2.7.1.9 Barsom Model.....	22
2.7.2 Variable Amplitude Fatigue Loading Models.....	23
2.7.2.1 Chang, Szamossi and Liu Model.....	23
2.7.2.2 Hudson Model.....	24
2.7.2.3 Newman Model.....	25
2.7.2.4 Johnson Model.....	26
2.7.2.5 Modified Miner Model.....	27
2.8 Fatigue Crack Repair and Retrofit Methods.....	28
2.8.1 Surface Treatments.....	28
2.8.2 Repair of Through-Thickness Cracks.....	30
2.8.3 Modification of the detail.....	32
2.8.4 Repairs using Carbon Fiber Reinforced Polymer (CFRP) Composites.....	33
2.9 Literature Review.....	33
2.9.1 Crack growth in CFRP-retrofitted panels.....	33
2.9.2 CFRP debonding and development length.....	37
Chapter 3 Experimental Test Setup.....	40
3.1 Introduction.....	40
3.2 Geometric Configuration of Test Setup.....	40
3.3 Instrumentation Plan and Crack Measurements.....	49
3.3.1 CFRP installation and surface preparation.....	56
3.3.1.1 CFRP installation.....	56
3.4 Mechanical properties for CFRP and adhesive.....	59
3.5 Test Matrix.....	61

3.6 Testing Plan and Loading Protocol	62
Chapter 4 Experimental Results and Observations.....	64
4.1 Introduction	64
4.2 Test results for Individual Specimen.....	65
4.2.1 Test Results and Observations for Specimen 1	65
4.2.1.1 Strain Gauge Results for the Shakedown Tests	66
4.2.1.2 Crack Length versus Number of Cycles for Specimen 1	67
4.2.1.3 Crack Growth Rate versus Change in Stress Intensity Factor	71
4.2.1.4 Change in Strain with Half Crack Length.....	72
4.2.2 Test Results and Observations for Specimen 2	73
4.2.2.1 Crack Length versus Number of Cycles for Specimen 2.....	74
4.2.2.2 Change in Strain with Half Crack Length.....	77
4.2.3 Test Results and Observations for Specimen 3	79
4.2.3.1 Crack Length versus Number of Cycles for Specimen 3.....	80
4.2.3.2 Change in Strain with Half Crack Length.....	82
4.2.4 Test Results and Observations for Specimen 4	84
4.2.4.1 Crack Length versus Number of Cycles for Specimen 4.....	85
4.2.4.2 Change in Strain with Half Crack Length.....	88
4.3 Comparison of Results	90
4.3.1 Half Crack length vs Number of Cycles.....	90
4.3.2 Strain in Steel vs. Half Crack length	92
Chapter 5 Conclusions, Field Implications and Future Work.....	93
5.1 Conclusions	93
5.2 Field Implications.....	94
5.3 Future Work	95

Bibliography	97
Appendix A Approximate Calculations for Concentration of Fluvial Sediments	103
Appendix B Detailed Drawings of Setup.....	108
Appendix C Calculations for Paris Law Constants for Specimen 1	114
LIST OF ABBREVIATIONS.....	116

LIST OF TABLES

Table 1. Constant Amplitude Fatigue Limits; after: AASHTO (2010)	12
Table 2. Different values for Paris law constants ‘C’ and ‘m’ for different types of steels; after: Barsom (1999)	16
Table 3. Mechanical properties of CFRP and adhesive provided by manufacturer	60
Table 4. Test Matrix.....	61
Table 5. Number of cycles for the points shown in Figure 48.....	79
Table 6. Number of cycles for the points shown in Figure 53.....	84
Table 7. Number of cycles for the points shown in Figure 58.....	90
Table 8. Sample calculations for ΔK for west half crack length of specimen 1	115

LIST OF FIGURES

Figure 1. Typical horizontally framed miter gate; source: HQUSACE (2010)	2
Figure 2. Components of miter gates; after: Riveros (1997)	3
Figure 3. Different modes of loading in fracture mechanics; after: Irwin (1958)	7
Figure 4. Infinite plate under tension with through thickness crack.....	8
Figure 5. Energy release rate for crack of length 'a' and 'da'; after: Anderson (1991).....	10
Figure 6. Coordinate system at the crack tip; after: François (2013).....	11
Figure 7. AASHTO fatigue detail categories; after: AASHTO (2010)	12
Figure 8. Typical da/dN versus ΔK curve.....	13
Figure 9. Crack tip yield zones; after: Wheeler (1972)	21
Figure 10. Air hammer peening for repairing fatigue cracks; after: Dexter (2005)	29
Figure 11. Hole drilling method to stop crack propagation; after: Dexter (2005).....	30
Figure 12. Vee and Weld repair method to repair through thickness cracks; after: Dexter (2005)	31
Figure 13. Addition of a doubler plate to repair through thickness crack; after Dexter (2005) ...	32
Figure 14. Chao Wu tests i) Specimen details ii) CFRP configuration; after: Wu (2012)	35
Figure 15. Specimen geometry for Yu tests (a) patch configuration A (b) patch configuration D (c) notch details; after: Yu (2014)	36
Figure 16. Hybrid bonded FRP technique (Wu, et al., 2011)	38
Figure 17. Possible failure modes of CFRP to steel bonded joints.....	39
Figure 18. A geometrical drawing showing a front view of the test setup including the actuator, self-reacting frame, the acrylic tank and the tested specimen	44

Figure 19. A physical front view of the test setup including the actuator, self-reacting frame, the base plate of the acrylic tank and the tested specimen.....	45
Figure 20. A physical front view of the test setup including the actuator, self-reacting frame, base plate with acrylic tank with water and tested specimen.....	46
Figure 21. A physical front view of the spreader beam including the specimen, the angle connecting the specimen and actuator	47
Figure 22. (a) 0.45-0.55 mm sand used (b) 23 kg (50 lbs) NaCl salt blocks	48
Figure 23. Propeller with electric motor in the tank facing back face of the specimen 4 at 45° ..	49
Figure 24. Locations of strain gauges (SG) on specimen 1	50
Figure 25. Locations of strain gauges (SG) on specimen 2 through specimen 3.....	51
Figure 26. Strain gauge locations on specimen 4 (Front face)	51
Figure 27. Strain gauge installation (a) Strain gauges from micro measurements (b) Strain gauge on the specimen and CFRP after installation (c) Soldering lead wires for strain gages (d) Protective covering for strain gauges.....	52
Figure 28. (a) Typical linear strain gauge used (b) Protective covering for strain gauges after installation on the specimen.....	53
Figure 29. Schematics of data flow and the DAQ system	53
Figure 30. Setup comprising of MTS 407 controller, two DAQ systems and a computer for data collection.....	54
Figure 31. Grid lines marked 2 cm apart on the specimen to measure the half crack length on either side of the crack	55
Figure 32. Tack weld introduced at crack tip to facilitate faster crack growth	55
Figure 33. Prepared surface before installation of CFRP	56

Figure 34. CFRP installation on specimen 2 (a) Markings on the specimen to install CFRP (b) preparation of adhesive (c) applying adhesive on the CFRP (d) CFRP on specimen after installation	58
Figure 35. CFRP bonded to specimen 110 mm from the center of the crack.....	60
Figure 36. Specimen nomenclature.....	61
Figure 37. Strain gauge (SG) locations on specimen 1.....	65
Figure 38. Stress vs. Strain data from strain gauges installed at various locations on specimen 1	67
Figure 39. Half crack length vs Number of cycles for Specimen 1	69
Figure 40. Crack surfaces for west half crack after fracturing the specimen 1 (a) Flat crack surface up to 150 mm from the center showing brittle fracture (b) Slightly slanted crack surface from 150 mm to 300 mm indicating ductile-brittle crack extension	70
Figure 41. Crack surfaces for west half crack after fracturing the specimen 1 (a) Shear lips form 300 mm to 500 mm indicating pure ductile fracture (b) Necking of the specimen indicating ductile crack extension.....	70
Figure 42. Crack surfaces for west half crack showing all the different fractures along the length of the crack after fracturing the specimen.....	71
Figure 43. A log-log plot of crack growth rate (da/dN) vs change in stress intensity factor (ΔK) for half crack lengths on east and west side of the specimen 1	72
Figure 44. Strain in steel vs Half crack length for Specimen 1 with respective strain gauge locations	73
Figure 45. Steel surface after CFRP debonding (front left) at 378,756 cycles for specimen 2	75
Figure 46. Half crack length vs Number of cycles for Specimen 2	76

Figure 47. Strain in steel vs. Half crack length for specimen 2 with strain gauge locations	77
Figure 48. Strain in CFRP vs. Half Crack length for Specimen 2 with strain gauge locations	79
Figure 49. Half crack length vs Number of cycles for Specimen 3.....	81
Figure 50. Crack propagation on each side of CFRP for Specimen 3	81
Figure 51. Fractured specimen 3.....	82
Figure 52. Strain in steel vs. Half crack length for Specimen 3 with strain gauge locations	83
Figure 53. Strain in CFRP vs. Half crack length for Specimen 3 with strain gauge locations	84
Figure 54. Specimen 4 showing (a) Steel surface after CFRP debonding (b) Debonding of CFRP at top edges	86
Figure 55. Crack length vs Number of cycles for Specimen 4	87
Figure 56. Back face of Specimen 4 after the test	87
Figure 57. Strain in steel vs. Half crack length for specimen 4 with strain gauge locations	88
Figure 58. Strain in CFRP vs. Half crack length for specimen 4 with strain gauge locations.....	89
Figure 59. Comparison of Half crack length vs. Number of Cycles for all specimens	91
Figure 60. Comparison of Strain in Steel vs. Half Crack Length for all specimens.....	92
Figure 61. Front view of the test setup frame	108
Figure 62. Beam to column shear connection and column base plate connection	109
Figure 63. HSS bracing for the frame.....	110
Figure 64. Actuator plate connections to bottom flange of top W24x94 beam.....	111
Figure 65. Spreader beam top view with holes to connect actuator swivel.....	111
Figure 66. Spreader beam bottom view with holes to connect angles connecting specimen	112
Figure 67. Bottom W24x94 beam and specimen connection	112
Figure 68. W24x94 and W33x169 beam connection.....	113

Figure 69. Bottom W24x94 beam and acrylic tank connections 113

Chapter 1

Introduction

1.1 Problem Statement

Steel structures operating in harsh corrosive environment such as miter gates, ships, oil rigs, pipes, among others, experience fluctuations in loading due to normal operation (e.g. loading and unloading of cargo ships) or their interaction with the surrounding water (e.g. wave loading). As a result, fatigue cracks can develop at various location in the structures and can become a nuisance as they require extensive inspection and continuous repair. Although the propagation of such cracks is typically stable, if left unrepaired, these cracks can propagate and threaten the integrity of the structures. It is important to note that this study aims to evaluate the fatigue repair of underwater structures through a newly devised experimental setup that seeks to provide data in relation to miter gates.

Miter gates are large steel structures, employed in navigational river locks, which through opening and closing allow passage of large vessels between different levels in a river system. Fabrication of miter gates is performed by welding steel sections using either horizontally framed or vertically framed configurations. A typical horizontally framed miter gate is very common (HQUSACE, 2010) and is shown in Figure 1. Horizontal girders are framed together with vertical diaphragms and skin plates welded to upstream flanges. These gates experience cyclic loading from opened to free hanging to closed condition (mitered condition) where arch action is utilized to transfer the hydrostatic loads to the lock walls through horizontal girders. During operation, the gates experience eccentric loading due to strut arm forces at the top of the gate and resistive forces of the submerged surfaces from the movement through the water. This eccentric loading causes twisting and warping to develop in various parts of the gates including the intersection of welded

vertical and horizontal flanges, cutouts, attachments to the skin plate, and pintle socket connections. With continuous operation, these components develop fatigue cracking.



Figure 1. Typical horizontally framed miter gate; source: *HQUSACE (2010)*

Fatigue life of structures is defined as the total life required for the crack to initiate and propagate to a critical length. Examples of miter gates in which fatigue cracking has been observed include the Snell Locks (built 1959) on the St. Lawrence Seaway, Greenup (built 1959), Meldahl (1959), Markland (built 1960) and McAlpine Locks (built 1961). Upper St. Anthony's Falls (built 1963), Poe locks at the Soo (built 1968), Bankhead Lock (built 1975). The main components of miter gates are shown in Figure 2. In all these examples, the most common fatigue cracking is observed at welded details and is due to the presence of tensile residual stresses coupled with geometric

concentration and weld geometry (HQUSACE, 2010). Fatigue cracks generally originate from a flaw in the weld and extend to the base metal connected to the weld. This cracking occurs mostly in the submerged surfaces and may require unscheduled outage for repairs (HQUSACE, 2010).

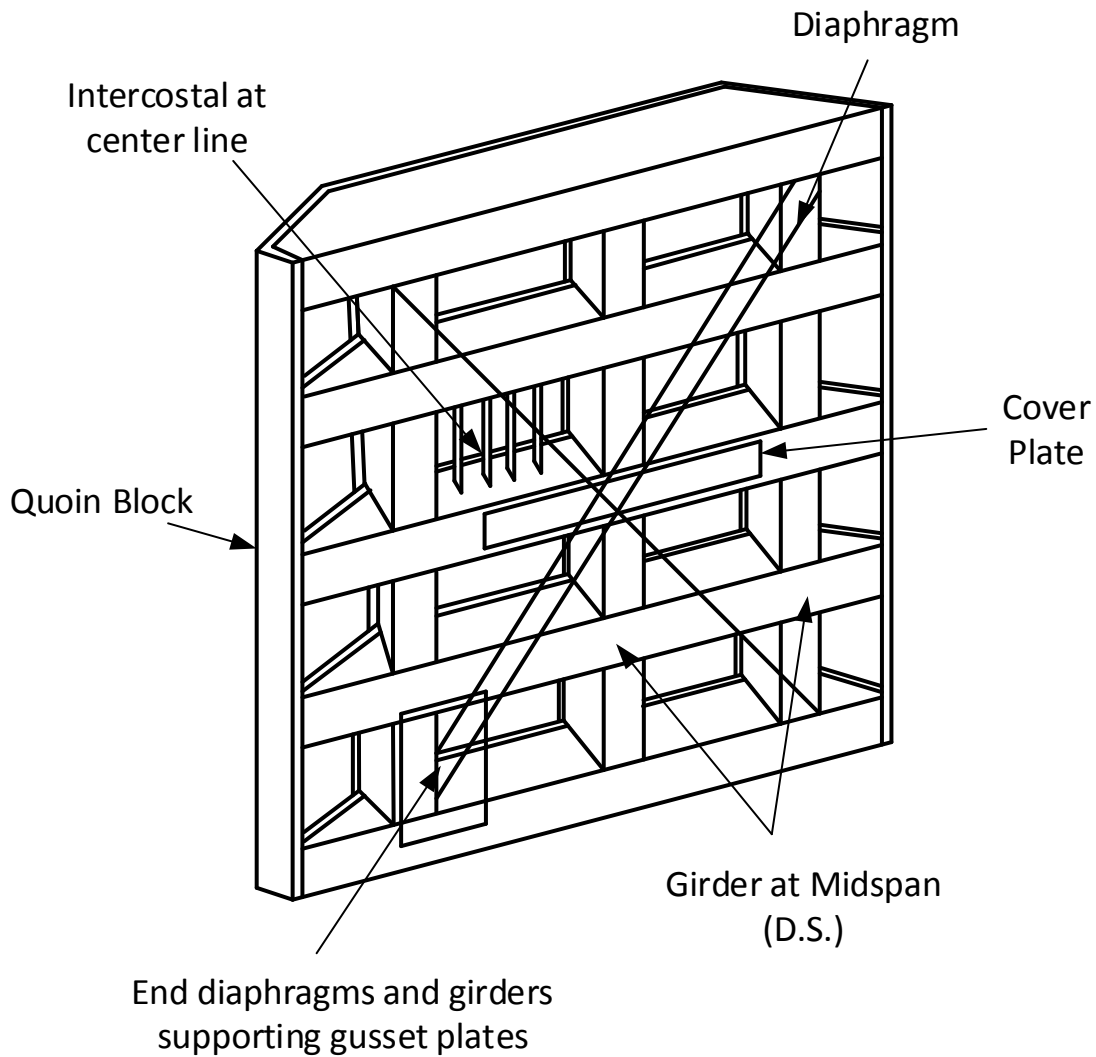


Figure 2. Components of miter gates; after: Riveros (1997)

1.2 Objective and Scope

As indicated previously, fatigue cracks in miter gates occur typically in the submerged portion of the gate and to repair these cracks whole catchment near the gates needs to be dewatered which

requires scheduled or unscheduled outage. This process is expensive, time consuming, and has a negative impact on the economy as it impacts the flow of goods through the river. It is therefore important to develop and evaluate new fatigue repair methods that are easy to implement and effective in mitigating crack growth so as to limit the disruption of the normal gate operation. To that end, carbon fiber reinforced polymer (CFRP) can be an attractive alternative for the repair of fatigue cracks. A recent study provided an in-depth overview of existing experimental and analytical studies on the use of CFRP for the repair of metallic structures and on the potential of using CFRP for the repair of hydraulic steel structures (Mahmoud, et al., 2013). The study indicated that several experimental research have been performed to evaluate the use of CFRP for extending the in-air fatigue life of aircraft stiffened aluminum panels and steel bridge girders but none have been conducted for repairing fatigue cracks in underwater metallic structures. A recent numerical study has been conducted by Como, Mahmoud and Riveros (2014) to evaluate crack growth in underwater CFRP-repaired steel panels. The study indicated that CFRP- repaired plates show significant improvement in fatigue life over non repaired plates with double-sided CFRP repairs exhibiting improvement over their single-sided counterparts.

The previously conducted studies show reduction in crack propagation rate when CFRP strips are either covering the crack fully or when placed ahead of the crack tips (Wu, et al., 2012, Alemdar, et al., 2011, Tavakkolizadeh, et al., 2003). When CFRP is attached at the crack front where the local stresses are higher than the nominal stresses, it reduces the effect of higher local stresses by providing additional stiffness, locally, which limits the crack mouth opening. Although this might not stop the propagating crack fully, it slows down the rate of propagation. This research deals with the application of CFRP and its effects on crack propagation rate in underwater steel panels.

The objectives of this study are as follows:

- To develop a new experimental setup that allows for underwater assessment of crack growth in CFRP-repaired steel panels.
- To determine if the bonded CFRP have any effect on the rate of fatigue crack propagation in underwater steel plates.
- To determine the effect of using different underwater adhesive on CFRP debonding.
- To determine the effect of using different types of CFRP on fatigue crack propagation rate.
- To determine the effect of corrosion, introduced using salt, on the behavior of bonded CFRP.
- To determine the effect of fluvial sediments on the behavior of the bonded CFRP.

1.3 Organization of Thesis

This thesis is comprised of five chapters. Chapter 1 introduces the problem statement and research objectives. Chapter 2 discusses the background and literature review in relation to the use of CFRP for mitigating fatigue crack propagation. Chapter 3 discusses the experimental setup developed and the specimen topology utilized in this research. Chapter 4 focuses on the experimental results regarding application of the CFRP near crack tip as well as the effect of salt and fluvial sediments on the CFRP and fatigue crack growth. Chapter 5 discusses the conclusion, field implications and outlines future research requirements.

Chapter 2

Background and Literature Review

2.1 Fracture Mechanics

The theory of fracture mechanics has been well-established and used for predicting fatigue and fracture strength of various materials. This theory comprises of two main fundamental approaches; namely Linear Elastic Fracture Mechanics (LEFM) and Elasto Plastic Fracture Mechanics (EPFM). Both of these approaches deal with the analysis of the stress field at the crack tip with either limited plasticity (LEFM) or large plasticity (EPFM). Fatigue analysis under service loads is known to be governed by the live-load stress range and in such case the maximum applied load is typically much less than the load that would cause yield in the material. Consequently, LEFM is adequate for analysis concerning fatigue crack growth where the propagation is governed by cyclic stresses that are relatively of small magnitude.

In Fracture mechanics, the modes of loading under which crack extension would occur fall into three different types, i.e. mode I, II and III as illustrated in Figure 3 (Irwin, 1958). In mode I, also called the opening mode, the crack faces are moving away from each other when the applied load is perpendicular to the plane of the crack. Mode II is in-plane shearing mode and mode III is anti-planar shearing mode or simply tearing mode. Most civil engineering structures are geometrically symmetric and the primary stresses are typically perpendicular to the details in question. Therefore, the details are primarily under mode I loading. It is important to recognize that hydraulic steel structures are subjected to complex loading conditions through which multiple modes might drive the initiation and propagation of cracks. In this study, however, the focus is on mode I loading only and is intended to provide a base for further studies which may include mixed mode loading conditions.

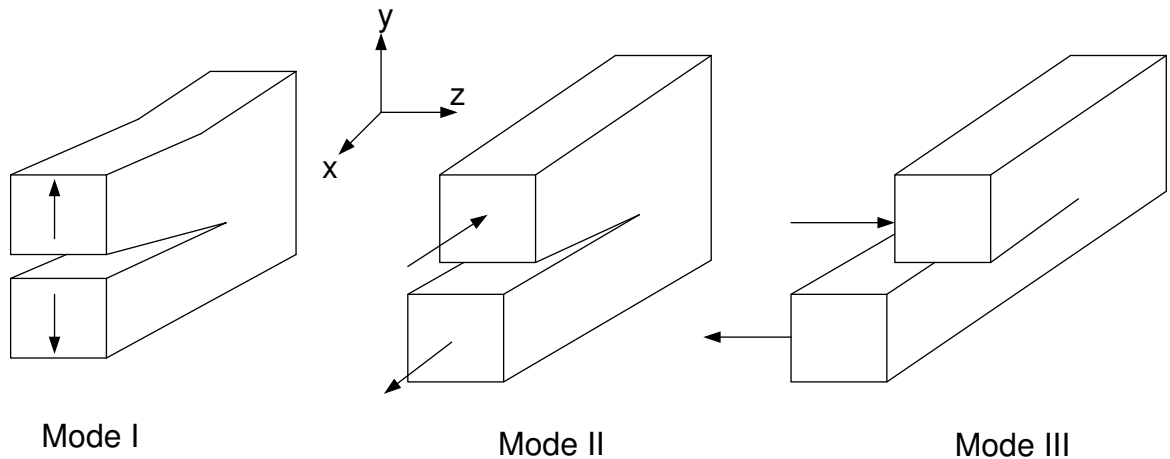


Figure 3. Different modes of loading in fracture mechanics; after: Irwin (1958)

Under mode I, or opening mode, the body is loaded by tensile forces, such that the crack surfaces are pulled apart in the y direction (shown in Figure 3). The deformations are then symmetric with respect to the planes perpendicular to the y axis and the z axis. Under mode II, or sliding mode, the body is loaded by shear forces parallel to the crack surfaces, which slide over each other in the x direction (Figure 3). The deformations are then symmetric with respect to the plane perpendicular to the z axis and skew symmetric with respect to the plane perpendicular to the y axis. Finally, under mode III, or tearing mode, the body is loaded by shear forces parallel to the crack front the crack surfaces, and the crack surfaces slide over each other in the z direction. The deformations are then skew-symmetric with respect to the plane perpendicular to the z and the y axis (Figure 3).

2.2 Linear Elastic Fracture Mechanics

The stress intensity factor (K), which defines the demand associated with the state of stress at the crack tip, is the main parameter in linear elastic fracture mechanics (LEFM). It is a measure of magnitude of the stress and strain fields at the crack tip, which can be described by

$$K = F_c F_s F_w F_g \sigma \sqrt{\pi a} \quad (1)$$

Where,

K = Stress intensity factor

F_c = Crack shape factor

F_s = Crack surface factor

F_w = Finite width factor

F_g = Non-uniform stress factor

σ = Nominal stress

a = Half the crack length

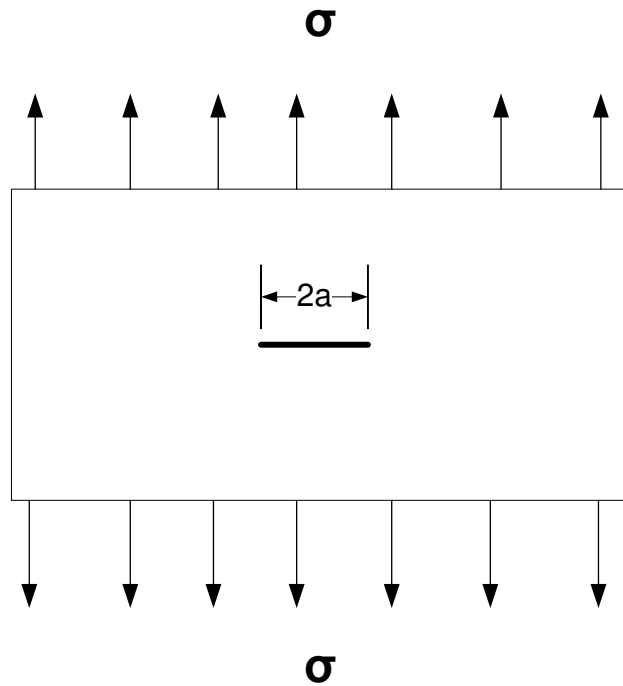


Figure 4. Infinite plate under tension with through thickness crack

Crack length 'a' is taken as half the crack length for a center crack and as the total crack length for an edge crack. The stress intensity factor has units of MPa-m^{1/2} or ksi-in^{1/2}. The resistance of material against brittle fracture depends on the relation $K < K_c$ (Anderson, 1991), where K_c is the critical stress intensity factor which is also known as the fracture toughness of a material which simply can be viewed as the capacity of the particular material. Primary parameters affecting fracture toughness are temperature, loading rate, and material thickness.

2.3 Strain Energy Release Rate

The energy release rate 'G' for a crack growing under mode I is a function of material thickness 't' and the change in energy stored 'dU' for crack extension 'da'. When the energy available for crack growth is higher than the resistance provided by the material, crack will grow. Figure 5 (a) explains the energy stored in the material when loaded with force P. As crack extends by 'da', the stored energy (U) in the material is released and used to form a new crack of length (a+da) as shown in Figure 5 (b). The stored energy is decreased by 'dU'. Hence, the total energy remaining in the body is 'U-dU'. Stress intensity factor 'K' and energy release rate 'G', for plane stress condition, can be related by a formula:

$$G = \frac{K^2}{E} \quad (2)$$

Where, E = Modulus of elasticity for given material

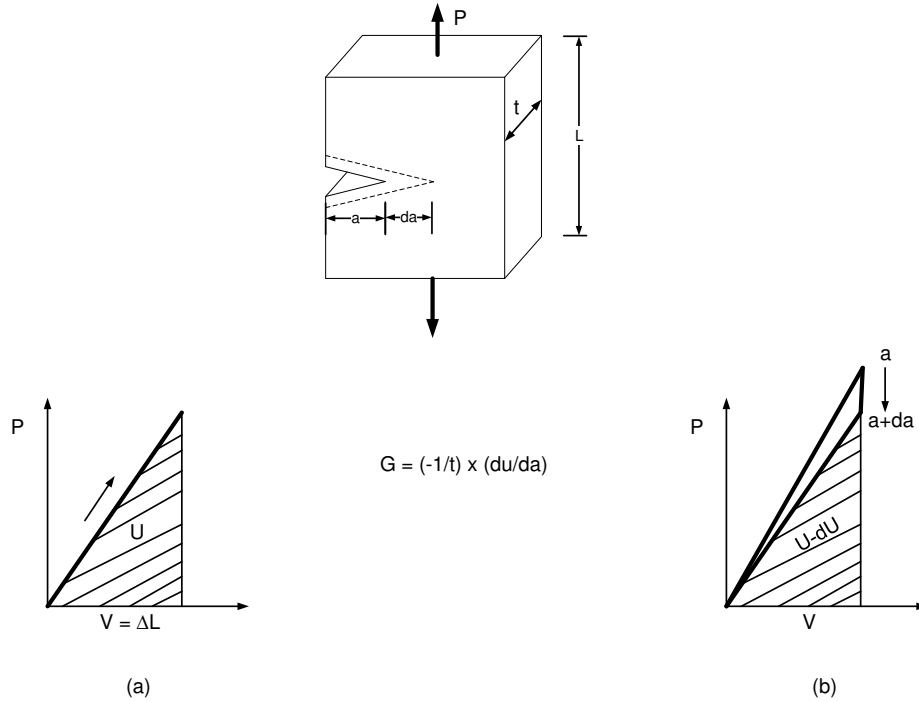


Figure 5. Energy release rate for crack of length 'a' and 'da'; after: Anderson (1991)

2.4 Stress Intensity Factor

As previously indicated the stress intensity factor 'K' describes the state of stress in the vicinity of the crack tip. Equation 3 gives the formula for the stresses surrounding the crack tip with the coordinate system shown in Figure 6.

$$\begin{Bmatrix} \sigma_{11} \\ \sigma_{22} \\ \sigma_{12} \end{Bmatrix} = \frac{K_I}{\sqrt{2\pi r}} \cos(\theta/2) \begin{Bmatrix} 1 - \sin\left(\frac{\theta}{2}\right) \sin\left(\frac{3\theta}{2}\right) \\ 1 + \sin\left(\frac{\theta}{2}\right) \sin\left(\frac{3\theta}{2}\right) \\ \sin\left(\frac{\theta}{2}\right) \cos\left(\frac{3\theta}{2}\right) \end{Bmatrix} \quad (3)$$

In plane strain, $\sigma_{33} = \nu (\sigma_{11} + \sigma_{22})$ and in plane stress $\sigma_{33} = 0$.

Applying this equation at the crack tip shows that the stresses, mathematically, approach infinity.

The singularity at the crack tip need to be carefully considered when evaluating K. Therefore, it is

customary to evaluate K near the crack tip. In such case, the stress intensity factor for mode I can be calculated as the limit definition as shown below

$$K_I = \lim_{r, \theta \rightarrow 0} \sigma_{22} \sqrt{2\pi r} \quad (4)$$

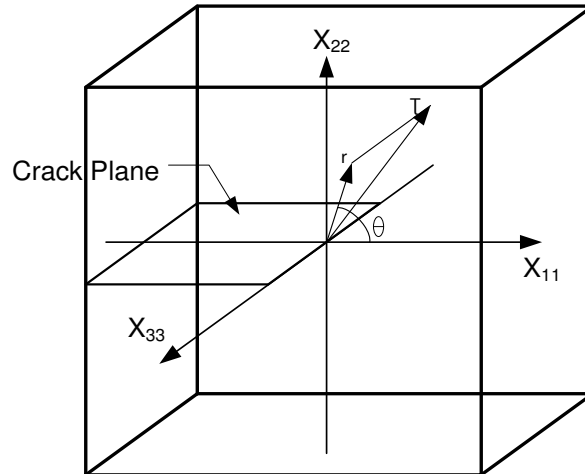


Figure 6. Coordinate system at the crack tip; after: *François (2013)*

2.5 Fatigue Category Details

As previously noted, fatigue life comprises of an initiation phase and a propagation phase. AASHTO LRFD provisions provide different fatigue detail categories and their corresponding S-N curves to determine the initiation life (AASHTO, 2010). The S-N curves are log-log plot of the stress range versus number of cycles (Figure 7). For a particular fatigue detail, if the stress range is below its constant amplitude fatigue limit, cracking is postulated not to occur. The dotted lines in Figure 7 show the constant amplitude range for the different details. Constant amplitude fatigue limits for the corresponding fatigue categories are given in Table 1.

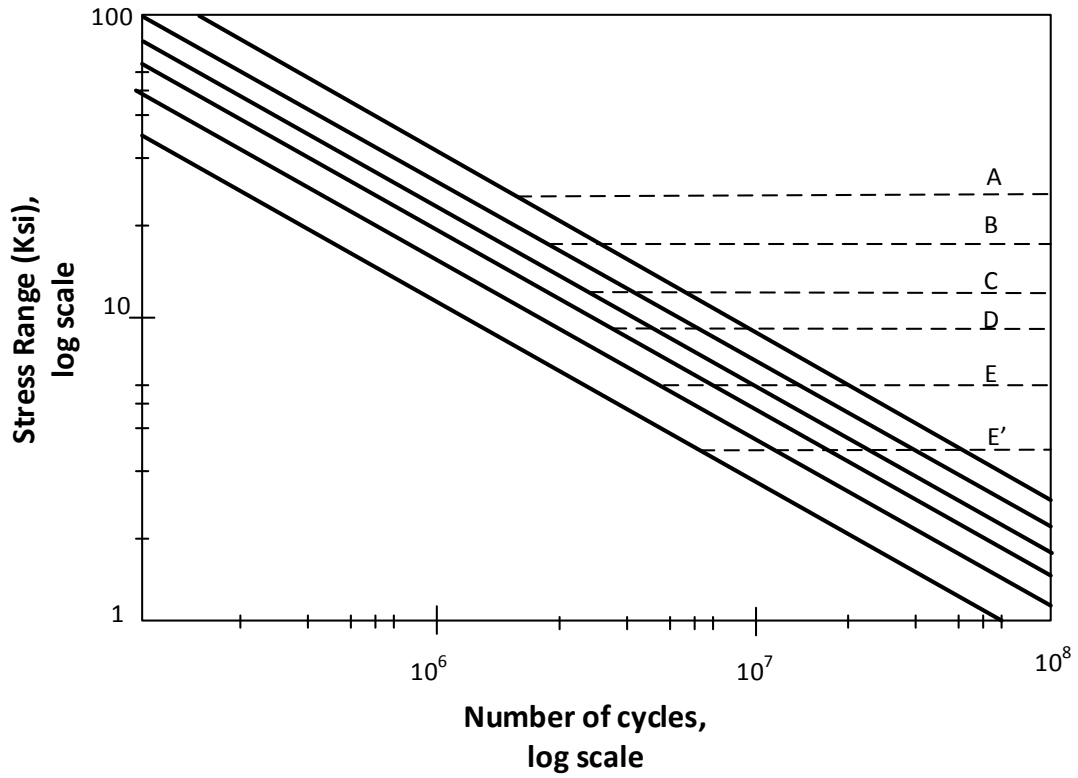


Figure 7. AASHTO fatigue detail categories; after: AASHTO (2010)

Table 1. Constant Amplitude Fatigue Limits; after: AASHTO (2010)

Detail Category	Constant Amplitude Fatigue Limit (CAFL) (Ksi)
A	24
B	16
B' or C'	12
C	10
D	7
E	4.5
E'	2.6

2.6 Fatigue Rate Curve

For fatigue crack propagation, a crack growth rate curve is commonly known as da/dN versus ΔK curve, which is typically divided into three distinct regions (region I, II and III) as shown in Figure 8.

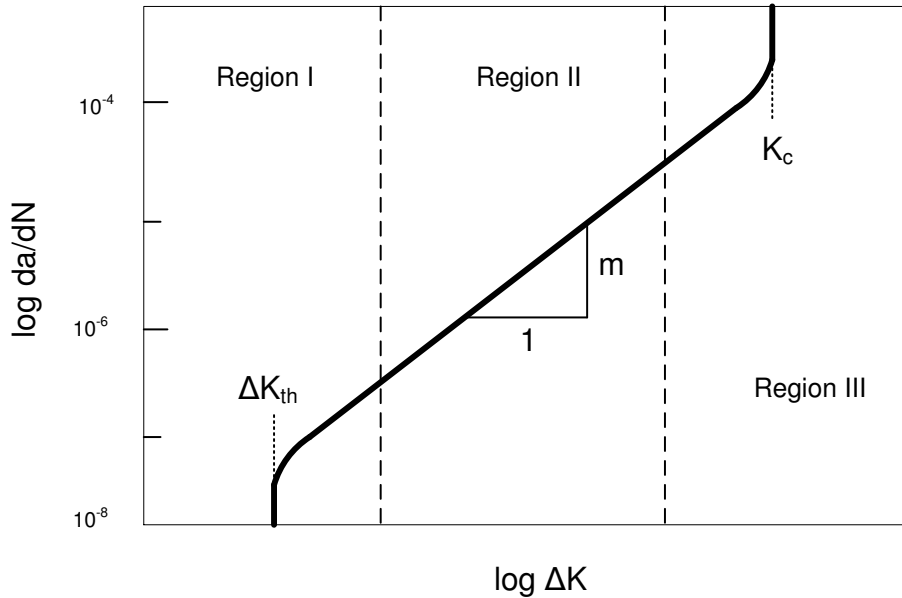


Figure 8. Typical da/dN versus ΔK curve

Region I represents the nucleation of the fatigue crack. This region is influenced by microscopic features such as grain size, type of bond, applied stress, temperature and environmental conditions. There exists a stress intensity factor range below which fatigue cracks should not propagate. This is known as fatigue crack growth threshold and is represented as ΔK_{th} .

Region II represents crack propagation zone in which linear elastic fracture mechanics concepts are applicable. In this region crack tip is long compared to mean grain size but much smaller than the actual crack length. Stable crack growth can be seen in this region and the effects of microstructure, mean stress, and ductility are small.

Region III represents the unstable crack growth just before the fracture. Stress intensity factor approaches fracture toughness K_c of the material. The plastic zone near the crack tip is considerably large and concepts of LEFM are not applicable in this region. EPFM concepts should be applied for accurately predicting the unstable crack growth and fracture of the material.

2.7 Fatigue Crack Growth Rate Models

Many aspects of fatigue crack growth were well understood in mid-20th century. A damage model for the computation of crack growth under variety of service loads was required (Beden, et al., 2009). Many researchers have conducted thorough studies on both 1) constant amplitude fatigue loading and 2) variable amplitude fatigue loading. Beden (2009) reviewed these models and some of them are presented in following sub-articles.

The generalized equation that relates the change in crack length (da) and number of cycles (dN) to ΔK and R can be described using the following equation

$$\frac{da}{dN} = f(\Delta K, R) \quad (5)$$

Where,

R = Minimum load to maximum load ratio

ΔK = Range of stress intensity factor

2.7.1 Constant Amplitude Fatigue Loading Models

Constant amplitude fatigue loading is the most general type of the fatigue growth analysis in which no load history has to be considered. There are many fatigue crack growth models that vary in the factors considered and different curve fitting parameters.

2.7.1.1 Paris Model

In 1963, Paris and Erdogan (Paris, et al., 1963) showed that the range in stress intensity factor (ΔK) are related to the fatigue crack growth. It has been showed that the plot of crack growth rate versus ΔK is represented by a straight line when plotted on a log-log scale. There is a threshold ΔK value, denoted as ΔK_{th} , below which a crack will not propagate. Value for ΔK_{th} can be taken as 3 MPa-m^{1/2} for structural steel. At high ΔK values the crack growth is unstable and is accompanied by ductile fracture. The Paris Law can be given as

$$\frac{da}{dN} = C \Delta K^m \quad (6)$$

Where,

a = Half crack length

N = Number of cycles

ΔK = Range of stress intensity factors

C and m = Material constants

It is worth noting that the load ratio, R, is often indirectly taken into account in the Paris law by using the effective stress range, ΔK_{eff} , which accounts for all parameters affecting crack growth rate including applied loads and residual stresses. Most researchers agree that all structural steels have similar crack growth rates and the variance observed in C values is just material variation (Dexter, et al., 2004). The most reported values of C represent a conservative upper bound fit to the data. Typical values of 'C' and 'm' obtained for different types of steels are tabulated in Table 2. (Barsom, et al., 1999)

Table 2. Different values for Paris law constants ‘C’ and ‘m’ for different types of steels; after: Barsom (1999)

Type of Steel	C [in/(cycle*ksi*in ^{0.5})]	m [no unit]
Martensitic Steel	0.66×10^{-8}	2.25
Ferrite-Pearlite Steel	3.6×10^{-10}	3
Austenitic Stainless Steel	3.0×10^{-10}	3

2.7.1.2 Walker Model

The Paris law does not take in to account the stress ratio (R). This limitation was improved by Walker (1970) who included the effect of the stress ratio and the maximum stress intensity factor through the introduction of a new parameter ΔK . The equation proposed by Walker is as follows

$$\overline{\Delta K} = K_{\max} (1 - R)^{\gamma_w} \quad (7)$$

Where, $K_{\max} = \Delta K / (1 - R)$

Therefore,

$$\overline{\Delta K} = \frac{\Delta K}{(1 - R)^{1 - \gamma_w}} \quad (8)$$

Hence, the Walker law can be written as

$$\frac{da}{dN} = C_w (\overline{\Delta K})^{m_w} \quad (9)$$

or,

$$\frac{da}{dN} = C_w \left(\frac{\Delta K}{(1 - R)^{1 - \gamma_w}} \right)^{m_w} \quad (10)$$

For R=0, the above equation becomes

$$\frac{da}{dN} = C_w(\Delta K)^{m_w} \quad (11)$$

Where,

C_w and m_w are material constants defined by Walker (1970)

This is similar to Paris law. This model includes the effect of stress ratio but also introduces a new parameter γ_w . This new parameter is determined by trial and error method and it is possible that no value of γ_w can be found. In this scenario Walker model cannot be used to predict fatigue crack growth rate.

2.7.1.3 Forman Model

Forman (1972) improved the Walker model by suggesting new model which includes the unstable region, Region III, of the fatigue rate curve. Forman law can be given by following equation

$$\frac{da}{dN} = \frac{C_F(\Delta K)^{m_y}}{(1-R)K_C - \Delta K} = \frac{C_F(\Delta K)^{m_y}}{(1-R)(K_C - K_{max})} \quad (12)$$

Here, K_c is fracture toughness of the material and C_F and m_y are material constants defined by Forman (1972). This equation indicates that as K_{max} approaches K_c , da/dN tends to infinity. Hence, the model is capable of representing region II (stable growth) as well as region III (accelerated growth) of the fatigue rate curve. For each data point, Forman equation is capable of representing the data for different stress ratios using the following quantity

$$Q = \frac{da}{dN} [(1-R)K_C - \Delta K] \quad (13)$$

If different ΔK and R combinations fall together on a straight line then the Forman model may be used. Comparing above equations, the Forman law can be written as

$$Q = C_F(\Delta K)^{m_y} \quad (14)$$

In continuation to Forman model, Hartman and Schijve proposed new equation as follows

$$\frac{da}{dN} = \frac{C_{HS} (\Delta K - \Delta K_{th})^{m_{HS}}}{(1 - R)K_c - \Delta K} \quad (15)$$

Where,

C_{HS} and m_{HS} are material constants defined by Hartman and Schijve.

This gives another version of the Forman law

$$\frac{da}{dN} = \frac{C_{MOD}(\Delta K)^{m_{MOD}} (\Delta K - \Delta K_{th})^{0.5}}{(1 - R)K_c - \Delta K} \quad (16)$$

Where C_{MOD} and m_{MOD} are material constants for modified Forman law.. The disadvantage of using these equations is the ΔK_{th} is sensitive to the value of R and specific value of ΔK_{th} needs to be substituted for particular value of R .

2.7.1.4 Collipriest Model

Collipriest (1972) proposed a crack growth model capable of describing all three regions of the fatigue rate curve while incorporating the stress ratio effect. It is given by the following expression

$$\frac{da}{dN} = C(K_c/\Delta K_{th})^{\frac{m}{2}} EXP \left[\ln \left(\frac{K_c}{\Delta K_{th}} \right)^{\frac{m}{2}} \tanh^{-1} \left[\frac{\ln \left(\frac{\Delta K^2}{(1 - R)K_c \Delta K_{th}} \right)}{\ln \left(\frac{(1 - R)K_c}{\Delta K_{th}} \right)} \right] \right] \quad (17)$$

Although this model includes all the three regions of the fatigue rate curve, it appears to be complicated as it involves various parameters.

2.7.1.5 Frost and Pook Model

Frost and Pook (1971) hypothesized that crack growth occurs under cyclic loading is not a result of progressive structural damage but is due to the formation of striations that are caused by reshaping the crack tip at each cycle because of unloading. This model is based on the increment of crack growth with each cycle which can be related to changing crack tip geometry during opening and closing of the crack. This relationship can be given by

$$\frac{da}{dN} = \frac{9}{\pi} \left(\frac{\Delta K}{E}\right)^2 \quad \text{for plane stress} \quad (18)$$

$$\frac{da}{dN} = \frac{7}{\pi} \left(\frac{\Delta K}{E}\right)^2 \quad \text{for plane strain} \quad (19)$$

Frost and Pook found that the prediction of plane stress equation and experimental data plotted in terms of $\Delta K/E$ against da/dN are in good agreement at crack growth rates around 3×10^{-5} mm/cycle. (Beden, et al., 2009) Experimental crack growth rates are underestimated at high growth rates and overestimated at low growth rates.

2.7.1.6 Pugno Model

Pugno and Ruoff (2004) generalized the Paris law using Quantized Fracture Mechanics by

substituting $K(a)$ with a mean value, $K^*(a, \Delta a) = \sqrt{[K^2(a)]_a^{a+\Delta a}}$, where Δa is “fracture quantum”,

which is a material constant for infinite life. They proposed a generalized law as follows

$$\frac{da}{dN} = C [\Delta K^*(a, \Delta a, \Delta \sigma)]^m \quad (20)$$

Where, Δa is function of $\Delta \sigma$. Integrating equation 20, the total number of cycles for fatigue collapse (when the crack length has reached its critical final value at a_c) can be given as

$$N_C^{P^*} = \frac{1}{\bar{C}} \int_a^{a_c} \frac{da}{[\Delta K^*(a, \Delta a, \Delta \sigma)]^m} \quad (21)$$

In equation 21, Δa can be recovered using Wohler's prediction in the limit case of $a \rightarrow 0$ and it can be written that

$$N_C^W = \frac{\bar{C}}{\Delta \sigma^k} \quad (22)$$

Hence,

$$\Delta a: N_C^{P^*}(a \rightarrow 0) = N_C^W \quad (23)$$

This simple law would allow one to study not only the final fracture but also the fatigue crack growth $N_C^{P^*}[a(N)]$ where, $a \leq a(N) \leq a_c$.

2.7.1.7 Wheeler Model

Wheeler (1972) proposed a model that takes in to account retardation by introducing a new parameter called retardation parameter. This model can be applied to any fatigue crack growth equation $da/dN = f(\Delta K, R)$. Wheeler's law can be given as

$$\frac{da}{dN} = \phi_R f(\Delta K, R) \quad (24)$$

Where,

$$\phi_R = \left(\frac{R_y}{a_p - a}\right)^y \quad \text{for } (a + R_y) < a_p$$

or,
$$\phi_R = 1 \quad \text{for } (a + R_y) \geq a_p$$

and,

ϕ_R = retardation parameter

R_y = extent of current yield zone

y = shape factor

$a_p - a$ = distance from crack tip to elastic plastic interface

These parameters are illustrated in Figure 9. For plane strain conditions, Wheeler suggested that

$$R_y = \frac{1}{4\pi\sqrt{2}} \left(\frac{K_I}{\sigma_y} \right)^2 \quad (25)$$

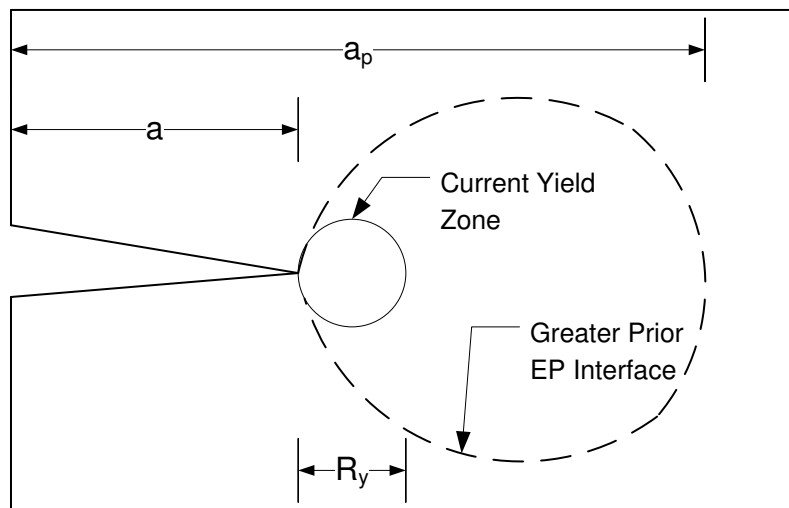


Figure 9. Crack tip yield zones; after: *Wheeler (1972)*

2.7.1.8 Willemborg Model

Willemborg (1971) modified Wheeler's Model by determining the amount of retardation as a function of stress intensity factor to cancel the effect of overload plastic zone. The modified stress intensity factor can be written as

$$K_r = (K_{max})_{OL} \left(1 - \frac{\Delta a}{Z_{OL}}\right)^{\frac{1}{2}} - K_{max} \quad (26)$$

Where, $(K_{max})_{OL}$ is maximum stress intensity factor during overload, Δa is the amount of crack growth since the overload, Z_{OL} is the overload plastic zone size and K_{max} is the maximum stress intensity factor for normal loading.

Johnson (1981) gave an equation for overload plastic zone as follows

$$Z_{OL} = \frac{1}{\beta\pi} \left[\frac{(K_{max})_{OL}}{\sigma_y} \right]^2 \quad (27)$$

2.7.1.9 Barsom Model

Barsom (1976) described the stress intensity factor in terms of root mean square value of stress intensity factor range, ΔK_{rms} . It can be given as

$$\Delta K_{rms} = \sqrt{\sum_{i=1}^n \Delta K_i^2} \quad (28)$$

Where, ΔK_i is the stress intensity factor for i^{th} cycle of loading consisting of n cycles. This model does not account for crack growth rate retardation.

Barsom obtained a single stress intensity parameter that will describe crack growth rate under both constant amplitude loading and variable amplitude loading. If the requirements of the above equation are satisfied, Barsom proposed the following relationship

$$\frac{da}{dN} = A_B (\Delta K_{rms})^{m_B} \quad (29)$$

where, A_B and m_B are constants and

$$\Delta K_{rms} = \sqrt{\frac{\sum_{r=1}^k \Delta K_r^2}{n}} \quad (30)$$

ΔK_{rms} is the parameter that represents the root mean square of the individual load cycle in the spectrum. This model is simple to use as it requires to determine the curve fitting parameters A_B and m_B .

2.7.2 Variable Amplitude Fatigue Loading Models

Crack growth in structures depends on the amplitude, stress ratio, and frequency of the load (Beden, et al., 2009). It is difficult to model the randomness in these parameters since the variable loading is random in nature. Overload cycles retard the crack growth rate while underload cycles accelerate the growth. Different approaches were used to develop these models for variable amplitude fatigue loading namely 1) Yield Zone Size 2) Crack Closure Approach 3) Strain Energy Density Factor. Due to complex mechanisms existing in these models, no universal model has been derived.

2.7.2.1 Chang, Szamossi and Liu Model

Two different approaches were considered for experiments conducted on center-cracked tension specimens under random spectrum loading by Chang, Szamossi and Liu (1981). One approach did not account for load interactions such as tensile overload retardation, compressive load acceleration, etc. The model can be given as

$$\frac{da}{dN} = C \left[\frac{\Delta K}{(1 - \bar{R})^{1-\gamma}} \right]^m \quad (31)$$

Here, γ is a constant to be determined through experiments.

And if $\Delta K > \Delta K_{th}$

$$0 \leq \bar{R} \leq R_{cut}^+, \quad \bar{R} = R$$

$$0 \leq \bar{R} \geq R_{cut}^+, \quad \bar{R} = R_{cut}^+$$

Where, R = stress ratio

R_{cut}^+ = cut off value of stress ratio

For $\Delta K \leq \Delta K_{th}$ $\frac{da}{dN} = 0$

Where, $\Delta K_{th} = (1-R) \Delta K_{tho}$

ΔK_{tho} = threshold value of ΔK for R=0

2.7.2.2 Hudson Model

Hudson (1981) used the similar approach as Barsom (1976) to predict the fatigue crack growth under random spectrum loading that is typically experienced by aircraft. This approach neglects the load interactions effect and provides an average fatigue crack growth rate when load interactions is limited. The maximum and minimum mean square stress levels can be calculated using following equations

$$\sigma_{max rms} = \left[\frac{1}{N} \sum_{r=1}^N (\sigma_{max})^2 \right]^{\frac{1}{2}} \quad (32)$$

And

$$\sigma_{min rms} = \left[\frac{1}{N} \sum_{r=1}^N (\sigma_{min})^2 \right]^{\frac{1}{2}} \quad (33)$$

Where, σ_{max} and σ_{min} are the maximum and minimum stresses of random loading and N is the total number of these stresses. Root mean square stress ratio can be given as

$$R_{rms} = \frac{\sigma_{min rms}}{\sigma_{max rms}} \quad (34)$$

The root mean square maximum and minimum stress intensity factors can be give using correction factor for center cracked specimen.

$$K_{\max rms} = \sigma_{\max rms} \sqrt{\pi a \sec\left(\frac{\pi a}{W}\right)} \quad (35)$$

And

$$K_{\min rms} = \sigma_{\min rms} \sqrt{\pi a \sec\left(\frac{\pi a}{W}\right)} \quad (36)$$

Where, ‘a’ is half crack length and ‘W’ is specimen width. The root mean square stress intensity range can be given as

$$\Delta K_{rms} = K_{\max rms} - K_{\min rms} \quad (37)$$

Hudson used above parameters along with Forman equation to predict fatigue crack growth rates

$$\frac{da}{dN} = \frac{C \Delta K_{rms}^m}{(1 - R_{rms})K_c - \Delta K_{rms}} \quad (38)$$

Where, K_c is elastic fracture toughness.

2.7.2.3 Newman Model

Newman (1981) used crack closure approach for predicting the fatigue life. He calculated the crack opening stress as a function of crack length and loading history from an analytical model. The law proposed by Newman can be written as

$$\frac{da}{dN} = C_1 \left[\frac{\Delta K_{eff}}{1 - \left(\frac{K_{max}}{C_3}\right)^2} \right]^{C_2} \quad (39)$$

Where, $\Delta K_{eff} = (\sigma_{max} - \sigma_{op})Y\sqrt{\pi a}$. C_1 , C_2 and C_3 are constants determined using constant amplitude loading data by least squares.

He re-predicted the results using equation 35 and giving new equation as follows

$$\frac{da}{dN} = C_1 \Delta K_{eff}^{C_2} \left[\frac{1 - \left(\frac{\Delta K_o}{\Delta K_{eff}} \right)^2}{1 - \left(\frac{K_{max}}{C_5} \right)^2} \right] \quad (40)$$

Where; $\Delta K_o = C_3 \left(1 - C_4 \frac{\sigma_o}{\sigma_{max}} \right)$; and $K_{max} = \sigma_{max} Y \sqrt{\pi a}$

In 1997, Newman developed a much more realistic finite element model. It includes plastic zone which causes interference between crack surfaces. Until now, this finite element model is the best to predict fatigue crack growth (Beden, et al., 2009).

2.7.2.4 Johnson Model

Johnson (1981) used multi-parameter yield zone (MPYZ) for determining fatigue crack growth under random variable loading. It accounts for crack growth retardation and acceleration by modifying the stress ratio in Forman equation. Model proposed by Johnson can be written as

$$\frac{da}{dN} = \frac{C \Delta K^n}{(1 - R^{eff})^m K_C - \Delta K} \quad (41)$$

Where, $m=1$ at $R>0$ and $m=2$ at $R<0$.

R^{eff} accounts for all the load interactions when full stress intensity range is used adjusting its value for each cycle. ‘C’ and ‘n’ are obtained from the constant amplitude loading data. The threshold ΔK_{th}^* can be expressed as

$$\Delta K_{th}^* = (1 - R^{eff}) \Delta K_{th} \quad (42)$$

Here, ΔK_{th} is obtained for $R=0$. The effective stress ratio then will be

$$R^{eff} = \frac{K_{min} - K_R}{K_{max} - K_R} = \frac{K_{min}^{eff}}{K_{max}^{eff}} \quad (43)$$

K_R is residual stress intensity generated due to plasticity around the crack tip. The maximum allowable stress ratio will be

$$R_{max} = \left[\frac{0.2Z_{OL}}{t} \right] + 0.6 \quad (44)$$

Where, Z_{OL} is the plastic zone size.

2.7.2.5 Modified Miner Model

Varma (1990) introduced a model based on Miner rule which does not account for rain flow counting technique to predict the fatigue crack growth rate under random loading. The equation can be given as

$$\Delta K_{eff} = \sum \left[\frac{n_i \Delta K_i^m}{N_T} \right]^{\frac{1}{m}} = \sum \left[\frac{n_i}{N_T} \right]^{\frac{1}{m}} \Delta K_i \quad (45)$$

Where,

ΔK_{eff} = effective stress intensity factor range

N_i = number of cycles

ΔK_i = stress intensity factor range for i^{th} cycle

N_T = total number of cycles

m = constant

2.8 Fatigue Crack Repair and Retrofit Methods

Many fatigue crack repair and retrofit methods are available. Repairing existing cracked material can be performed either by removing the crack through gouging and filling the gouged area with weld metal or by modifying the stresses at the crack tip without removing the cracks. In some cases, whether the crack is removed or not, reinforcing plates can be added to reinforced the troubled area. In general, repair and retrofit methods can be classified as 1) Surface Treatments, 2) Repair of Through-Thickness Cracks and 3) Modifying the specific detail or entire global structure in order to reduce further cracking (Dexter, et al., 2005).

2.8.1 Surface Treatments

Surface treatments include grinding, gas tungsten arc (GTA) re-melting, impact treatments (only for shallow cracks) and hole drilling. Grinding includes disc grinding and burr grinding. It is used to partially or fully remove the cracked details. Finish grinding should be performed such that the sparks generated due to grinding fly parallel to the direction of the primary stress. Small micro cracks could be generated during welding procedure which might grow and become fatigue cracks under cyclic loads which can be removed by grinding. Disc grinding does not increase the fatigue life in appreciable amount but burr grinding provides 50% higher allowable stress range over untreated details (Dexter, et al., 2005).

Gas tungsten arc (GTA) remelting is similar to welding weld toe and base metal. Metal is only melted without adding any extra material while gas shielded tungsten electrode is manually moved along the weld toe. This method reduces the stress concentration at weld toe. The effectiveness of this method requires higher operator skills as well as adequate penetration which is difficult to attain for field operations.

Impact treatments include air hammer peening and ultrasonic impact treatment. These methods introduce local compressive residual stresses near the crack tips and are only applicable for shallow cracks (typically less than 3mm). Air hammer peening includes air hammer with blunt tip to deform the weld toe creating local compressive stresses. This helps in reducing the tensile stress range and increasing the fatigue life. Ultrasonic impact treatment (UIT) is another impact treatment which is quieter than air hammer. UIT has proven to be the most effective than hammer peening and it might increase the fatigue strength of the detail by one category (Dexter, et al., 2005).



Figure 10. Air hammer peening for repairing fatigue cracks; after: Dexter (2005)

In hole drilling, a hole is drilled at the crack tip to reduce the stress concentration at the tip of the crack and extend fatigue life. Larger holes are better as long as the strength of the detail is not altered. To improve the effectiveness of these holes, cold expansion method is used whereby a pin, slightly larger in diameter than the hole, is punched through the hole and as the pin passes through the hole it deforms the hole plastically introducing compressive residual stresses. In some

cases, structural bolts can be inserted in the hole and pretensioned to provide a compressive stress field around the hole.



Figure 11. Hole drilling method to stop crack propagation; after: Dexter (2005)

2.8.2 Repair of Through-Thickness Cracks

Fully developed cracks, (through-thickness cracks) cannot be repaired simply using surface treatment methods, although hole drilling is often used to developed full through-thickness cracks.. Typically two different methods are utilized to repair these cracks; namely 1) vee-and-weld, and 2) adding doubler/splice plates. In the Vee-and-weld method, for long through-thickness cracks, the material is gouged out along the crack in the shape of 'V' and then the gouge is filled with V-shaped groove weld (i.e. the entire cracked area is filled with weld metal). Quality of the vee-and-weld is better when made in fabrication shop and it may lower in the field as it requires skilled, experienced labor as well as the environmental conditions may affect the procedure.

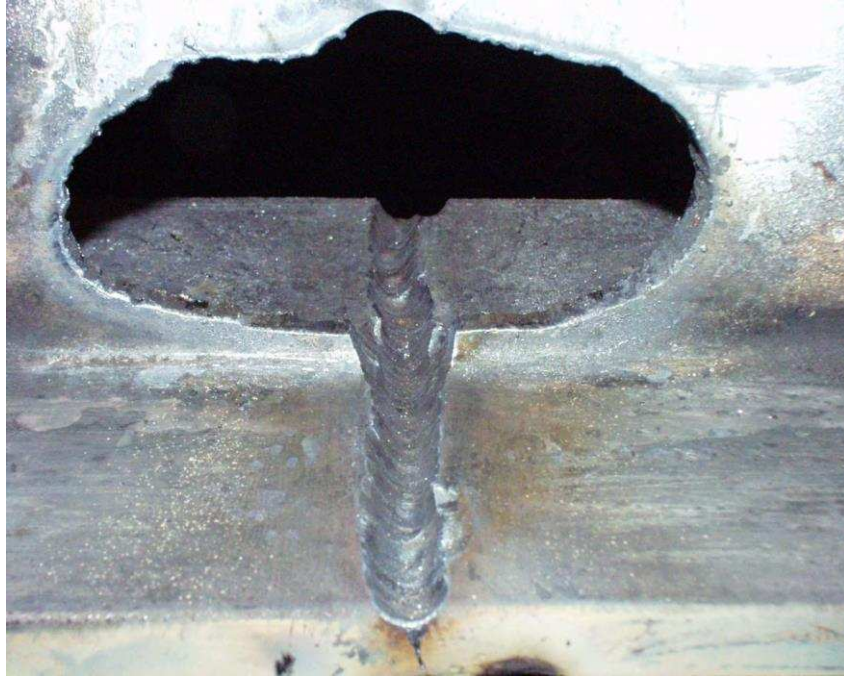


Figure 12. Vee and Weld repair method to repair through thickness cracks; after: Dexter (2005)

Doubler plates or splices is another method of repairing through-thickness fatigue cracks. These plates add extra material to the detail increasing the cross-section or provide continuity to the cracked detail (i.e. bridging the crack). The added cross-section reduces the stress range experienced by the detail. The problem with this method is that if the doubler plates are welded, the new weld might start to develop their own cracks. This is the reason bolted doubler plates are preferred over the welded doubler plates. Bolted connections are AASHTO category B. Another problem that arises by this method is that it is difficult to maintain the alignment on two sides of the cracked section before welding.

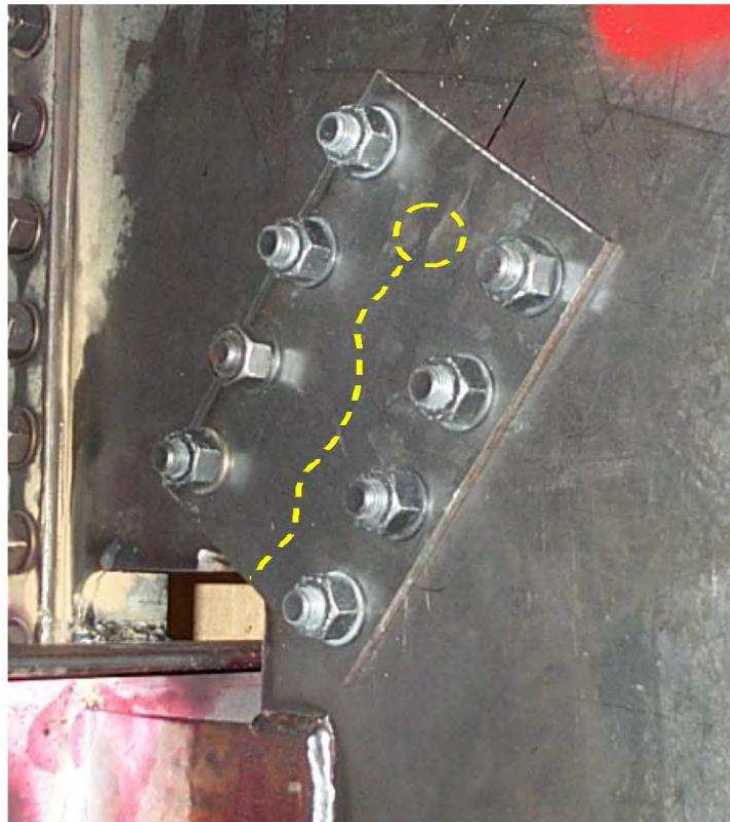


Figure 13. Addition of a doubler plate to repair through thickness crack; after Dexter (2005)

2.8.3 Modification of the detail

The notion of modifying the detail hinges on the desire to reduce the stress range in the cracked details to reduce the crack driving force. For example, if the details have sharp corners then it is highly likely that there is high stress concentration near these sharp corners. To reduce this stress concentration caused by the presence of sharp corners, the corners can be modified to be rounded in shape (i.e. introduce a transition radius to allow for smooth stress flow). The overall geometry of the detail might also be changed to reduce the stress concentration on the detail. It is very important to keep in mind that the modified details should be fatigue checked.

2.8.4 Repairs using Carbon Fiber Reinforced Polymer (CFRP) Composites

The use of fiber reinforced polymers to increase the fatigue life of the structures started in mid-1980. The main advantage of using CFRP material is that it is light weight and durable which makes it easy to handle. A recent feasibility study was conducted by Mahmoud and Riveros (2013) on the potential for using CFRP for the repair of underwater steel structures. The literature review below highlights some key studies listed in that feasibility study.

2.9 Literature Review

2.9.1 Crack growth in CFRP-retrofitted panels

There have been various studies performed to evaluate the increase in fatigue life of steel structures using fiber reinforced polymer (FRP) or CFRP (Tavakkolizadeh, et al., 2003, Alemdar, et al., 2011, Wu, et al., 2012, Yu, et al., 2014). The majority of the studies were conducted on concrete structures with limited field applications however (Shaat, et al., 2003). Unlike reinforced concrete structures, studies on the use of CFRP for repairing steel structures are scarce. The majority of existing work on metallic structures for evaluating the effectiveness of CFRP in slowing down crack growth was conducted on aluminum panels for the aerospace industry. For steel structures, research findings have shown that CFRP sheets and strips are not only effective in restoring the lost capacity of a damaged steel sections but are also effective in strengthening the sections to resist higher loads, extend fatigue life and reduce crack propagation. Following studies on use of CFRP to reduce fatigue crack propagation are presented below.

Previous studies have been performed to evaluate the potential increase in fatigue life of the steel girder by attaching CFRP strips to the tension flange. Tavakkolizadeh and Saadatmanesh (2003) assessed the effect of epoxy-bonded CFRP strips to tension flange of the steel girder on increasing the number of cycles to crack initiation. It was reported that the fatigue life of the retrofitted

specimens was approximately between 2.6 to 3.4 times that of the unretrofitted specimens for stress ranges of 345 to 207 MPa, respectively. This improvement is equivalent to upgrading the detail from the AASHTO category D to category C.

Alemdar (2011), studied the effectiveness of CFRP overlays on welded connections under fatigue loading. It was concluded that the CFRP-retrofitted pre-cracked specimen sustained an additional 2.88 million cycles after crack initiation without any measurable crack growth. This test also showed that the CFRP overlays were able to reduce the stress range at the critical point of the welded connection below the crack propagation threshold.

Chao Wu (2012) presented a study on the use of ultrahigh modulus CFRP for strengthening center cracked steel plates. In this study, an ultrahigh modulus CFRP plate with modulus of 460 GPa was used to strengthen initially cracked steel plates. Five different strengthening configurations were used by changing patch length and patch width and applying the patches on one side and both sides. The specimens were tested under fatigue loading with frequency 20 Hz, stress ratio of 0.1, and nominal stress of 150 MPa. The experimental results showed that fatigue life was 8 times more than that of the unstrengthened steel plates. It was concluded that the CFRP bond length, bond width and location have considerable influence on fatigue performance of CFRP-strengthened specimens and CFRP needs to be attached close to the crack tip to achieve better results. The specimen details and CFRP configuration are shown in Figure 14.

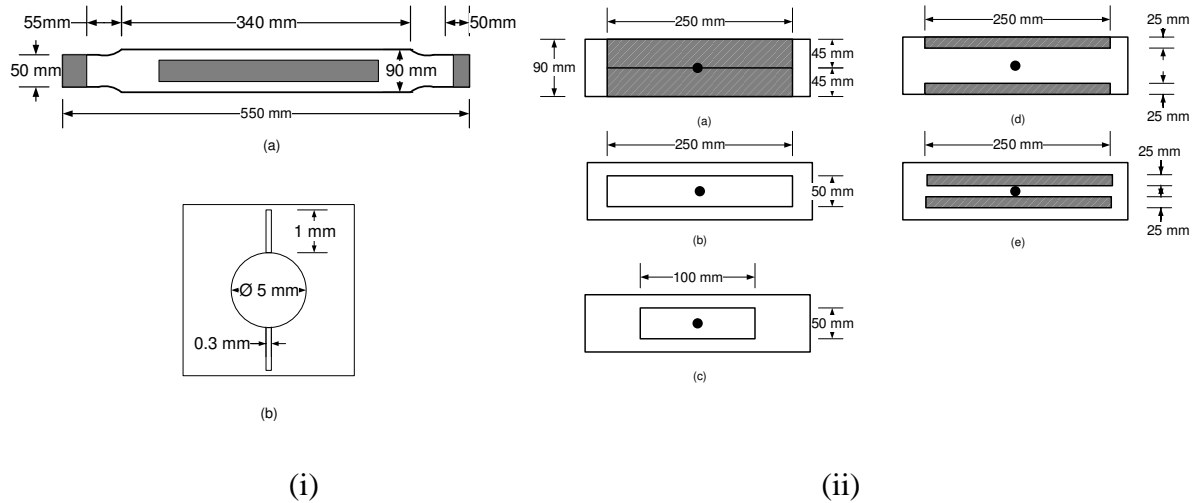


Figure 14. Chao Wu tests i) Specimen details ii) CFRP configuration; after: Wu (2012)

Yu (2014) investigated the effect of CFRP applied at different stages of crack propagation in a steel coupon. A numerical study was conducted on CFRP bonded steel plates with different degrees of damage using the boundary element method (BEM). The results of this study were then compared with experimental results which showed that the BEM might be used to investigate fatigue crack propagation in CFRP bonded steel plates. Analysis included the effect of bond length, bond width, CFRP stiffness and shear modulus of the adhesive on stress intensity factor. The specimen configuration is shown in Figure 15. Numerical model showed similar results with experimental results. It was found that the stress intensity factor is reduced with increase in shear modulus of adhesive from 0 MPa to 350 MPa. Further increase in the shear modulus did not affect the stress intensity values by much. Considerable reduction was seen after strengthening and larger cross-section and higher elastic modulus of CFRP is recommended as the reduction of stress intensity factor was observed with the increase in the same. To reduce the stress intensity factor by considerable amount, maximum possible area should be patched if not the entire plate.

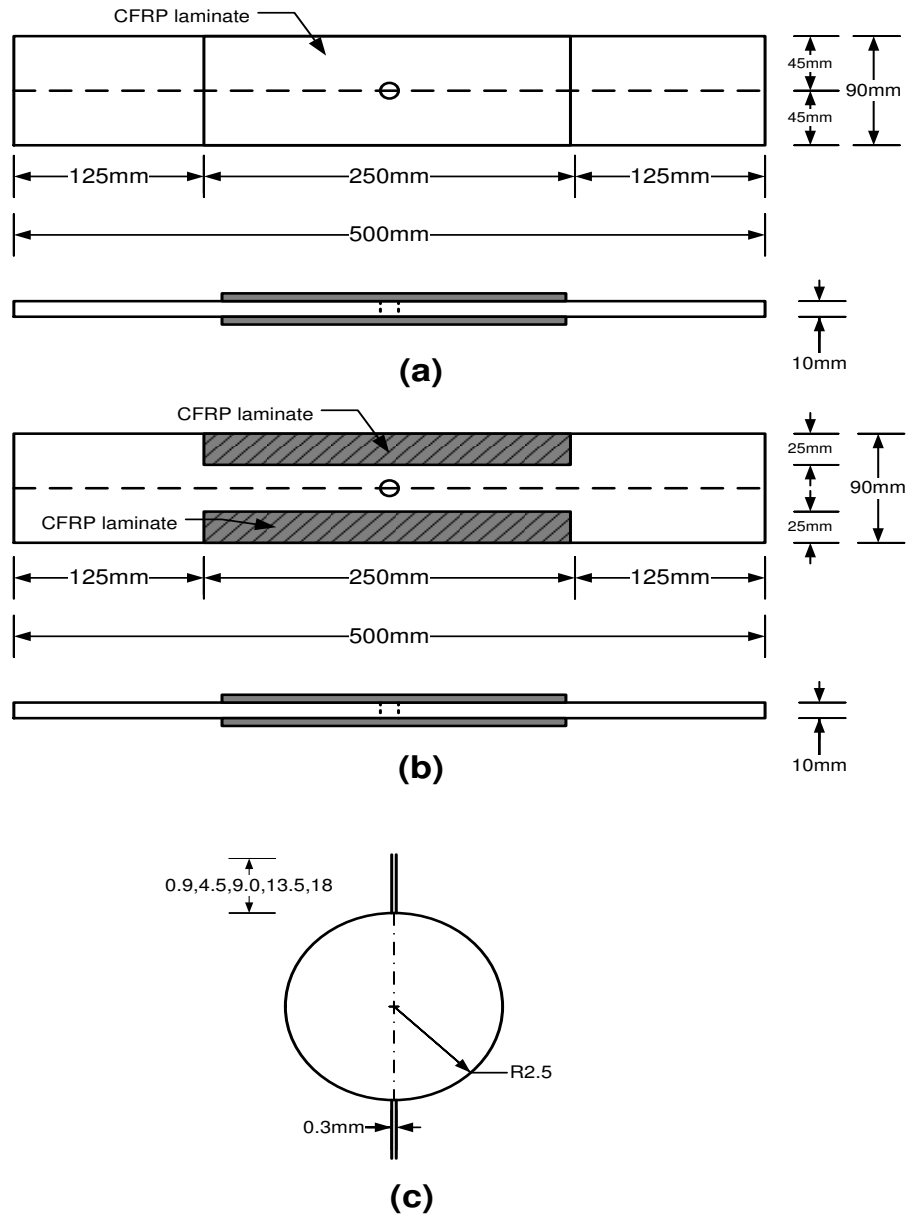


Figure 15. Specimen geometry for Yu tests (a) patch configuration A (b) patch configuration D (c) notch details; after: Yu (2014)

2.9.2 CFRP debonding and development length

Shield et al. (2003) conducted a series of experimental tests to evaluate the effective bond length of CFRP in fatigue-repaired steel girders. The effective bond length is the shortest CFRP strip length that results in the strip developing its full strength. It was concluded that the ductility of adhesive governs the effective bond length and so the ultimate strength of CFRP strips could not be achieved. In addition, the tests showed significant reduction in strain in retrofitted cracked specimens, except in the case of small cracks where it was difficult to clearly identify the benefits. Specifically, it was found that the bonded CFRP strips reduced the stresses at the crack tip by approximately 60%. The total recommended length of a one-layer CFRP strip applied for retrofit should be a minimum of 20 inches long (two 8 inch long bonded regions on either side of a 4 inch long debonded region).

Schnerch (2006) focuses on the surface preparation methods and means of preventing galvanic corrosion. Experimental research was carried out to determine the suitable adhesive by determining effective bond length or development length. Performance of the bond dictates the failure of the joints. In this study, the use of several types of adhesive showed resulted in rupture of the CFRP strips, which indicates the development of the full strength of the CFRP. It was found that the development length is proportional to the number of CFRP layers used. Analytically it was predicted that high shear stresses would develop at the end of the CFRP, which was confirmed by the experimental program in this study. Selection of the proper adhesive and surface treatments is necessary to achieve the highest bond strength.

Bocciarelli (2008) investigated the debonding strength of axially loaded double shear lap joints between steel plates and CFRP through analytical, numerical and experimental analysis. Two steel plates were joined together with two CFRP plates with epoxy making a lap shear joint with

different lengths. Steel-adhesive interface was the dominant failure. It was found that more the thickness, more will be the strength of the adhesive joints. Maximum shear stress does not depend on the geometry of the connection and might be used for designing the joint.

Wu (2011) developed a new hybrid bonded FRP technique to improve FRP debonding prevention. Bond interface is the weakest link in the joint. The new proposed hybrid system suggested by Wu is shown in

Figure 16. A thin concrete layer is peeled off before applying FRP. FRP is applied using required adhesive and mechanical fasteners are drilled through FRP to the concrete substrate. This increases the frictional resistance at the interface and in turn increasing the bond strength. It was concluded that the failure of the beam was attributed to the rupture of the FRP. Furthermore, if the number of FRP layers is increased, the higher strength of the bond is achieved.

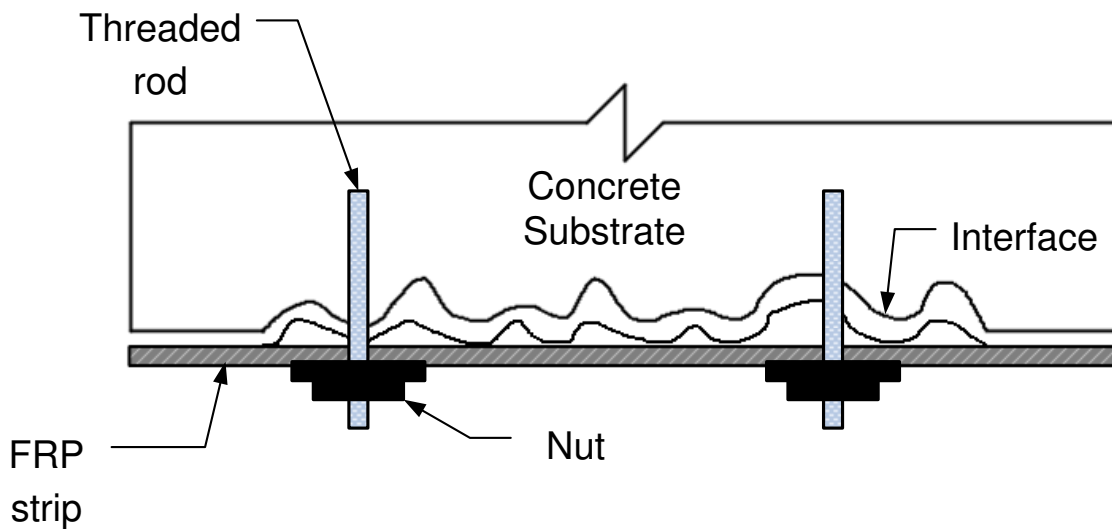


Figure 16. Hybrid bonded FRP technique (Wu, et al., 2011)

Teng (2012) studied debonding failures of CFRP-strengthened steel coupons. Considering the failure plane, debonding failures between the steel and CFRP may occur in (a) adhesive (cohesion failure), (b) at interface between the adhesive and adherends (adhesion failure) and (c) combination of the both. These different types of failures are illustrated in Figure 17. If adhesion failure controls the strength of CFRP strengthened steel coupons, the interfacial bond strength will depend on how the steel surface and the CFRP surface are treated as well as the bond capability of the adhesive. The test results showed that the grit-blasting method results in significantly higher adhesion strengths over the solvent cleaning and hand grinding methods. The test results also confirmed that there exists an effective bond length in such bonded joints beyond which any further increase in the bond length does not lead to any further increase in the bond strength but does lead to an increase in the ductility of the debonding process.

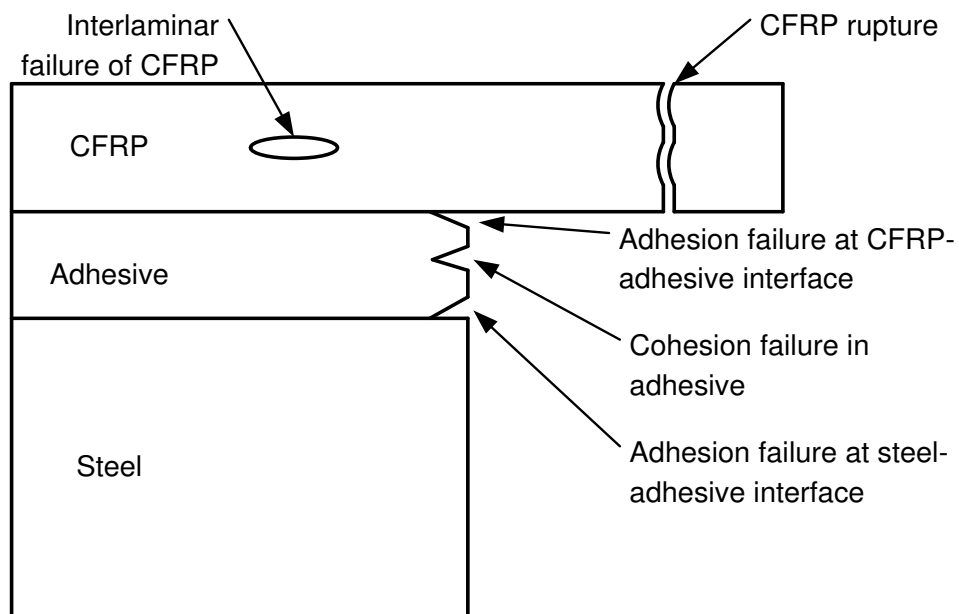


Figure 17. Possible failure modes of CFRP to steel bonded joints

Chapter 3

Experimental Test Setup

3.1 Introduction

This section explains the details of the experimental setup used including geometries of test specimens, test setup, instrumentation plan and surface preparation, mechanical properties of CFRP and adhesive used, test matrix, and testing protocol. *The test matrix was developed for seven different specimens. However, in this thesis only four were tested. The remaining three will be tested at a later stage.*

It is important to design the test setup for the required material and fatigue strength. Designing the test setup for fatigue stems from the fact that repeated cycles on the reaction frame could cause premature fatigue cracks to develop. The geometry of the test specimen was selected to allow for the application of large CFRP patches, mimicking actual field applications. To investigate strains in both the steel specimens and CFRP strips, strain gauges were installed at various locations on the specimens as well as on the CFRP. Surface preparation is an important step before installing the CFRP strips on the specimen to achieve effective bonding of the adhesive. It is also necessary to prepare the surface before installing strain gauges.

3.2 Geometric Configuration of Test Setup

Problems related to the fatigue crack propagation in the field of civil engineering are generally associated with mode I type of loading. Although this does not always hold true, it was necessary to test all the specimens under mode I to develop a baseline for evaluating the effectiveness of the proposed repair under a uniform state of stress. The thickness of the specimens were chosen to be

9.5 mm so as to correspond to a practical in typical CFRP panels. The width of the specimen was chosen to allow for the installation of large CFRP patches. A self-reacting frame was designed using the American Institute of Steel Construction (AISC) Manual (2010) to provide the required strength. All the forces applied to this frame were counter acting each other and only the dead load of the entire system was assumed to be transferred to the floor.

As seen in Figure 18, the self-reacting frame consisting of a 2.83 m (10 feet) long W610x140 (W24x94) top beam connected to two W200x59 (W8x40) columns by double angle shear connections. The angles used for shear connections were L102x102x9.5 (L4x4x3/8) with seven bolts of diameter 19 mm (3/4 in). The columns were resting on two W840x251 (W33x169) girder running parallel to each other with a center-to-center distance of 2.83 m (10 feet). Columns were connected to a base plate of thickness 51 mm (2 in) and four bolts of diameter 19 mm (3/4 in). The total length of each column was 4.27 m (14 feet). Another W610x140 W24x94 beam was connected at the bottom to the W840x251 (W33x169) girders on both sides using double angle shear connections. The angles used for shear connections were L102x102x9.5 (L4x4x3/8) with seven bolts of diameter 19 mm (3/4 in).

Since miter gates are always subjected to wet environments; hence, it was important to test the specimens under water. This was realized by building a tank made of acrylic walls 25 mm (1 in) in thickness with a steel base plate of 1.93 m x 1.93 m x 9.5 mm (76 in x 76 in x 3/8 in) connected to the top flange of the bottom W610x140 (W24x94) girder with specimen resting on this base plate. Back-to-back L133x133x13 (L5x5x1/2) angles were used to connect this whole assembly using ten 22 mm (7/8 in) diameter shear bolts and twenty 32 mm (1 1/4 in) tension bolts. The tensile stresses on the 32 mm (1 1/4 in) bolts were 172 MPa (25 ksi), each. Filler plates that are 25 mm (1 in) thick were provided on both side of the specimen between the angles to reduce the prying action

assuming these plates to be underdeveloped. See through acrylic was chosen as to allow for external monitoring of the specimens. The inside-to-inside dimensions of the tank were 1.75 m x 1.75 m x 1.22 m (68.75x68.75x48”). The acrylic sheets were connected to the base plate with four L102x102x9.5 (L4x4x3/8) angles all around the tank. The bolts going through acrylic sheets and the angles were of 13 mm (1/2 in) in diameter and the bolts going through the angles and base plate were 19 mm (3/4 in) in diameter. The sizes of these bolts were chosen such that the bolts can resist the shear force acting on the acrylic walls and the tension force acting on the base plate. To make the connections of the acrylic sheets watertight, these were covered by silicone. A hole was made in the steel base plate of the tank to empty the tank through a hose using a knob, effectively, when needed. Figure 19 shows the physical front view of the test setup including the actuator, self-reacting frame, the base plate of the acrylic tank and the tested specimen and Figure 20 shows the physical front view of the test setup including actuator, self-reacting frame, acrylic tank with water and tested specimen.

Specimens were loaded using a 980 kN (220-kip) hydraulic actuator manufactured by MTS Systems Corporation. Even distribution of the load applied by the actuator through the width of the specimen is important and to achieve this, a built-up spreader beam having five stiffeners on each side of the web was used. It was assumed that each stiffener will carry equal load and distribute it in the specimen equally. It was very important for all the welds to be smooth without having any flaw so that the fatigue problems arising due to bad weld quality would be eliminated. The Actuator was connected to top beam by connecting the actuator to a bearing plate and bolting this plate to the flange of the beam. Six bolts of diameter 22 mm (7/8 in) were used in this connection. Four 38 mm (1 1/2 in) bolts with length of 46 cm (18 in) were used to connect swivel of the actuator to the bearing plate. Eight 22 mm (7/8 in) cap screw bolts were used for the

connection between actuator and spreader beam. Spreader beam was connected to the specimen using two back to back L5x5x1/2 angles along the length of the specimen. Filler plates that are 13 mm (1/2 in) thick were used between the angles and the specimens to reduce the moment demand on the bolts connecting angles and the spreader beam, i. e., tension bolts. All bolts were pretensioned using turn-of-nut method. As per AISC, this method provides a clamping force of 70-85% of the yield stress in the bolts. Detailed drawings of test setup and connections can be found in Appendix B.

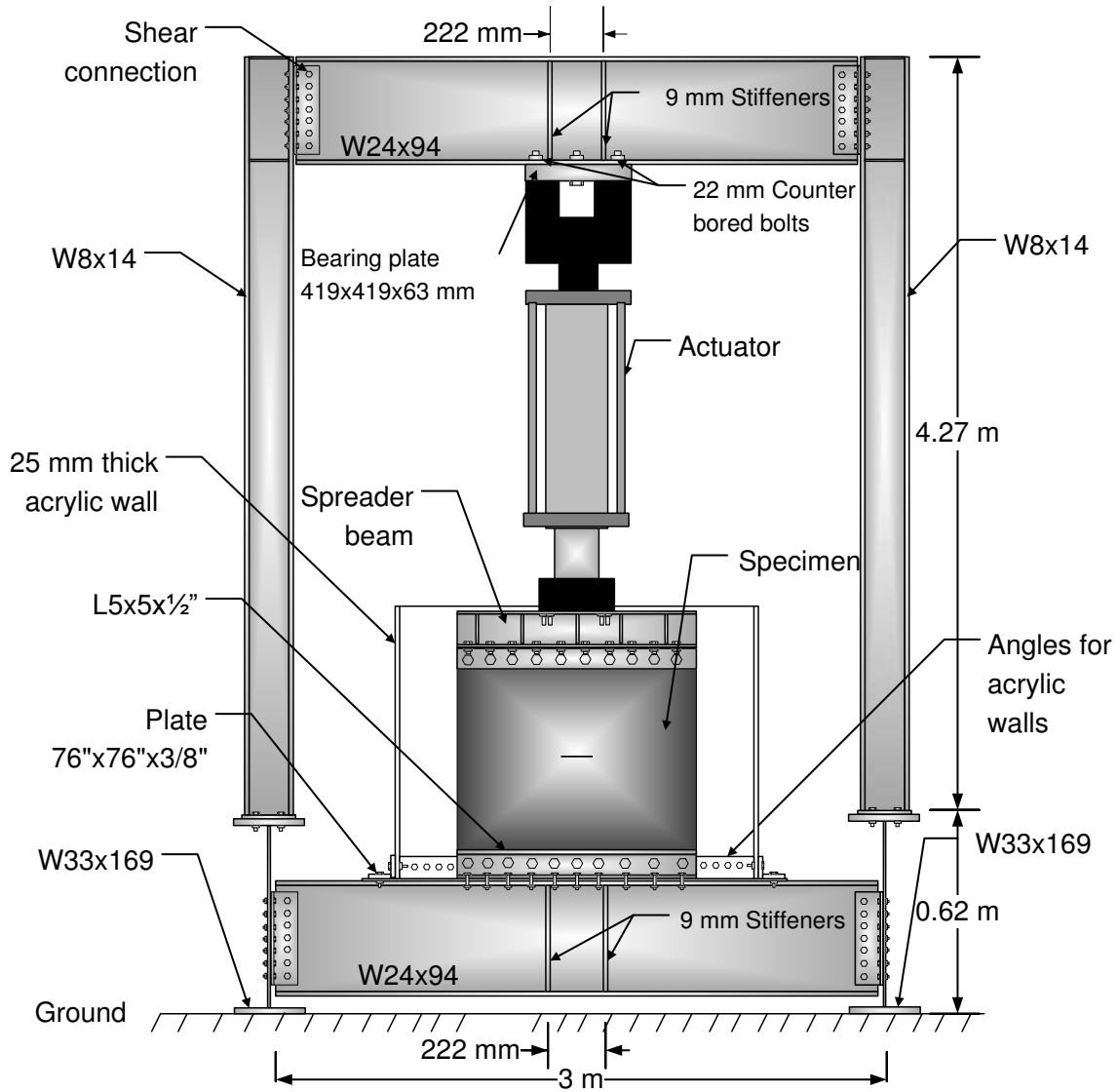


Figure 18. A geometrical drawing showing a front view of the test setup including the actuator, self-reacting frame, the acrylic tank and the tested specimen



Figure 19. A physical front view of the test setup including the actuator, self-reacting frame, the base plate of the acrylic tank and the tested specimen



Figure 20. A physical front view of the test setup including the actuator, self-reacting frame, base plate with acrylic tank with water and tested specimen

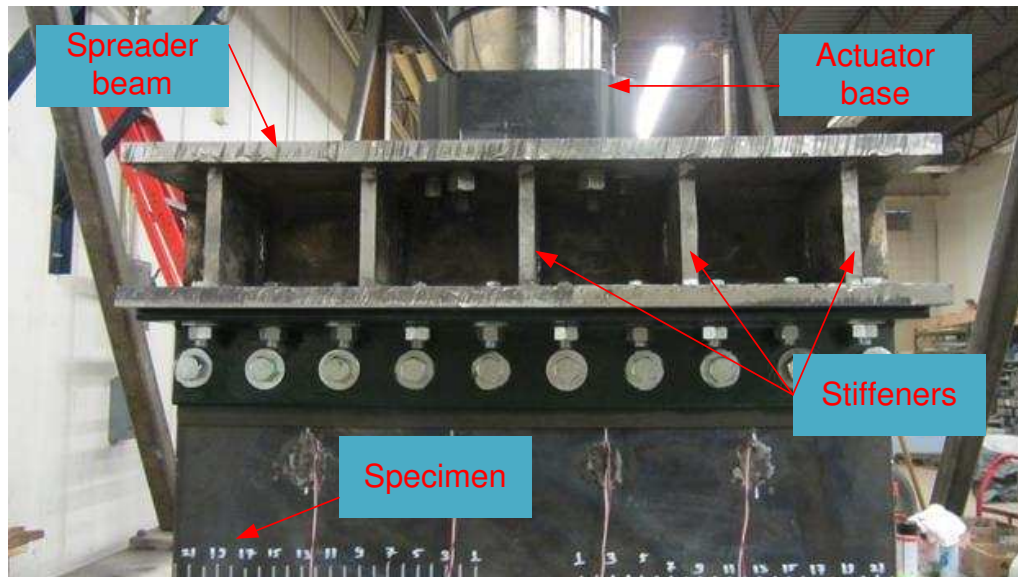


Figure 21. A physical front view of the spreader beam including the specimen, the angle connecting the specimen and actuator

Underwater test was conducted for specimen 4. Since miter gates are built in rivers which bring in fluvial sediments as well as salt in the catchment area. River flow erodes the rocks at the river bed. Salts and sediments get carried away in the river water from erosion. Concentration of NaCl salt in river water is less as compared to that of seawater. Seawater contains NaCl salt concentration of 35 g/l. This concentration of seawater was used in this study to investigate the worst case possible. Effect of these parameters on the performance of the applied CFRP needs to be investigated. This was realized by adding a 90 kg (200 lbs) NaCl salt and similar amount of sand with particle size of 0.45-0.55 mm was introduced in the tank. The sand and salt used in this study can be seen in Figure 22 (a) and (b), respectively. The size of the sand particles is supposed to represent the fluvial sediments that are typically suspended in river water. The total volume of water was 2306 liters, i.e., the height of water inside the tank was 76 cm (30 in). To circulate the

water and keep these sand particles suspended, a propeller of diameter 30 cm (12") was built on a frame inside the tank as shown in Figure 23.



Figure 22. (a) 0.45-0.55 mm sand used (b) 23 kg (50 lbs) NaCl salt blocks

This propeller was placed in one corner of a tank facing the back face of the specimen in 45 degrees. The distance of the propeller from the base plate was adjusted such that its center will be at the same height (50 cm) as the crack from the base plate. Motor of the propeller was selected such that propeller would experience 500 rotations per minute. The tank was divided in two halves using similar acrylic as the tank walls. This was done so that only back face of the specimen would get bombarded by the suspended sand particles. Salt would affect both front and back faces as it was dissolved in the water. Calculations for the amount of sand required can be found in Appendix A.

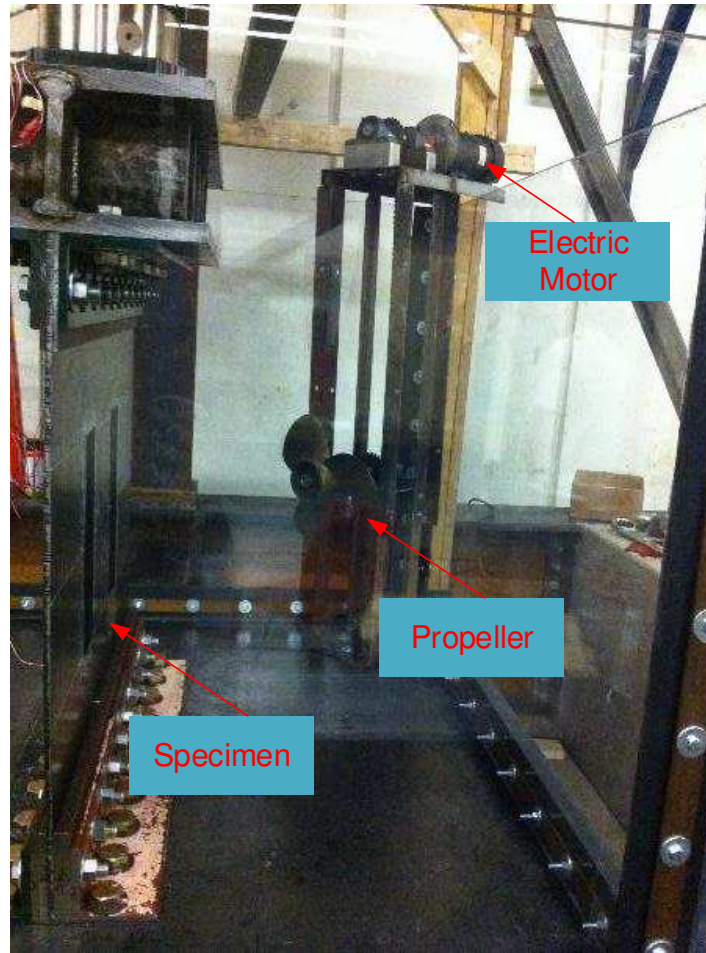


Figure 23. Propeller with electric motor in the tank facing back face of the specimen 4 at 45^0

3.3 Instrumentation Plan and Crack Measurements

Bondable 3-wired, linear strain gauges, designated as WK-06-125BT-350/W with 350Ω , manufactured by Micro Measurements were installed at various locations on the specimens as shown in Figure 24 and Figure 25 for specimen 1 and specimens 2, 3 and 4, respectively. The locations of strain gauges were selected to evaluate the stress distribution and shear lag. Strain gauges were also installed along the crack plane to allow for the assessment of the increase of stresses as the crack approaches the gauges. It was expected that the force transferred by spreader

beam will be equally distributed through the cross section of the specimen. Prior to installation, residues on the specimen surface were removed using CSM-2 degreaser, MCA-2 conditioner A and M-PREP neutralizer 5A. The gauges were bonded to the specimen using a GAK-2-AE-10 kit, provided by the Micro Measurements. To protect it from the water in the tank, gauges were covered with M-COAT J-3 polysulfide kit and then covered with M-COAT W-1 wax, also provided by Micro Measurements.

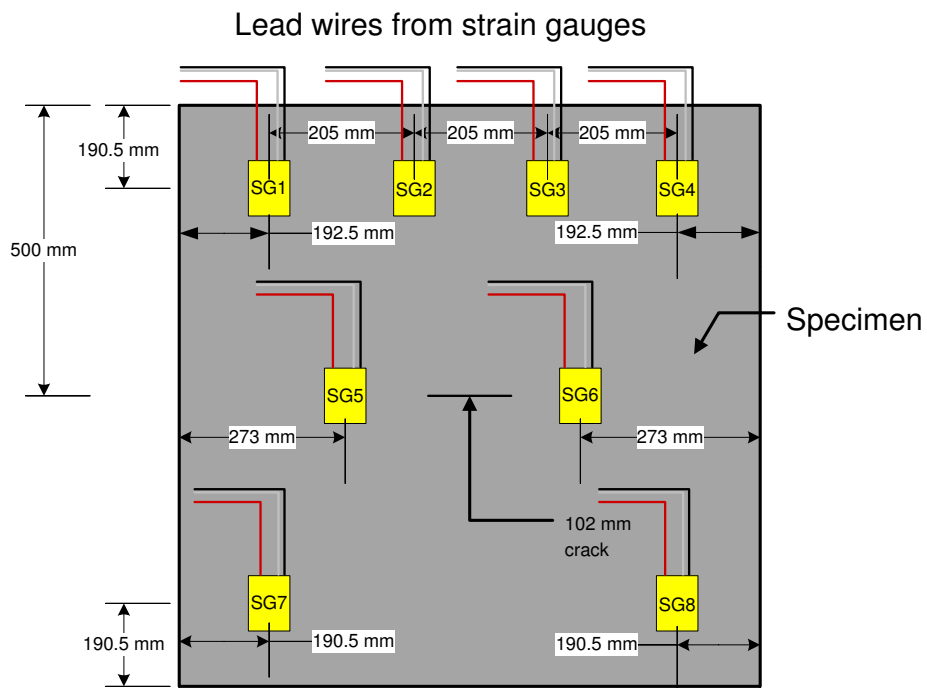


Figure 24. Locations of strain gauges (SG) on specimen 1

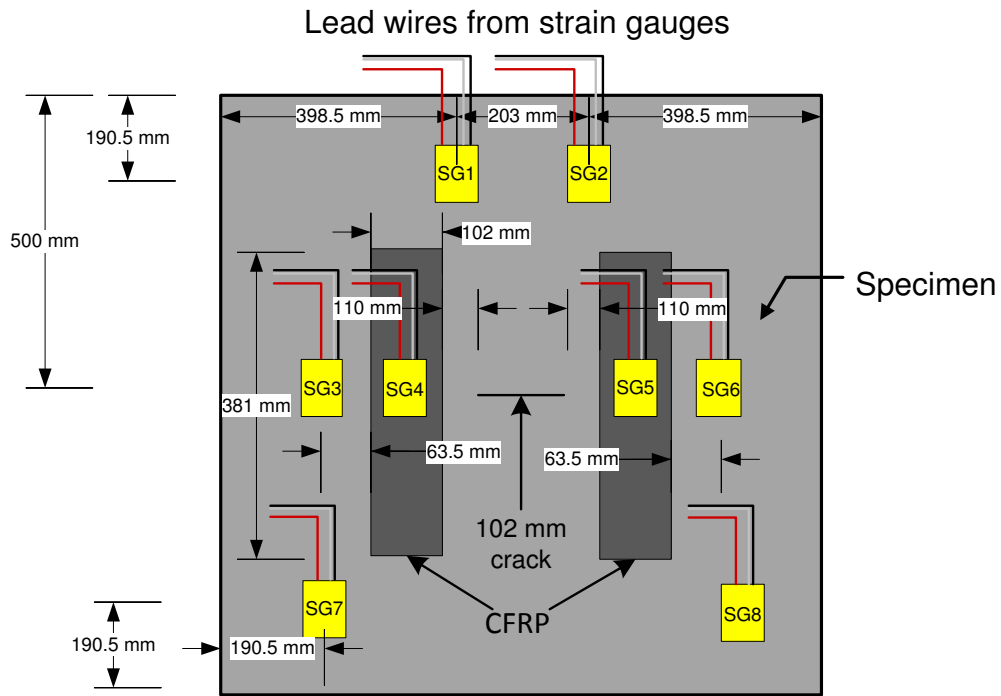


Figure 25. Locations of strain gauges (SG) on specimen 2 through specimen 3

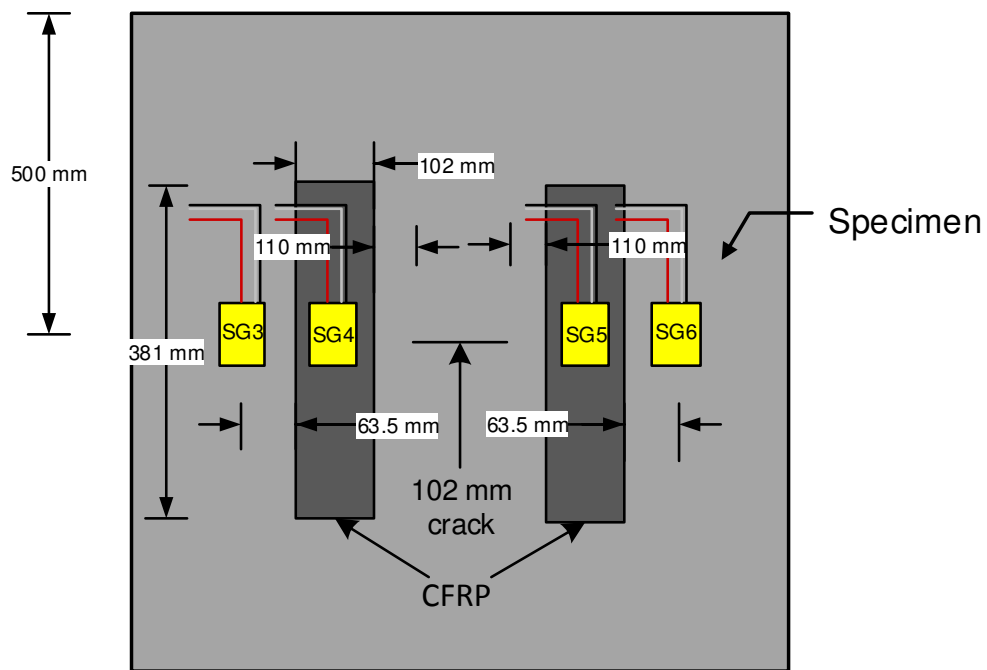
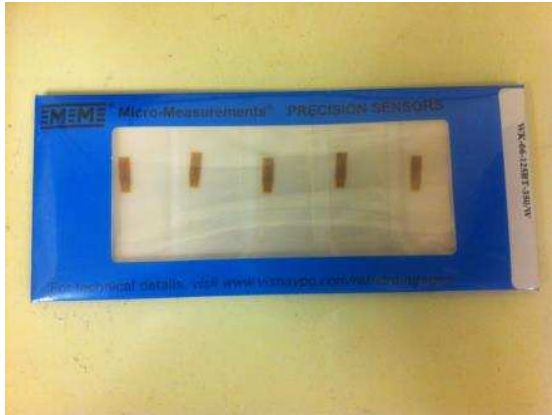
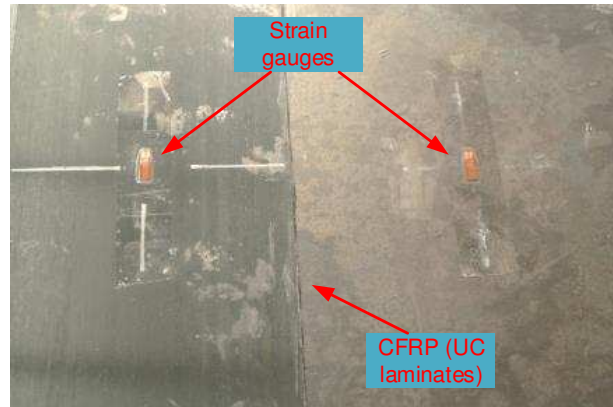


Figure 26. Strain gauge locations on specimen 4 (Front face)



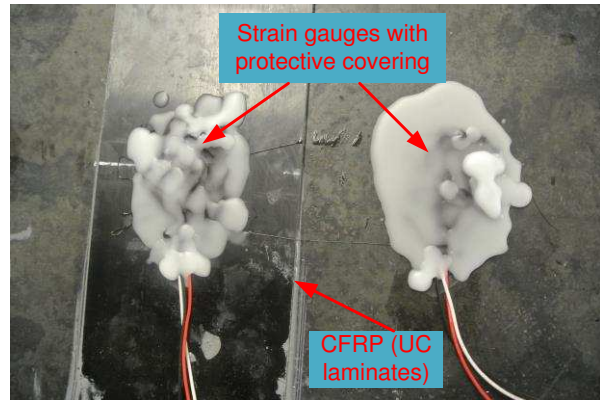
(a)



(b)



(c)



(d)

Figure 27. Strain gauge installation (a) Strain gauges from micro measurements (b) Strain gauge on the specimen and CFRP after installation (c) Soldering lead wires for strain gauges (d) Protective covering for strain gauges

Figure 28 (a) and (b) show a schematic of strain gauge and a typical strain gauge, respectively. The installed gauge on the specimen included a protective covering to prevent water seepage into the gauge as shown in Figure 28 (b). Soldered lead wires from the strain gauges were connected to Campbell Scientific CR1000 data acquisition system to obtain the axial strains in the specimens from each gauge at different locations. Another CR1000 was used, for collecting the displacement and force feedback from the MTS actuator through the MTS 407 controller. Figure 29 shows a

schematic of the data flow and the data acquisition system (DAQ). An actual photo of the data collection set up is shown in Figure 30.

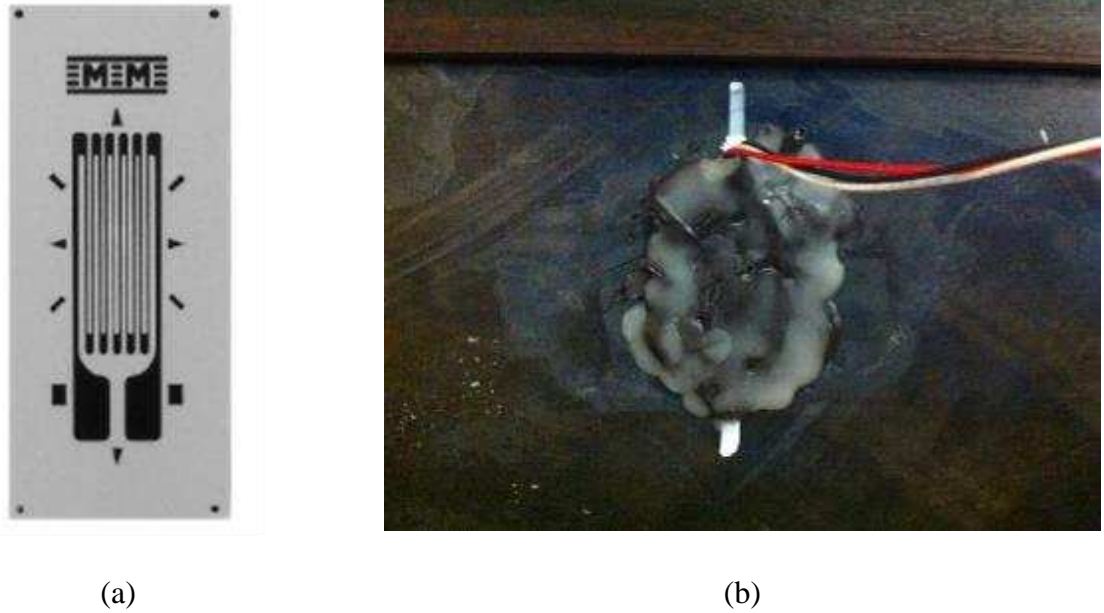


Figure 28. (a) Typical linear strain gauge used (b) Protective covering for strain gauges after installation on the specimen

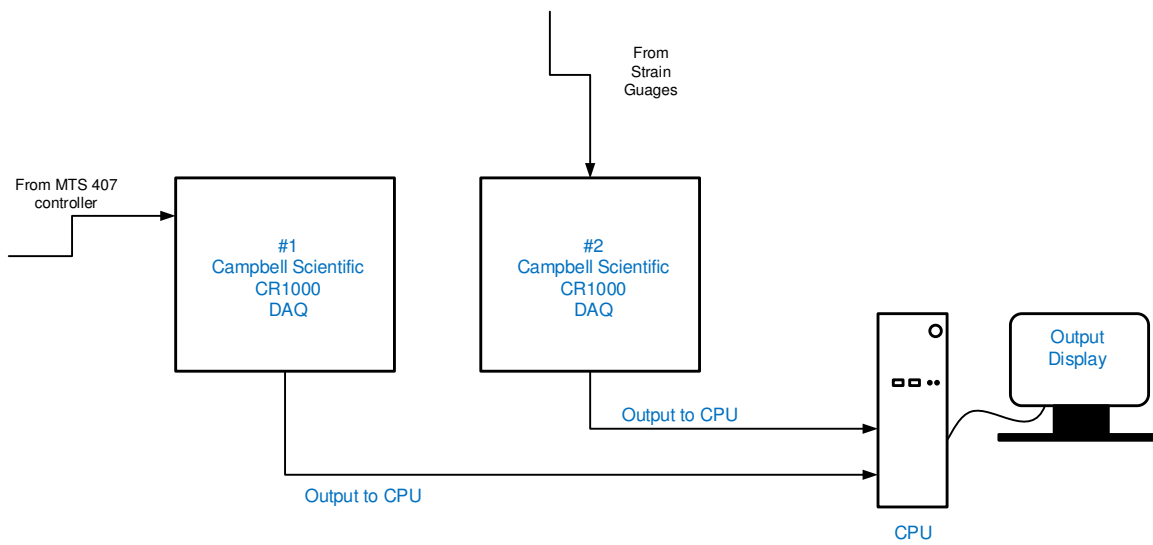


Figure 29. Schematics of data flow and the DAQ system

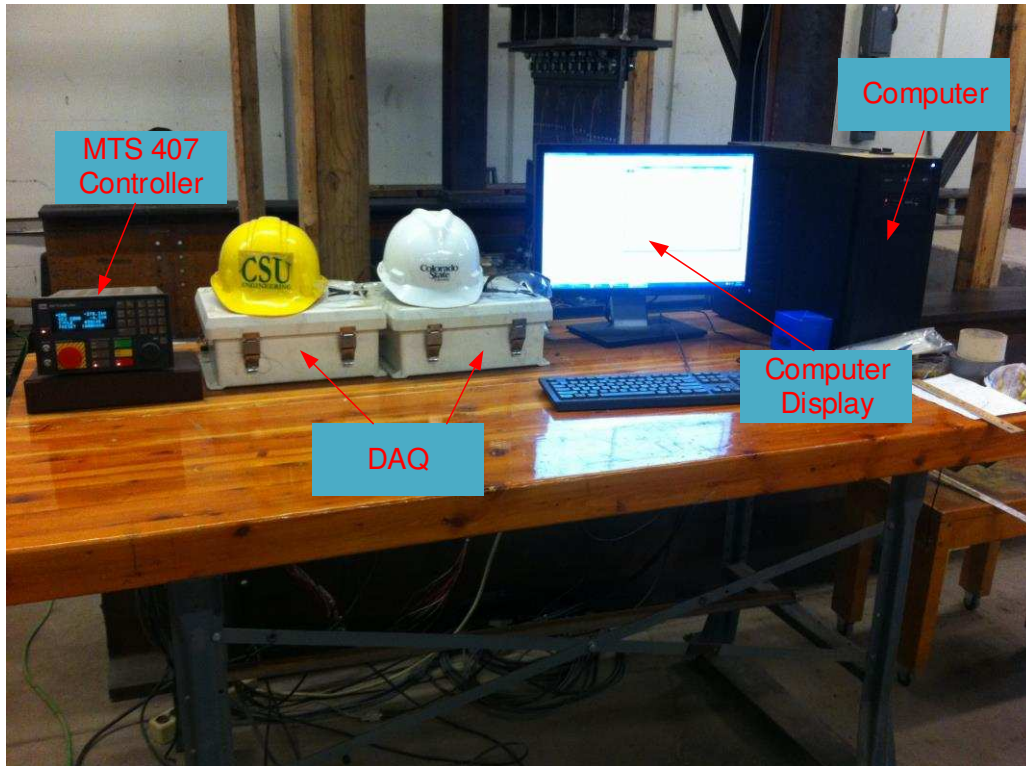


Figure 30. Setup comprising of MTS 407 controller, two DAQ systems and a computer for data collection

Crack length was measured by vertically marked grid lines on the specimen. To mark these lines a permanent oil paint marker was used. Every line was spaced with a distance of 2 cm each on both sides of the crack so the length of the propagating crack can be measured, effectively. A regular ruler was used to measure the distances between these lines. These grid lines can be seen in Figure 31.

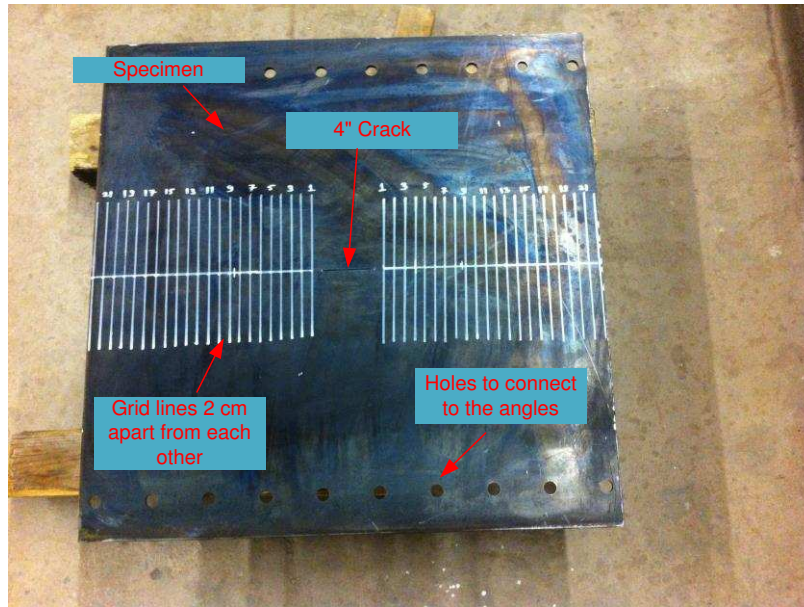


Figure 31. Grid lines marked 2 cm apart on the specimen to measure the half crack length on either side of the crack

To facilitate faster initiation of the crack growth, tack welds were introduced at the crack tips. Tack welds are considered to be worst fatigue category i.e, category E' with constant amplitude fatigue limit of 18 MPa (2.6 ksi). A typical tack weld at the crack tip is shown in Figure 32.

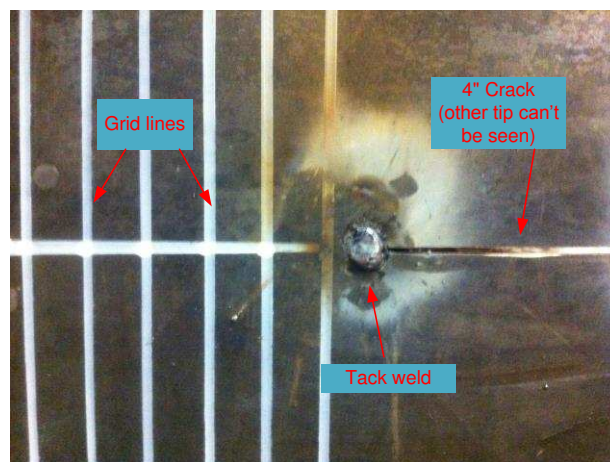


Figure 32. Tack weld introduced at crack tip to facilitate faster crack growth

3.3.1 CFRP installation and surface preparation

CFRP and strain gauge installation procedure is of great significance since improper installation can result in de-bonding of the CFRP and ineffectiveness of the strain gauges. The application procedure used to install CFRP and strain gauges is explained as follows:

3.3.1.1 CFRP installation

Surface preparation consisted of grinding the steel specimen (Figure 33), cleaning the grounded surface and CFRP surfaces with acetone, mixing the adhesive resin and hardener in equal proportions of weight using a mixer, applying adhesive on the appropriate surfaces using a spatula, installing the CFRP at the required location on the specimen and compressing the CFRP until the required thickness of the adhesive is achieved. Grinding the steel specimen is done until a rough surface is achieved so that the possibility of de-bonding of the adhesive will be lowered after removing the oxide coating of steel specimen.

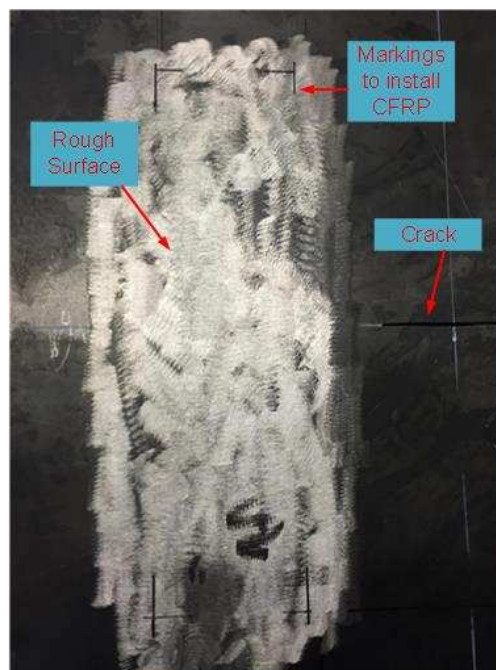
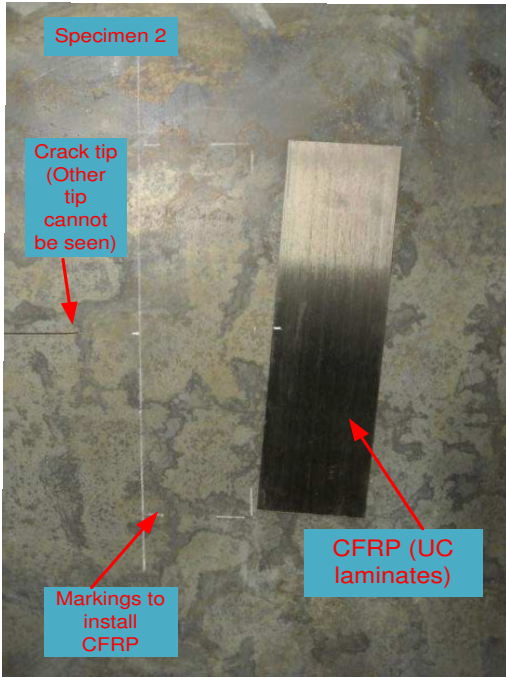


Figure 33. Prepared surface before installation of CFRP

Specimen 2 was not grinded at first, to investigate the effect of bonding of adhesive on the oxide coating. Specimen 3 and Specimen 4 were grinded before starting the tests. Cleaning with acetone is done so that the minute dust particles will be removed to achieve the effective bonding of adhesive to the steel surface and CFRP. On either faces of the specimen, two different methodologies were adopted to apply adhesive to install CFRP. On one face, the adhesive was applied on the steel and then CFRP was installed on the plate. On the other face it was applied on the CFRP and then the CFRP was installed on the plate. This was done to investigate the effect of the installation method on debonding of the CFRP. After installation of the CFRP, the adhesive is compressed before it hardens and the thickness is measured using a height gauge. Concrete blocks are placed on the CFRP to avoid any expansion of the adhesive. A series of photos of CFRP installation are shown in Figure 34.



(a)



(b)



(c)



(d)

Figure 34. CFRP installation on specimen 2 (a) Markings on the specimen to install CFRP (b) preparation of adhesive (c) applying adhesive on the CFRP (d) CFRP on specimen after installation

3.4 Mechanical properties for CFRP and adhesive

Two types of CFRPs, namely Tyfo UC laminates and Tyfo SCH-41 sheets, manufactured by Fyfe Co., LLC were used in this study. CFRP is a highly orthotropic material having the highest strength in the direction of fibers. It was important to orient the CFRP such that the maximum strength and stiffness are utilized. This was done by bonding the CFRP to the specimen such that the carbon fibers will be perpendicular to the crack growth. Thicknesses of the CFRP composites depend on the type used. Tyfo UC laminates were 1.4 mm thick and Tyfo SCH-41 sheets were 1 mm in thickness. Detailed drawing of the location of the CFRP attached to the specimen is shown in Figure 35.

It was necessary for the adhesive chosen to be effective underwater and for this Hudco Formula 3200 underwater adhesive was used. This adhesive has the ability to cure underwater. It is 100% solids, two-component system, which when mixed in the ratio of 1 part resin to 1 part curing agent (hardener), by weight or by volume, yields a smooth non-sagging paste. It was not possible to engage the full strength of the CFRP as the adhesive had lower tensile strength than the CFRP. Mechanical properties of CFRP and adhesive provided by manufacturer are tabulated in Table 3. This might be irrelevant when the crack is short in length but would have a large effect for longer cracks.

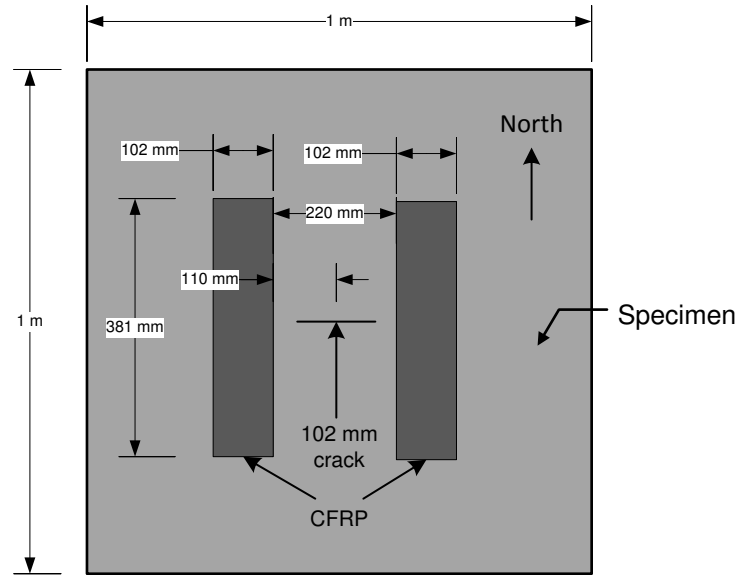


Figure 35. CFRP bonded to specimen 110 mm from the center of the crack

Table 3. Mechanical properties of CFRP and adhesive provided by manufacturer

Material	Density(g/cm ³)	Young's Modulus(GPa)	Poisson's Ratio
Steel	7.75	200	0.3
Tyfo UC Laminates (CFRP)	1.8	139.6	0.4
Tyfo SCH-41 (CFRP)	1.74	82	0.4
Hudco Formula 3200 (Adhesive)	1.35	0.14	0.4
Tyfo S (Adhesive)	1.11	3.18	0.4

Hudco Formula 3200 has very low modulus of elasticity and was not recommended to be used for CFRP installation. Investigation was carried out for this adhesive as it sets underwater

3.5 Test Matrix

Four 1m x 1m x 9.5mm specimens were tested under cyclic fatigue loading. Following nomenclature is used through-out the report. Nomenclature for the specimens, as shown in Figure 36, was done based on the specific CFRP type used, type of adhesive, and bond length.

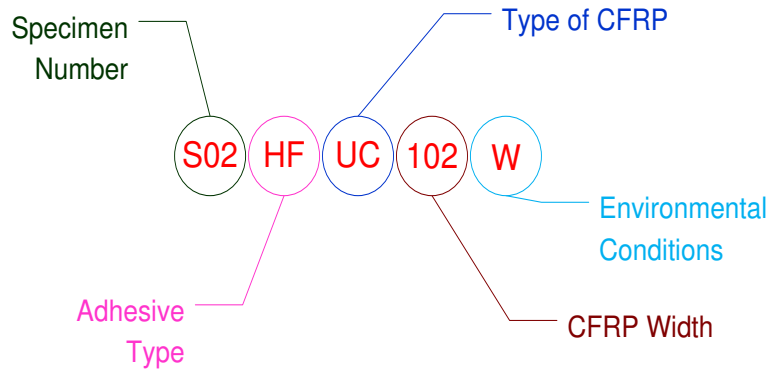


Figure 36. Specimen nomenclature

Table 4. Test Matrix

Specimen	Nomenclature	CFRP Width (mm)	Type of CFRP	Bond Length (mm)	Environmental Condition
Specimen 1 (Finished)	S01-NA-NA-0NW	NA	NA	NA	No water
Specimen 2 (Finished)	S02-HF-UC-102NW	102	Tyfo UC laminates	381	No water
Specimen 3 (Finished)	S03-S-SCH-102NW	102	Tyfo SCH-41 sheets	381	No Water
Specimen 4 (Finished)	S04-S-SCH-102W	102	Tyfo SCH-41 sheets	381	Underwater
*Specimen 5	S05-NA-NA-0W	NA	NA	NA	Underwater
*Specimen 6	S06-S-SCH-102W	204	Tyfo SCH-41 sheets	381	Underwater
*Specimen 7	S07-S-SCH-102*W	102	Tyfo SCH-41 sheets	381	Underwater

*Note: Specimen 5, 6, and 7 will be tested at a later stage.

S01-NA-NA-0NW – Control specimen, no CFRP, not underwater.

S02-HF-UC-102NW - Tyfo UC laminates, 102 mm (4”) CFRP width, 381mm (15”) bond length, not underwater.

S03-S-SCH-102NW - Tyfo SCH-41 sheets, 102 mm (4”) CFRP width, 0.5 mm (0.02”) of adhesive thickness and 381 mm (15”) bond length, not underwater.

S04-S-SCH-102W - Tyfo SCH-41, 102 mm (4”) CFRP width, 381 mm (15”) bond length, underwater.

S05-NA-NA-0W – No CFRP, underwater

S06-S-SCH-102W - Tyfo SCH-41, 204 mm (8”) CFRP width, 381 mm (15”) bond length, underwater.

S07-S-SCH-102*W - Tyfo SCH-41, 102 mm (4”) CFRP width, 2 layers of CFRP, 381 mm (15”) bond length, underwater.

3.6 Testing Plan and Loading Protocol

Testing of all specimens was commenced by conducting three shakedown tests. First two shakedown tests were done using static tension loading with the load increasing from 30 kN to 510 kN. Following the static shakedown, a cyclic test is conducted in which the specimens are subjected to few numbers of cycles with the load ranging from 30 kN to 510 kN in tension. The intention of the initial shakedown and cyclic tests is to allow all frame components to come to full contact with each other and evaluate the load path in the system. Following the first shakedown test, all bolted connections were tightened to ensure that all bolts are fully pretensioned so as to

eliminate the potential of fatigue failure of bolts. The shakedown tests were conducted under force control where the specified forces were incrementally increased in each shakedown test.

Following the initial shakedown, the cyclic tests were conducted under force control such that the stress range in each specimen is set at 55 MPa (8ksi) in which a maximum applied load resulted in a 55 MPa stress and the minimum applied load resulted in a zero stress (i.e. the stress ratio, $R = \sigma_{\min} / \sigma_{\max}$ was 0). The reason for conducting the tests under force control was to ensure a constant nominal stress range on the specimen as the crack becomes longer. If the test was conducted under displacement control, the nominal stress range would decrease as the crack propagates. Fatigue loading was applied using double servo valve 220-kip hydraulic actuator with frequency of 0.5 Hz. A MTS 407 controller was used to send the command signal to the 220kip actuator. The displacement and force feedback of the actuator were received back by the controller and the feedback from the actuator is subsequently sent to the Campbell Scientific CR1000 data acquisition system which was connected to a computer to record the data.

Chapter 4

Experimental Results and Observations

4.1 Introduction

For all the specimens, data for half crack length (a) versus number of cycles (N) was recorded. These plots are intended to show the effect of CFRP on the propagation rate of the crack with reduced propagation rate near the CFRP when compared to specimen 1 (control specimen without CFRP). It has already been discussed in chapter 2 that there is scatter in fatigue data and hence for the center crack tension (CCT) panel of Specimen 1, a log-log plot of crack propagation rate (da/dN) versus change in stress intensity factor (ΔK) was generated to obtain the 'C' and 'm' constants of the Paris law. It is not possible to generate this plot for the specimens having CFRP without numerical analysis as the effective ΔK is influenced by the presence of CFRP.

As the crack propagated in specimens with CFRP, it was important to record the strain values for the corresponding CFRP as the crack propagated and interacted with the CFRP. For specimens with CFRP, data for half crack length versus strain in the corresponding CFRP was collected. This plot was selected to investigate the maximum strain attained by the CFRP as the crack interacted with CFRP.

As mentioned in Chapter 3, four specimens were tested with different types of CFRP and varying adhesive in different environmental conditions. Dimensions of each specimen were 1m x 1m x 9.5mm. All tests were conducted under force control, such that stress range of 55 MPa (8 ksi) was maintained in each specimen throughout the corresponding tests. Fatigue loading was applied using double servo valve 220 kip actuator with frequency of 0.5 Hz.

4.2 Test results for Individual Specimen

Following sections discuss the results for individual specimen. It should be noted that while shakedown tests were conducted for all the specimens, only one shakedown test for specimen 1 is documented herein. Shakedown tests for specimen 2 through 4 are similar to specimen 1 and hence are not presented.

4.2.1 Test Results and Observations for Specimen 1

It was necessary to check the reliability of the selected self-reacting frame under applied load from performance perspective such as strength of the components and the bolted connections and the response of the actuator. As indicated in section 3.5, three shakedown tests were conducted before commencement of the actual cyclic fatigue test. Strain gauge data was collected during these tests to check the load path in the specimen. Figure 37 shows the locations of the strain gauges on specimen 1.

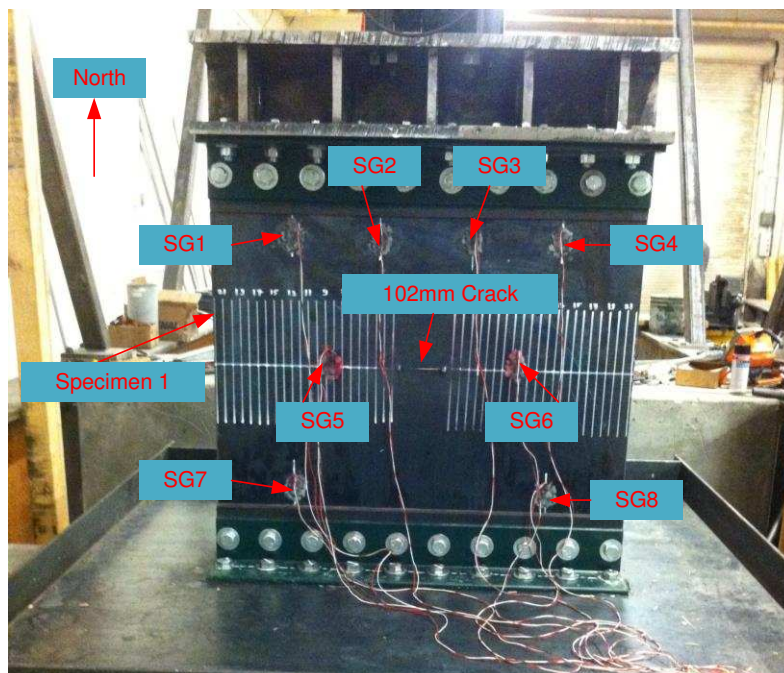


Figure 37. Strain gauge (SG) locations on specimen 1

4.2.1.1 Strain Gauge Results for the Shakedown Tests

Strain gauge data was recorded for every shakedown test and the linear stress-strain relationship was obtained. As mentioned in section 3.5, the frame needed to readjust itself so that all the components were in contact with each other. This is clear in Figure 30 where the response of the gauges is bilinear. The initial portion of the response is a result of the adjustment of the frame (i.e. slip is occurring between components and elements, etc.) and the second portion is due to full transfer of load in the specimen. As can be seen from Figure 37, total eight strain gauges were bonded to the specimen at different locations and also the local coordinates were assumed on the specimen with north being pointing upward. Figure 38 shows the plot of stress versus strain relationship. It is worth noting that the initial strain offsets were not removed since the slope of the plotted curves is the relevant parameter for comparison. As can be seen in Figure 30, the curves for strain gauge 5 and 6 showed very similar slopes as compared to theoretically calculated slope i.e., approximately 20-30%. These strain gauges were selected as the main strain gauges through which achieving a strain of $275\mu\epsilon$ corresponding to 55 MPa (8 ksi) stress range is confirmed. Strain gauges 5 and 6 were important because they were positioned such that they will be aligned with the crack and were far from any supports which might introduce higher strains than the nominal. The strain data measured by strain gauges 1 through 4 were similar and those measured by strain gauges 7 and 8 were similar. Although one would expect all these strain gauges to show similar strain values, except for strain gauges 5 and 6, the reason they did not can be attributed to the fact that strain gauges 1 through 4 were very close to the spreader beam having a very large bending stiffness as compared to strain gauges 7 and 8 which were very close to the W24x94 beam at the bottom having comparatively less bending stiffness. Strain gauges 5 and 6 should show different strain data than the others due to the presence of the crack at the center of the specimen which

introduces high stress concentration at the crack tips; hence influencing the strain values in the strain gauges at the same horizontal plan.

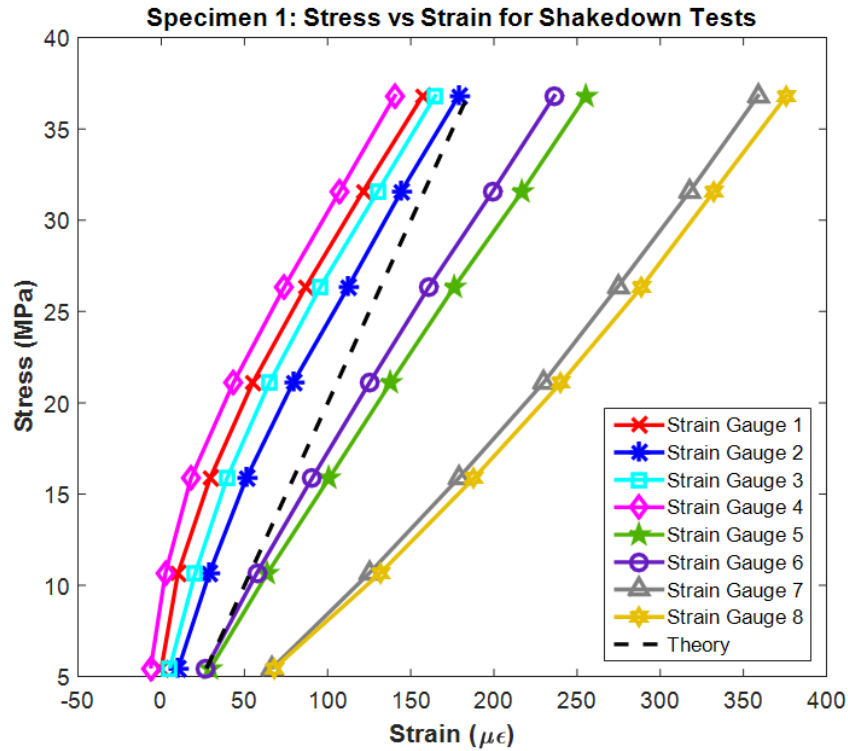


Figure 38. Stress vs. Strain data from strain gauges installed at various locations on specimen 1

4.2.1.2 Crack Length versus Number of Cycles for Specimen 1

Crack length was measured as the crack propagated along the specimen width and the corresponding number of cycles, showed on the MTS 407 controller, were recorded. Initially, the crack propagation was faster due to the presence of the tack welds at the crack tip. As the crack grew away from the tensile residual stress field introduced by the tack weld, it showed a stable/slower propagation. The fatigue life of the specimen was dominated by the stable crack growth. Near the end of fatigue life, unstable growth was noted as the crack reached its critical

length. Both, east and west cracks showed similar behavior for half crack length versus number of cycles emphasizing the even stress distribution imposed on the specimens. Figure 39**Error! Reference source not found.** shows half crack length vs number of cycles on west and east side of the specimen. As can be seen from the figure, the plots are exponential curves with crack growing in an unstable manner after reaching a critical length of around 300 mm (≈ 12 in). The total number of cycles required for the half crack to reach full width of the specimen was 439,140.

After fracturing the specimen, the crack surfaces were studied and it was found that the crack grew in stable manner, obeying laws of LEFM for 152 mm (≈ 6 in) showing flat and smooth surface with chevron marks which can be attributed to brittle crack extension. As the crack grew further from 152 mm to 300 mm, the surface showed slanted face as well as chevron marks indicating combined brittle-ductile (i.e. transition) crack growth After 300 mm (≈ 12 in), the crack surface showed shear lips as well as necking indicating pure ductile failure. The crack surfaces after fracturing the specimen can be seen in Figure 40 through Figure 42, for west half crack.

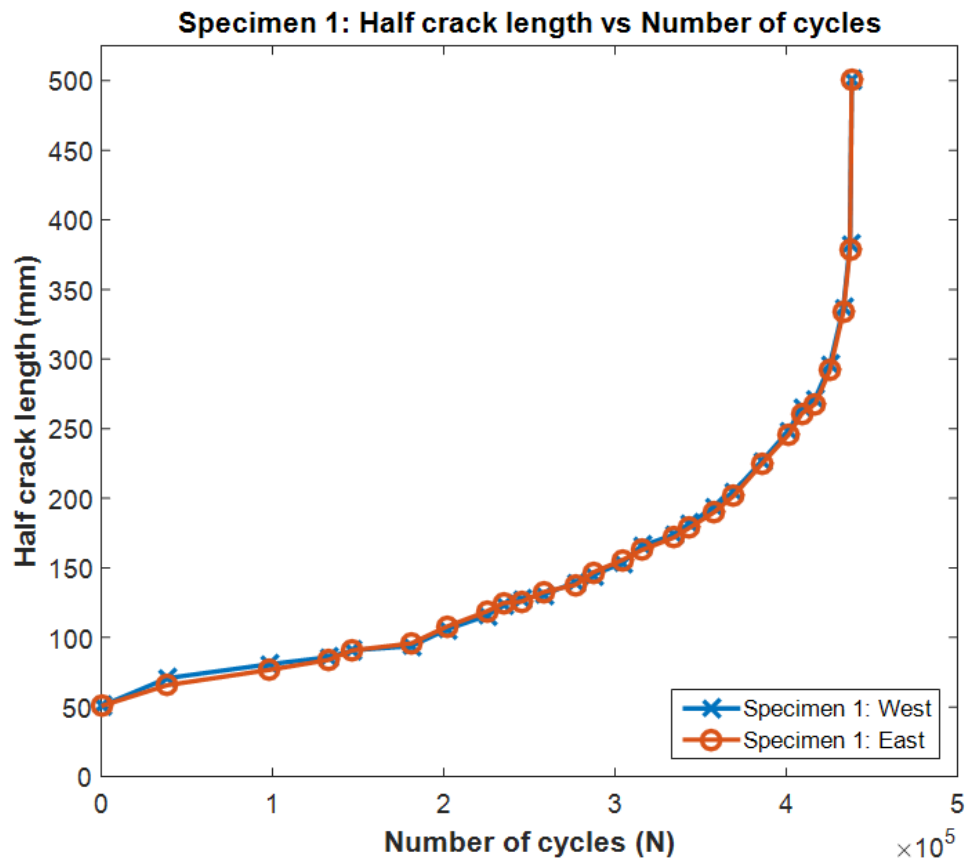
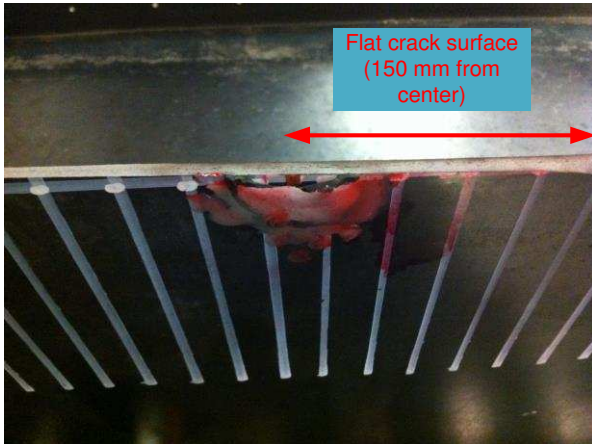


Figure 39. Half crack length vs Number of cycles for Specimen 1



(a)

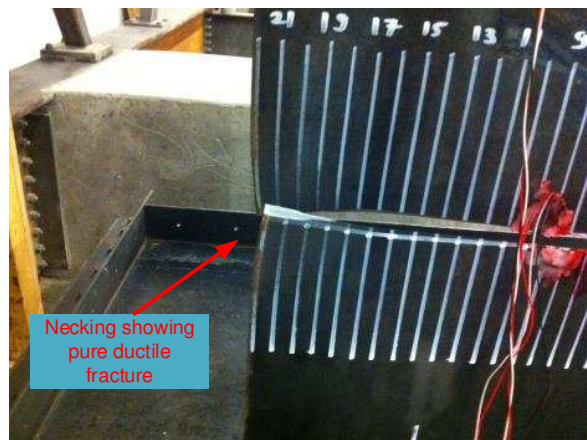


(b)

Figure 40. Crack surfaces for west half crack after fracturing the specimen 1 (a) Flat crack surface up to 150 mm from the center showing brittle fracture (b) Slightly slanted crack surface from 150 mm to 300 mm indicating ductile-brittle crack extension



(a)



(b)

Figure 41. Crack surfaces for west half crack after fracturing the specimen 1 (a) Shear lips form 300 mm to 500 mm indicating pure ductile fracture (b) Necking of the specimen indicating ductile crack extension

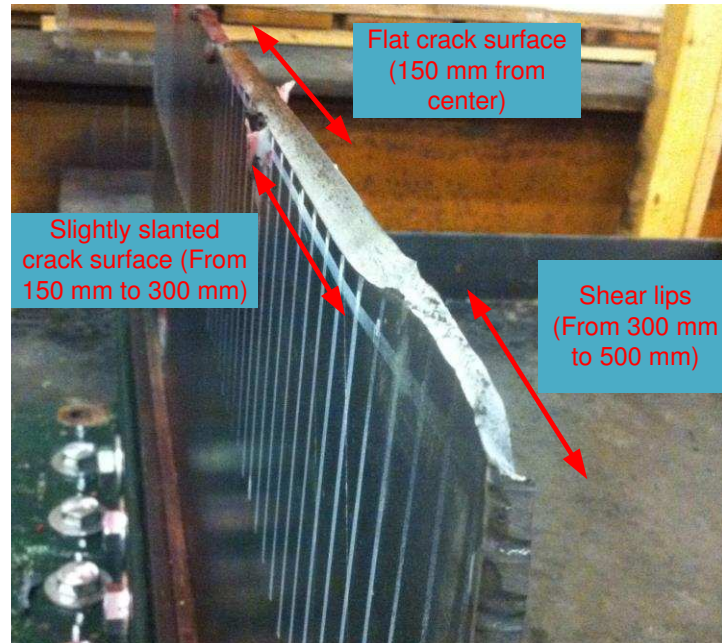


Figure 42. Crack surfaces for west half crack showing all the different fractures along the length of the crack after fracturing the specimen

4.2.1.3 Crack Growth Rate versus Change in Stress Intensity Factor

A log-log plot (shown in Figure 43) was developed for crack growth rate (da/dN) vs ΔK to obtain the values of the Paris law constants 'C' and 'm' from a straight trend line generated with 'C' being the y-intercept and 'm' being the slope of the line. As mentioned in chapter 2, there is a scatter in fatigue data and getting a single value for these constants is not possible. 'da' is change in crack length with 'dN' as change in number of cycles for corresponding change in crack length. ΔK is $K_{max} - K_{min}$ with K_{max} obtained from the maximum stress applied and K_{min} from minimum stress applied to the specimen.

The values for Paris law constants 'C' and 'm', were found to be 2×10^{-09} m/cycles $(MPa \text{ m}^{1/2})^m$ and 2.13, respectively, for half crack length on east side of the specimen. The values for the west side crack were found to be 2×10^{-11} m/cycles $(MPa \text{ m}^{1/2})^m$ and 2.77, respectively.

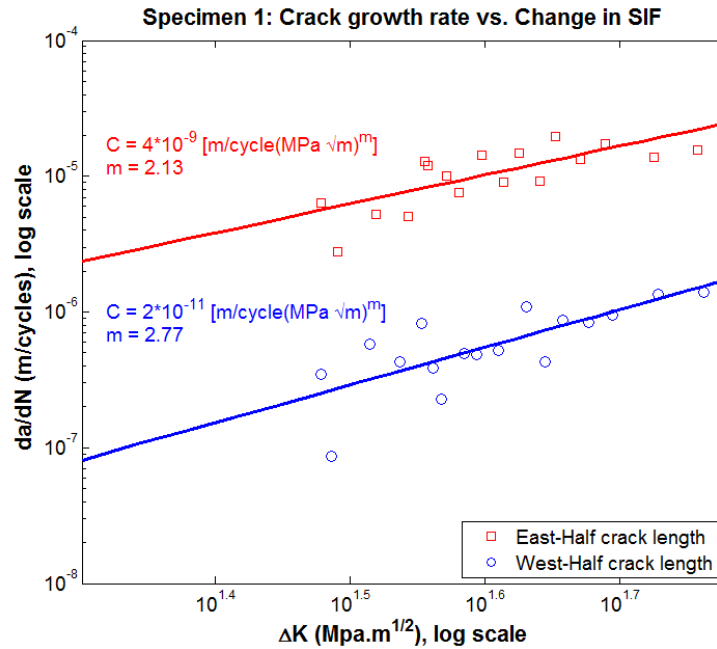


Figure 43. A log-log plot of crack growth rate (da/dN) vs change in stress intensity factor (ΔK) for half crack lengths on east and west side of the specimen 1

4.2.1.4 Change in Strain with Half Crack Length

Through the recorded strain gauge data, it was realized that the strain in both strain gauges on either side should increase exponentially with half crack length. The stress at the crack tip should tend to infinity. A plot was generated for strain in steel versus half crack as shown in Figure 44. As can be seen in Figure 36, strain in the steel increases gradually and tends to infinity as the crack approaches the strain gauges. It can also be seen that the strain values recorded by strain gauge 5 were less than that of strain gauge 6. As the respective half cracks approached the strain gauges, the measured strain in gauge 5 approached infinity (20-30 mm earlier) before strain gauge 6 did.

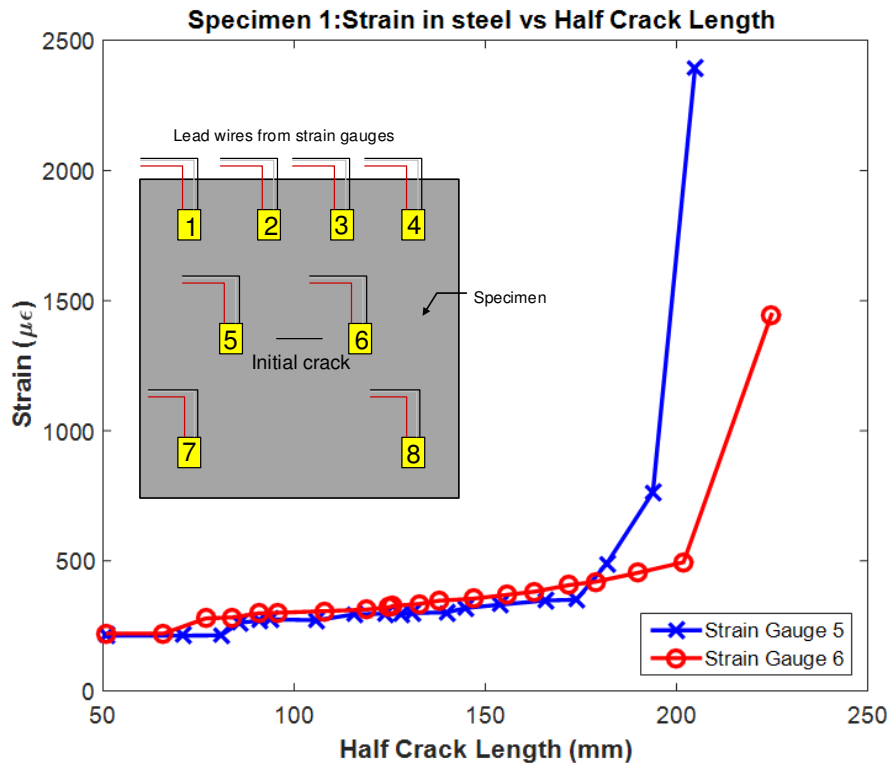


Figure 44. Strain in steel vs Half crack length for Specimen 1 with respective strain gauge locations

4.2.2 Test Results and Observations for Specimen 2

Specimen 2, retrofitted with CFRP, was tested under dry conditions with center crack of length 101.6mm and Tyfo-UC laminates CFRP attached at 110mm from the center of the crack using HUDCO Formula 3200 as explained in Chapter 3. *It is critical to emphasize that this adhesive has very low modulus and is not intended to use with CFRP. The reason for investigating its use is due to its ability to set underwater, which could provide an opportunity of easy repair.* Tack welds were introduced at the crack tips similar to specimen 1 to facilitate faster initial crack growth. The CFRPs were installed without any surface preparation. The motive for doing so was to check the effect of surface preparation on the performance of the CFRP. This is driven by the desire to

evaluate the possibility of practical field application where divers can simply install the CFRP under water on the cracked element without having to prepare any surfaces. The applied nominal stress range was 55 MPa (8 ksi) previously indicated. Eight strain gauges were installed on the specimen with strain gauge 4 and strain gauge 5 on two CFRP on the front face as discussed in chapter 3.

4.2.2.1 Crack Length versus Number of Cycles for Specimen 2

Crack length was measured similar to specimen 1. Cracking in the tack welds were noted at around 16,028 cycles with 52.8 mm half crack length. However, the cracks did not start to propagate until 63,294 cycles. The half cracks on each side propagated in stable manner until they reached the CFRPs (110 mm) with 254,251 cycles. At this point, the CFRP on front face on the east side showed complete debonding while all other CFRPs were intact (note: at this point the half crack length on the west side could not be measured as it was under the CFRP). Debonding of the CFRP installed on the front face on east side might have been a result of lack of surface preparation or a result of significant straining on the adhesive that is a result of the large crack opening in combination with the lack of surface preparation. At around 378,756 cycles and east half crack length of 150 mm all the remaining CFRP showed debonding. It should be noted that as the CFRP is debonded from one side below the crack line, it is assumed to be fully debonded.



Figure 45. Steel surface after CFRP debonding (front left) at 378,756 cycles for specimen 2

The east half crack length could be measured as the front right CFRP was already debonded. At 417,637 cycles and east half crack length at 172 mm, surface preparation was performed by grinding off any adhesive residue coating and roughing the surface and later cleaning it with acetone. The front left CFRP debonded even after surface preparation at 475,045 cycles with west half crack length of 184 mm and all other CFRPs were intact. This bedonding was believed to be because of the very large crack size that resulted in significant straining on the adhesive. This configuration was kept until 489,840 cycles and then the debonded front west CFRP was replaced, again. At 544,473 cycles, near fracture, all CFRP debonded. The total number of cycles to fracture

the specimen was 559,828. A plot of crack length versus number of cycles can be seen in Figure 46.

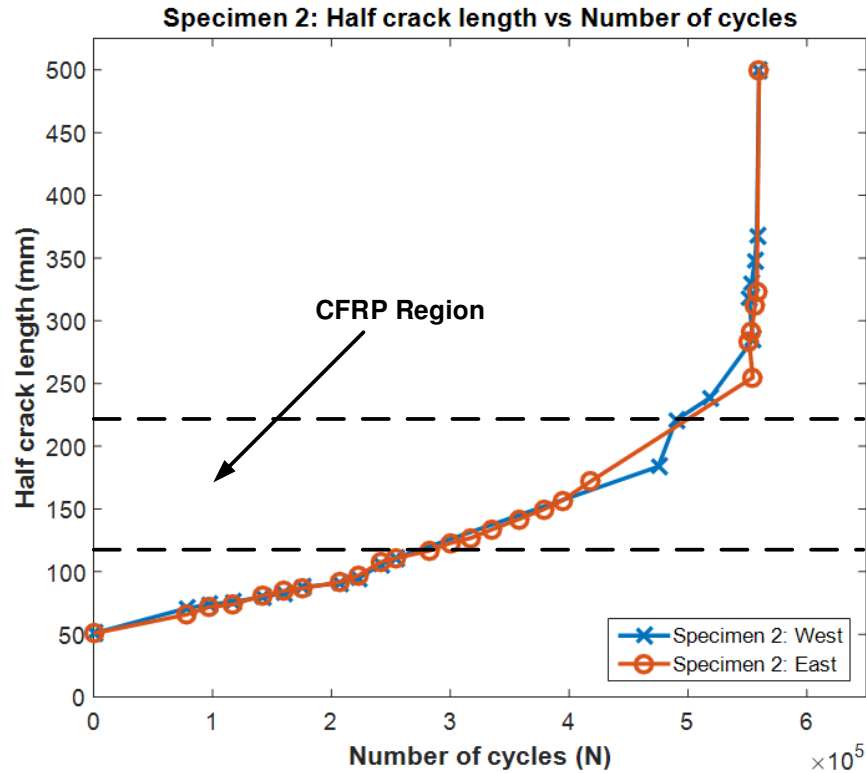


Figure 46. Half crack length vs Number of cycles for Specimen 2

Thorough study of crack surface shows smooth surface with chevron marks until 184 mm (7.2 in) indicating linear elastic behavior. From 184 mm to 374 mm (14.7 in), the crack surface was slanted and smooth with chevron marks indicating combined ductile-brittle crack extension. From 374 mm onwards until fracturing the specimen, crack surface showed shear lips indicating pure ductile fracture. Necking at the end also indicates pure ductile fracture of the specimen when both half cracks reached the end. The west half crack grew at higher rates after 220 mm than the east crack; in fact west half crack reached the end first, forcing the east half crack to become an edge crack for 4-5 cycles.

4.2.2.2 Change in Strain with Half Crack Length

Two different plots were generated for strain in steel versus half crack length and strain in CFRP versus half crack length as shown in Figure 47 and Figure 48, respectively. As can be seen in Figure 47, strain in steel increases gradually and tends to infinity as crack approaches strain gauges. It can be seen that the strain values recorded by strain gauge 3 were less than that of strain gauge 6. When half crack lengths read 180 mm, strain values for strain gauge 3 showed higher values than that of strain gauge 6 and as the respective half cracks approached the strain gauges, strain gauge 3 values approached infinity earlier (20-30 mm) as compared to strain gauge 6 values. It can be seen that gauge 6 measured almost constant strain when the east half crack was under CFRP.

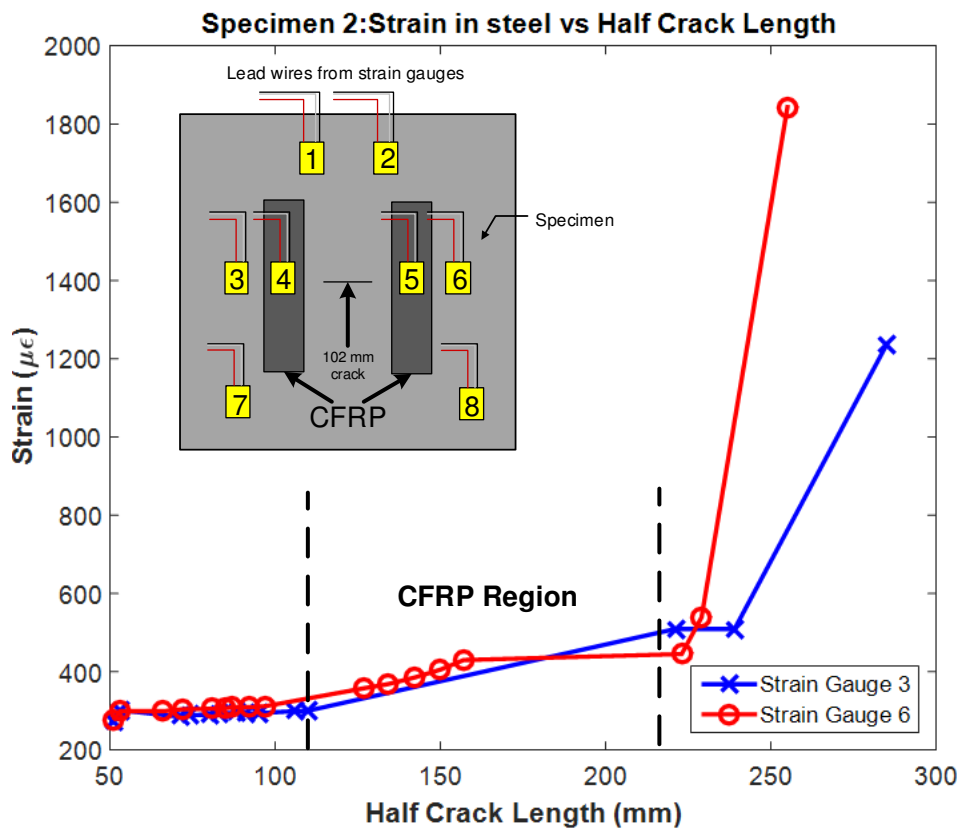


Figure 47. Strain in steel vs. Half crack length for specimen 2 with strain gauge locations

Strain gauge values for strain gauge 5 could not be recorded as it stopped reading the values as soon as the test was started. This could be attributed to either human error while installing this strain gauge or malfunctioning strain gauge. Strain gauge 4 values against west half crack length can be seen in Figure 48. As can be seen in Figure 48, the strain in gauge 4 increased gradually until point 2 (70 mm) shown by segment I implying the effectiveness of the CFRP in reducing crack growth, Segment II shows a jump in the strain implying higher strain in the CFRP as the crack propagated further (Figure 48). Segments III, IV and V show rapid increase in the strain. This could be attributed to the rapid debonding of CFRP. At point 6 (110 mm) CFRP totally debonded. Further data for strain gauge 4 could not be recorded as CFRP debonded multiple times. It can be noted that strain in steel (SG3) showed higher values than in CFRP but as the crack grew and CFRP was replaced, strain in steel increased gradually implying effectiveness of CFRP. . As previously emphasized, the adhesive used with Specimen 2 had very low modulus and was only investigated due to its ability to set underwater, which could provide an easy and viable retrofit option. Undoubtedly, the debonding of the CFRP as it interacted with the crack is due to the low modulus of the adhesive used with this specimen.

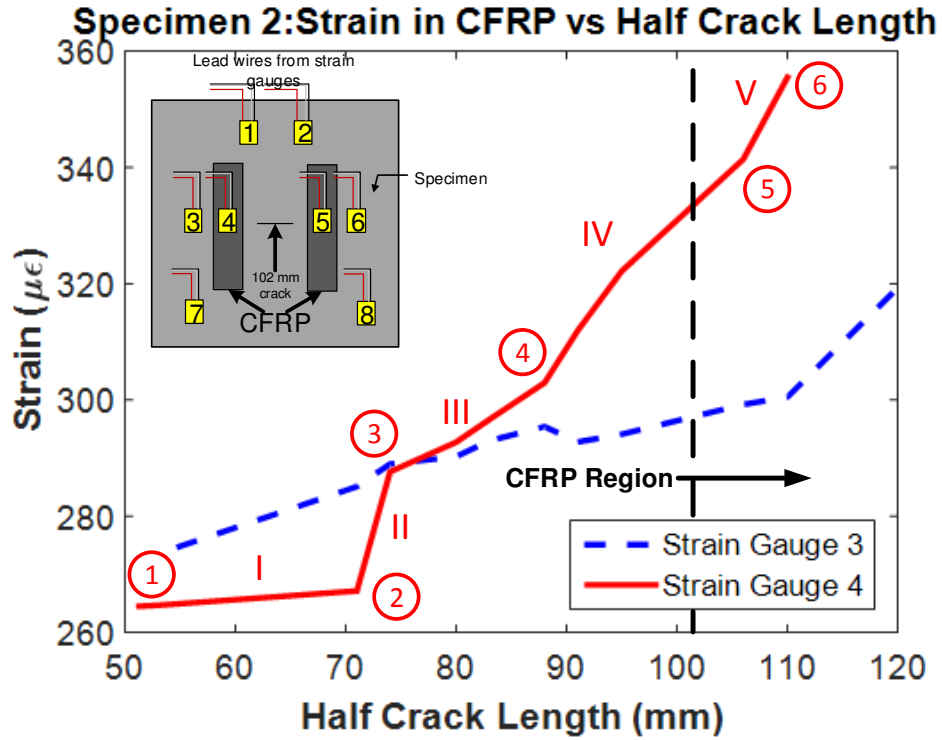


Figure 48. Strain in CFRP vs. Half Crack length for Specimen 2 with strain gauge locations

Table 5. Number of cycles for the points shown in Figure 48

	Point 1	Point 2	Point 3	Point 4	Point 5	Point 6
Cycles	63294	77951	97188	160174	241708	254251

4.2.3 Test Results and Observations for Specimen 3

Specimen 3 was tested under dry conditions with initial center crack of length 101.6 mm. CFRP Tyfo SCH-41 sheets were attached at 110mm from the center of the crack using Tyfo-S epoxy as explained in Chapter 3. This epoxy adhesive has a relatively high modulus value and is designed

to be used with CFRP. This is unlike the low modulus adhesive used with Specimen 2. Tack welds were introduced at the crack tips similar to specimen 1 and 2 to facilitate faster crack initiation. For this specimen, CFRP were installed with surface preparation. A stress range of 55 MPa (8 ksi) was applied to the specimen. Eight strain gauges were installed on the specimen with strain gauge 4 and strain gauge 5 on two CFRP on front face as discussed in Chapter 3.

4.2.3.1 Crack Length versus Number of Cycles for Specimen 3

Tack welds accelerated the crack initiation at first but after coming out of the residual stress field of these welds, crack propagated in a stable manner until reaching the CFRP. At 72,201 cycles, crack showed the propagation with half crack length on the west side 61 mm and 59 mm on the east side. After reaching CFRP, localized debonding of the CFRP where the crack is located was observed. At 517,028 cycles, strain gauge 5 was replaced as it showed no value. This might be attributed to the human mistake while attaching the strain gauge on the CFRP or the incompatibility of the strain gauges on surface of the CFRP. When the cycle number reached 572,487, the crack had propagated from underneath of the CFRP with half crack length of 226 mm on both sides. After this stable crack propagation was observed until it reached the critical crack length after which it showed unstable propagation. All four CFRP did not debond until 393 mm (west) and 392 mm (east) with 673,274 cycles. *This clearly highlights the importance of using proper adhesive for effective repair in comparison with Specimen 2.* The total number of cycles to fracture the specimen was 673,830. Plot of crack length versus number of cycles can be seen in Figure 49. Figure 42 and Figure 43 show typical crack growth in this specimen with CFRP still intact and fractured specimen, respectively.

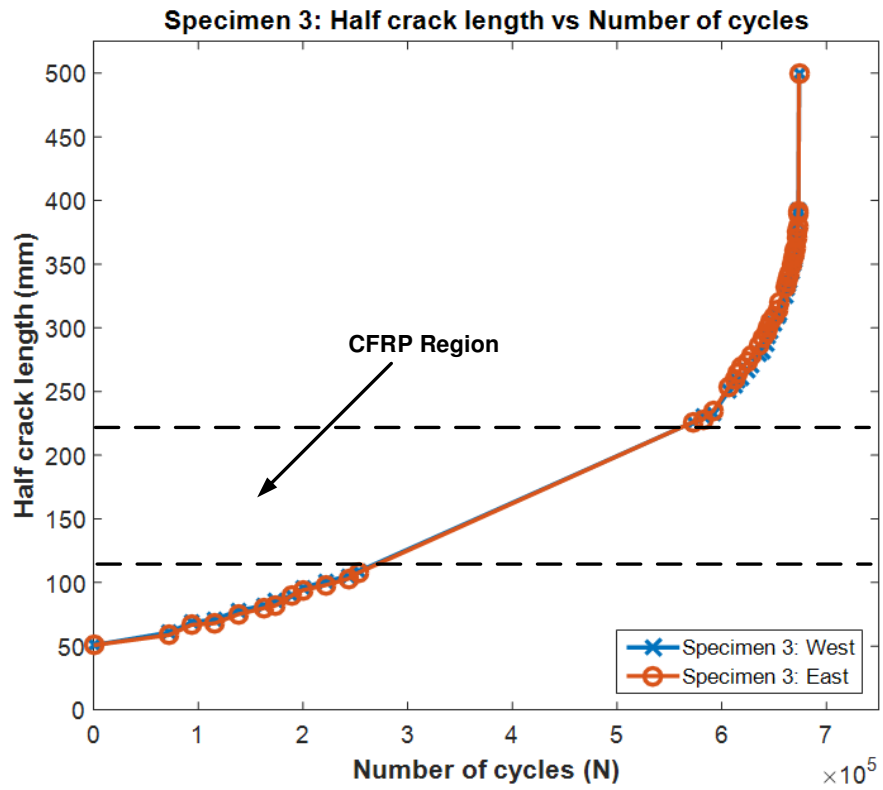


Figure 49. Half crack length vs Number of cycles for Specimen 3

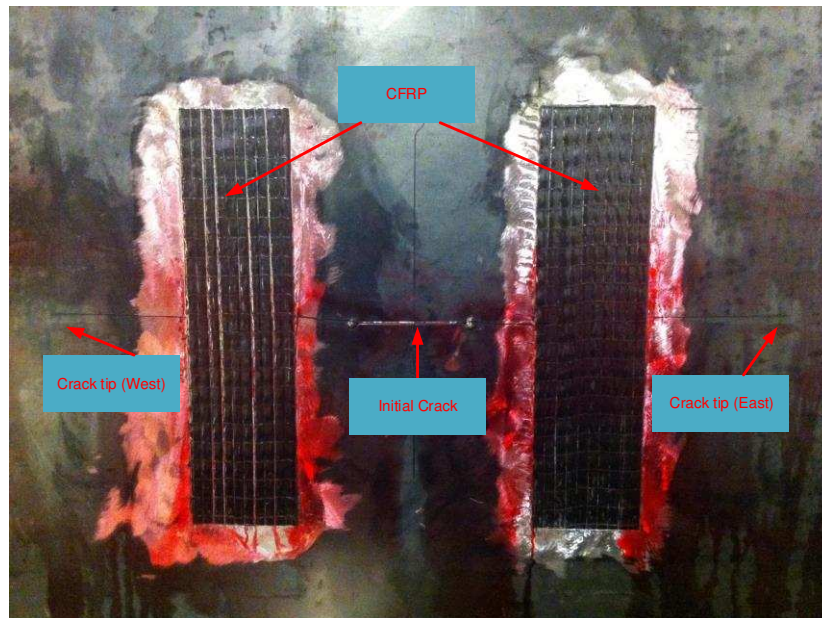


Figure 50. Crack propagation on each side of CFRP for Specimen 3



Figure 51. Fractured specimen 3

4.2.3.2 Change in Strain with Half Crack Length

Two different plots were generated for strain in steel versus half crack length and strain in CFRP versus half crack length as shown in Figure 52 and Figure 53, respectively. As can be seen in Figure 52, strain in steel increases gradually and tends to infinity as crack approaches strain gauges. It can be seen that the strain values recorded by strain gauge 3 were less than that of strain gauge 6. As the respective half cracks approached the strain gauges, strain gauge 3 values approached infinity at same crack length as strain gauge 6.

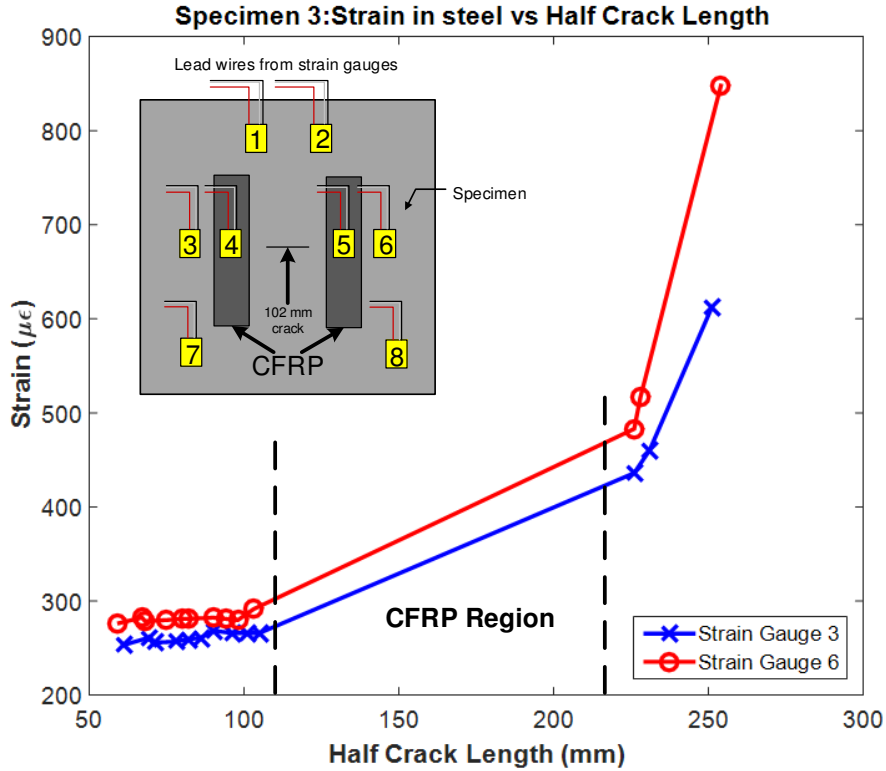


Figure 52. Strain in steel vs. Half crack length for Specimen 3 with strain gauge locations

As can be seen in Figure 53, strain values for both strain gauge 4 and strain gauge 5 increased gradually till the crack reached the CFRP as indicated by segment I from point 1 to point 2. (until 110 mm). Half crack lengths could not be measured as the cracks were under CFRP. As soon as the cracks propagated past CFRP (220 mm), the respective strain gauges showed very high strain values implying a rapid strain increase in the CFRP indicated by point 6. Maximum strain in west and east CFRP were $1313\mu\epsilon$ and $1575\mu\epsilon$. This is approximately 15.5% of the ultimate tensile strength of CFRP in the direction of fibers. Large increase in the CFRP when the crack had propagated from underneath the CFRP imply the effectiveness of the CFRP in transferring load and that no debonding had occurred.

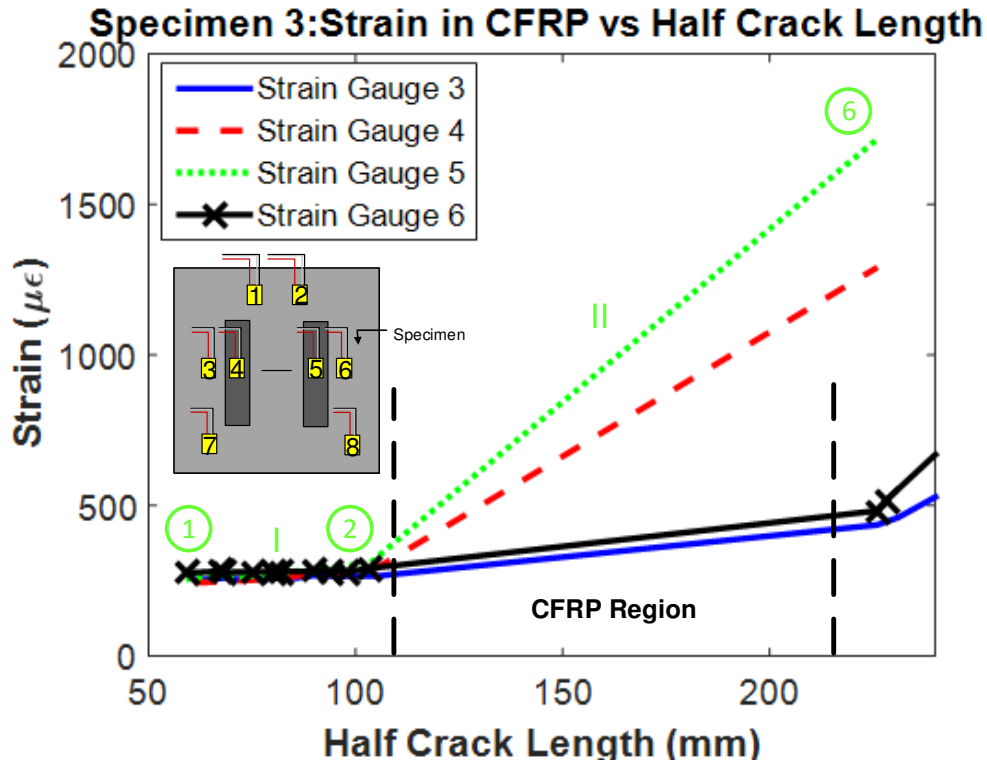


Figure 53. Strain in CFRP vs. Half crack length for Specimen 3 with strain gauge locations

Table 6. Number of cycles for the points shown in Figure 53

	Point 1	Point 2	Point 3	Point 4	Point 5	Point 6
Cycles	72201	243297	NA	NA	NA	572487

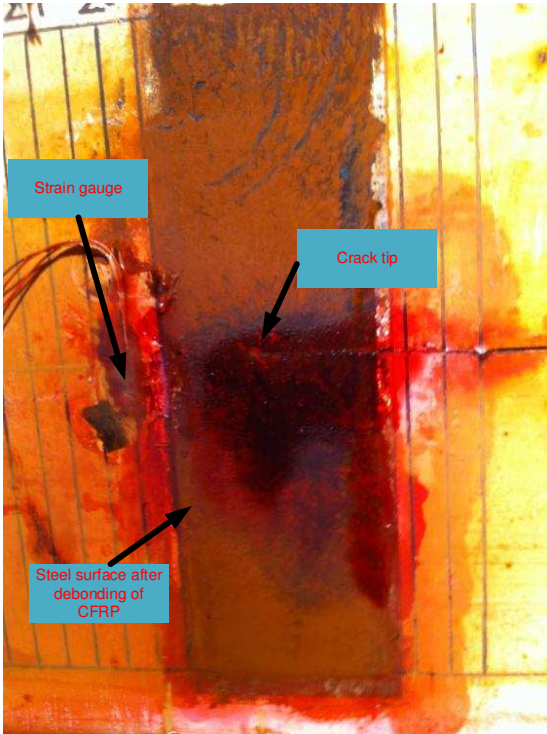
4.2.4 Test Results and Observations for Specimen 4

Specimen 4 was tested under wet conditions after specimen 3 with center crack of length 101.6 mm and Tyfo SCH-41 sheets CFRP attached at 110mm from the center of the crack using Tyfo-S epoxy as explained in Chapter 3. Tack welds were introduced at the crack tips, similar to the other specimens, to facilitate faster crack initiation. The CFRPs were installed with surface preparation.

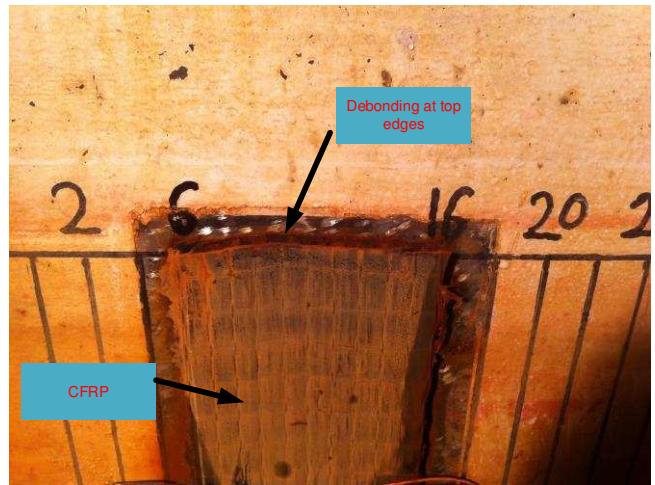
Stress range was 55 MPa (8 ksi) was applied to the specimen. In addition, 90 kg (200 lbs) of salt and same amount of sand with 0.45-0.55 mm particle size was introduced in the tank containing 2,306 liters of water.

4.2.4.1 Crack Length versus Number of Cycles for Specimen 4

For this specimen the east crack initiated at 60,141 cycles but the west crack showed no initiation. As the test progressed, the west half crack caught up with its east side counterpart. Both cracks propagated in a stable manner until 200,535 cycles when the west CFRP on the back face (east from front face) was totally debonded. The surface after CFRP debonding can be seen in Figure 54 (a). The reason for debonding can be attribute to the fact that this specimen face was subjected to the turbulence and the bombardment of the sand particles. When east crack was 152 mm at 246,568 cycles, the east CFRP on the back face started showing debonding at the top edges as can be seen in Figure 54 (b). Although the crack propagated in stable manner, the west CFRP on the back face was fully debonded at 292,948 cycles. The performance of the CFRP on the front face was very different than that installed on the back face. Specifically, debonding was observed at very large half crack length of 365 mm on the west side and 362 on east side for the west CFRP on the front face. When debonded, a loud breaking noise was heard, indicating that the CFRP reached full strength. Test was stopped at 432,579 cycles as there was a possibility of damaging acrylic walls while fracturing the specimen. A plot for crack length vs number of cycles for this specimen is shown in Figure 55. The reason for the much better performance of the CFRP on the front face than the CFRP on the back face can be attributed to the fact that the front face was isolated from the turbulence generated by the propeller and the effect of the sand particles through the partitions as discussed in chapter 3. A final picture showing back face of the specimen is shown in Figure 56.



(a)



(b)

Figure 54. Specimen 4 showing (a) Steel surface after CFRP debonding (b) Debonding of CFRP at top edges

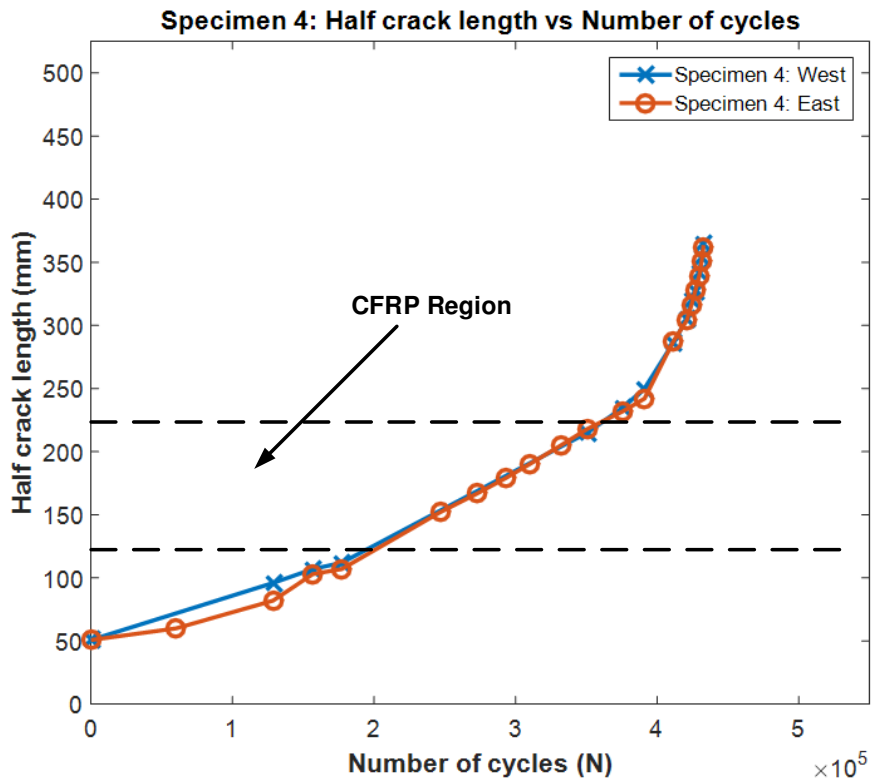


Figure 55. Crack length vs Number of cycles for Specimen 4

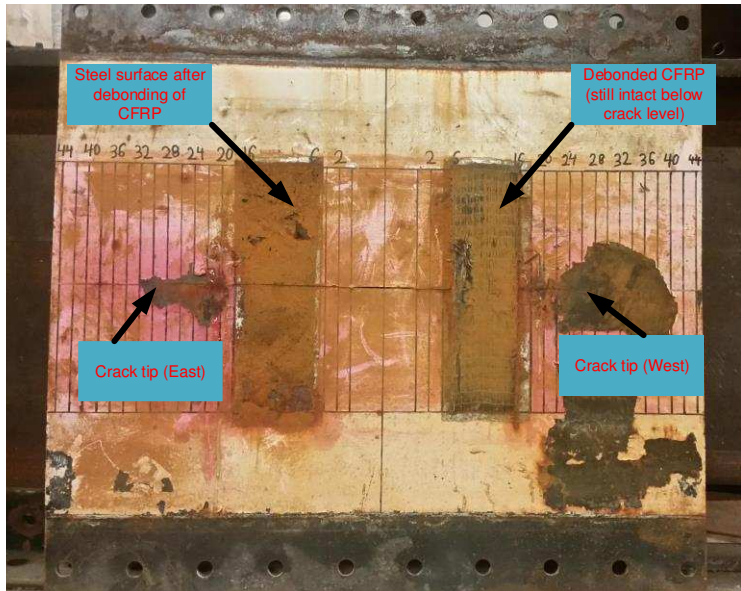


Figure 56. Back face of Specimen 4 after the test

4.2.4.2 Change in Strain with Half Crack Length

Two different plots were generated for strain in steel versus half crack length and strain in CFRP versus half crack length as shown in Figure 57 and Figure 58, respectively. As can be seen in Figure 57, strain in the steel increases gradually and tends to infinity as the crack approaches strain gauges. It can be seen that the strain values recorded by strain gauge 3 were equal to that of strain gauge 6. As the respective half cracks approached the strain gauges, strain gauge 3 values approached infinity at same crack length as strain gauge 6.

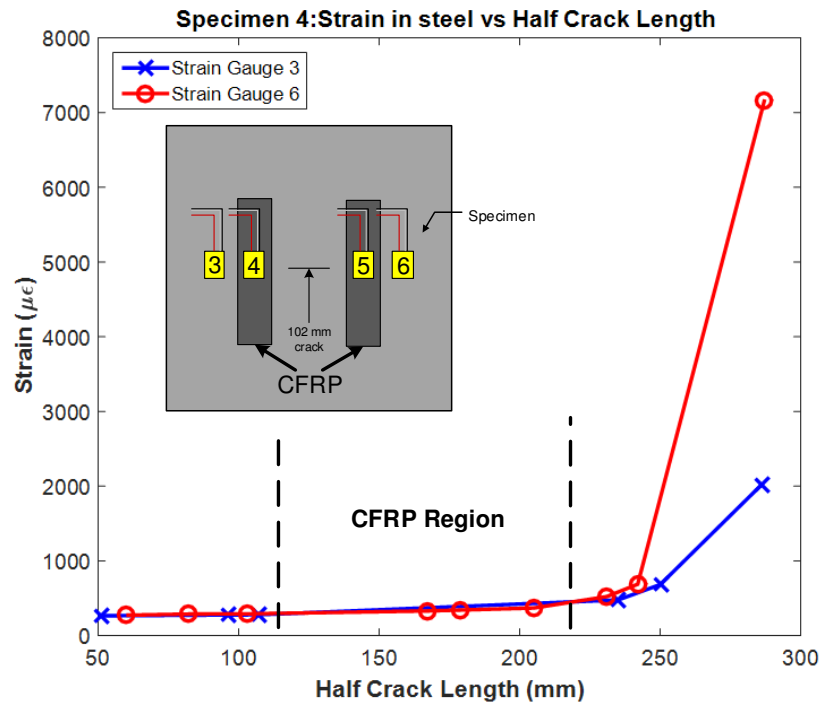


Figure 57. Strain in steel vs. Half crack length for specimen 4 with strain gauge locations

Strain gauge values for strain gauge 4 could not be recorded as it stopped reading the values as soon as the test was started. This could be attributed to either human error while installing this strain gauge or strain gauge being defective itself or the protective covering of this strain gauge

had openings which lead to interaction with water. As can be seen in Figure 58, strain in gauge 5 increased until the crack reached the CFRP as indicated by segment I. As the crack was under the CFRP, further increase in strain was observed until 175 mm as shown by segment II. This was followed by a clear jump (indicated by segment III) in the values implying higher strain in the CFRP. The strain kept increasing gradually as soon as the crack passed the CFRP as indicated by segments IV and V. The Maximum strain recorded by strain gauge 5 was 1348 $\mu\epsilon$ which implies approximately 13.25% of the maximum tensile strength was engaged in the direction of the fibers. Strain in steel was less than strain in CFRP as expected.

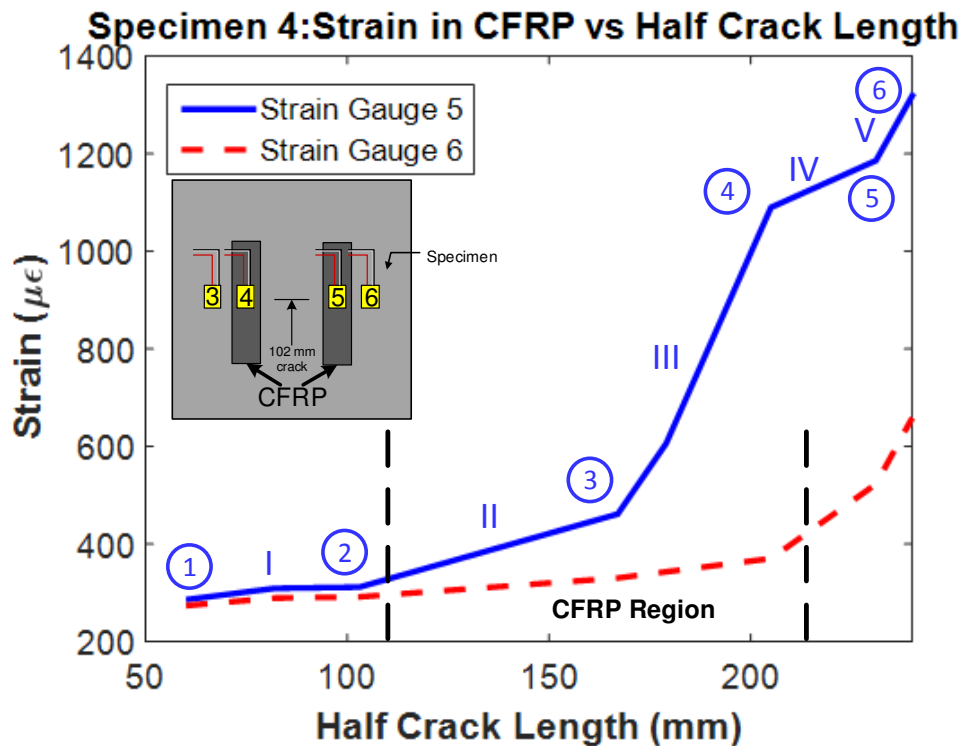


Figure 58. Strain in CFRP vs. Half crack length for specimen 4 with strain gauge locations

Table 7. Number of cycles for the points shown in Figure 58

	Point 1	Point 2	Point 3	Point 4	Point 5	Point 6
Cycles	60141	156744	273077	332003	375823	411255

4.3 Comparison of Results

This section includes the comparison of the results obtained for individual specimen as discussed in previous section. Mainly, half crack length versus number of cycles and half crack length versus strain values in both steel specimen and CFRP will be discussed.

4.3.1 Half Crack length vs Number of Cycles

It is important to compare the results for individual specimen to obtain an overall clearer perspective on the effectiveness of CFRP for underwater repair of steel panels. Figure 59 shows a plot comprising of half crack length versus number of cycles for all the four specimens. In addition, it took 439,140 cycles for specimen 1 to fracture. Specimen 2 with Tyfo UC laminates and Hudco Formula 3200 showed better results over specimen 1 having no CFRP. Although as noted before the Hudco Formula 3200 is a paste, with very low modulus, that is not intended for CFRP use. In this specimen, the CFRP had to replace three times due to the inadequacy of the adhesive. Overall the total number of cycles were recorded to be 559,828 cycles which is 1.3 times that of specimen 1. Specimen 3 took the maximum cycles to fracture with total cycles of 673,830, which is 1.5 times the specimen 1. This implies that the Tyfo SCH-41 sheets bonded to steel specimen near the crack tip using Tyfo-S adhesive has the advantage over Hudco Formula 3200. Specimen 4 included the effect of turbulence with effect of turbulence and bombardment of fluvial sediments on one side

and the effect of salt on both sides of the specimens. The total number of cycles to fracture was 432,579 cycles. This was approximately the same of that of specimen 1, which had no CFRP and was tested in-air. A numerical study for crack length versus number of cycles was conducted for unrepaired specimen subjected to corrosive environment. A plot was generated for this using Paris law constants $C = 2.4 \times 10^{-12.11} \text{ m/cycles (MPa m}^{1/2})^m$ and $m=3$ recommended by British Standards (2012) for corrosive environments. The results of unrepaired underwater specimens with Paris law parameters for a corrosive environment indicated that the underwater CFRP repaired specimen with the effect of turbulence and sand is approximately 3.5 better than its unrepaired counterpart shown by a dotted line in Figure 59. This clearly highlights the potential for this repair method to increase fatigue life of underwater repaired specimens.

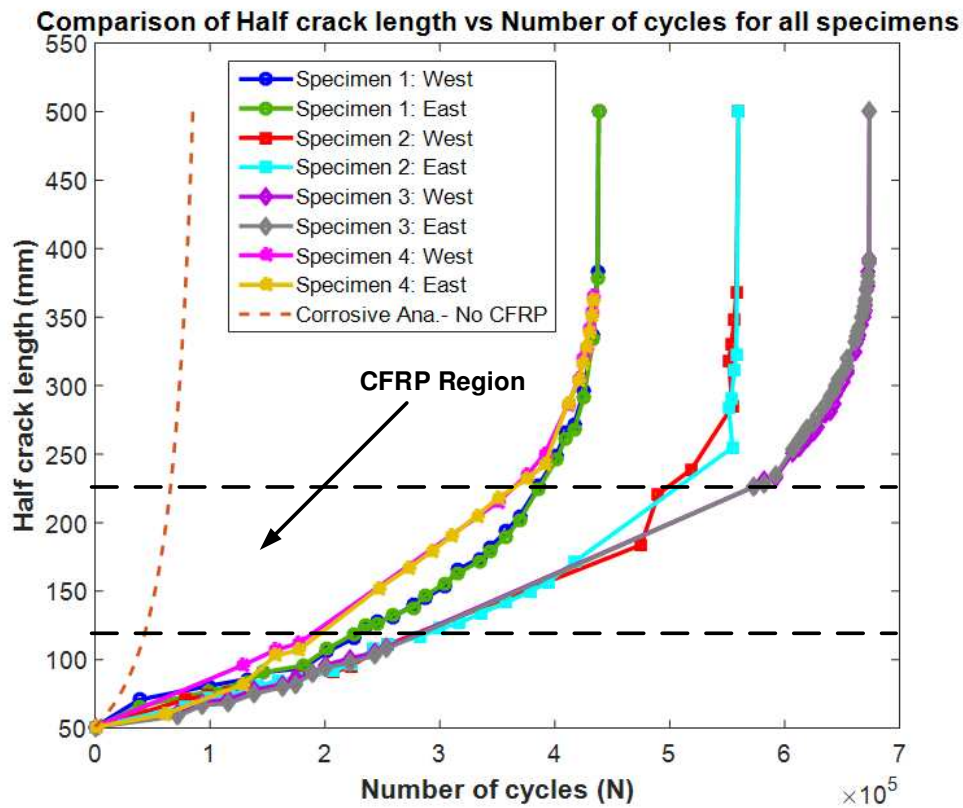


Figure 59. Comparison of Half crack length vs. Number of Cycles for all specimens

4.3.2 Strain in Steel vs. Half Crack length

To compare the strain developed in steel while testing each specimen, a plot was generated for the strain in steel versus half crack length which can be seen in Figure 60. Strain in the steel should show lesser values for specimens with CFRP as it reduces the strain at crack tips. Strain values for strain gauge 6 for specimen 4 were less than that of the other strain gauges for different specimens. The second lowest value was for strain gauge 3 of specimen 3. Highest strain values were obtained for strain gauge 6 of specimen 2 as a result of CFRP replacement. It can be noted that the strain values increased gradually for specimens with CFRP until the crack was under CFRP and later increased exponentially (cannot be seen in figure) as explained in previous sections.

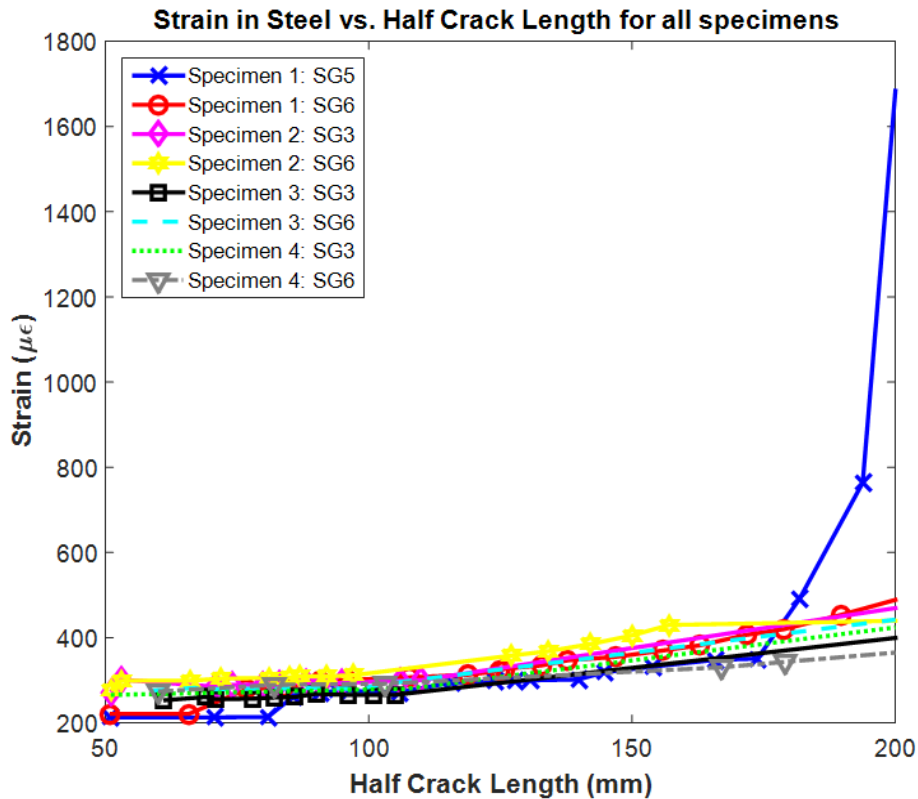


Figure 60. Comparison of Strain in Steel vs. Half Crack Length for all specimens

Chapter 5

Conclusions, Field Implications and Future Work

5.1 Conclusions

A new experimental setup was developed to evaluate the potential for using CFRPs for underwater fatigue repairs of steel panels. Conclusions were drawn from four physical experiments and a numerical analysis for an unrepaired corroded panel.

- A log-log plot of ' da/dN vs ΔK ' shows scatter in the data for specimen 1. Values of Paris Law constants ' C ' and ' m ' found in this study were very close to those found in the accepted studies (Barsom, et al., 1999, Dexter, et al., 2004).
- Surface preparation conducted before applying CFRP to specimen helps to improve the bonding of the adhesive to the steel. Tyfo UC-laminates showed debonding multiple times for specimen 2 even after surface preparation. Tyfo SCH-41 sheets showed no debonding until specimen 3 was fractured. These sheets displayed only localized debonding when crack was under this particular type of CFRP.
- Although debonding several times, UC laminates with Hudco Formula 3200 epoxy increased the fatigue life of the specimen by 1.3 times. This adhesive is not meant to be used with CFRP application but was evaluated due to the potential advantage it can provide for field application as it can set underwater (i.e. chamber dewatering is not required).
- SCH-41 sheets with Tyfo S epoxy increased the fatigue life of the specimen by 1.5 times. With its higher modulus value, this proves to be a better selection over its Hudco Formula 3200 counterpart.

- Approximately 15% of the ultimate tensile strength along the direction of the fibers was engaged for the combination of SCH-41 sheets along with Tyfo-S epoxy for specimen 3 which was tested under dry condition and approximately 13% of the ultimate tensile strength along the direction of the fibers was recorded for underwater retrofitted plate (specimen 4) with the same combination.
- Debonding of SCH-41 on one the back face for Specimen 4 can be attributed to the combined effect of salt and bombarding sand particles. Debonding was not observed on the front face until the crack was very long and the CFRP achieved full strength. The front face was not subjected to turbulence or the impact of sand.
- It can be seen that the total number of cycles taken to fracture control specimen and that of underwater CFRP-retrofitted specimen (Specimen 4) are very close which implies that salt corrodes the crack tip accelerating the crack propagation rate. When comparing the results of the underwater repaired specimen with that of a numerically obtained solution of underwater but unrepaired, an improvement of fatigue life of approximately 3.5 time is observed. This clearly demonstrates the potential of this underwater retrofit method.

5.2 Field Implications

This study was conducted for experimentally assessing the potential for underwater CFRP-retrofitting of large steel panels. It is important to imply the findings of this study in the field. The following observations should be considered for field implementations:

- Tyfo UC-laminates show increase in the fatigue life when used with Hudco Formula 3200 epoxy paste. This epoxy can bond to underwater or wet surfaces and Tyfo UC-laminates do not absorb any water when not covered with epoxy, a combination of both can be used for temporary retrofitting without dewatering the Miter gates

- Hudco Formula 3200 epoxy can be applied to UC-laminates outside the water and then can be taken underwater to apply to steel at required places
- Tyfo SCH-41 sheets resulted in the highest fatigue life increase when used with Tyfo-S epoxy. These sheets absorb water and cannot be applied underwater. Furthermore, Tyfo-S is not paste type adhesive which makes it harder to apply underwater. Tyfo-S does not bond to underwater or wet surfaces. However, it can set in dry conditions and then be subjected to water without any foreseen issues.
- Tyfo-S has significantly higher modulus than Hudco Formula 3200 and should be utilized for permanent repairs.
- For long term retrofitting, combination of Tyfo SCH-41 sheets with Tyfo-S epoxy can be used after detwearing the chamber to ensure application in dry conditions and hardening of the CFRP/adhesive components prior to refilling the chamber with water.
- Tyfo SCH-41 sheets are flexible and can be applied at sharp corners and to complicated geometries

5.3 Future Work

The current study emphasizes the need for future work regarding fatigue crack growth in CFRP retrofitted underwater steel panels. In addition to the remaining three specimens to be tests, some of the important research needs include:

- Deriving equations for effective bond length of CFRP for underwater retrofitting.
- Evaluating the effect of water turbulence on crack propagation rate.
- Assessing the effect of steel corrosion on bonding of CFRP.

- Studying the use of adhesive that can be applied without dewatering and is more reliable than the Hudco Formula 3200.
- Evaluating different arrangements of CFRP such as increased size of CFRP and covering the initial crack with the CFRP.
- Investigate the effect of CFRP on crack propagation in mode II, mode III and multimode loading.

Bibliography

AASHTO AASHTO LRFD Bridge Design Specifications [Report]. - Washington, DC : American Association of State Highway and Transportation Officials, 2010.

AISC Specification for Structural Steel Buildings, Edition 14 [Report]. - [s.l.] : American Institute of Steel Construction Manual, 2010.

Alemdar F. [et al.] Use of CFRP Overlays to Strengthen Welded Connections under Fatigue Loading [Journal] // Journal of Bridge Engineering, Vol. 17, No. 3, May 1, 2012. ©ASCE, ISSN 1084-0702/2012/3-420–431/. - 2011. - p. 12.

Anderson T., L. Fracture mechanics : Fundamentals and Applications [Book]. - [s.l.] : Boca Raton : CRC Press, 1991.

Barsom J M and Rolfe S T Fracture and Fatigue Control in Structures: Applications of Fracture Mechanics [Book]. - Woburn : Butterworth-Heinemann Publications, 1999.

Barsom J M Fatigue crack growth under variable amplitude loading in various bridge steels. In Fatigue Crack Growth under Spectrum Loads. ASTM STP 595 [Journal]. - Philadelphia : American Society for Testing and Materials, 1976. - pp. 217-235.

Beden S M, Abdullah S and Ariffin A K Review of Fatigue Crack Propagation Models for Metallic Components [Journal]. - [s.l.] : European Journal of Scientific Research, 2009. - 3 : Vol. 28. - pp. 364-397.

Bocciarelli M [et al.] Prediction of debonding strength of tensile steel/CFRP joints using fracture mechanics and stress based criteria [Journal]. - Elsevier : Engineering Fracture Mechanics, 2008. - 2009 : Vol. 76. - pp. 299-313.

British Standards. BS 7910: Guide on Methods for Assessing the Acceptability of Flaws in Metallic Structures [Report]. - 2012.

Chang J B, M Szamosi and Liu L W Random Spectrum Fatigue Crack Life Predictions with or without Considering Load Interactions. ASTM STP 748 [Journal]. - [s.l.] : American Society for testing and Materials, 1981. - pp. 115-132.

Collipriest E J An Experimentalist's View of the Surface Flaw Problem. Physical Problems and Computational Solutions [Journal]. - New York : American Society of Mechanical Engineers, 1972. - - : Vols. - - pp. 43-62.

Dexter R J and Mahmoud H N Predicting Stable Fatigue Crack Propagation in Stiffened Panels [Report]. - [s.l.] : National Technical Information Service, 2004.

Dexter R J and Ocel J M Manual for Repair and Retrofit of Fatigue Cracks in Steel Bridges [Report]. - McLean, VA : Federal Highway Administration, 2005.

Forman R G Study of fatigue crack initiation from flaws using fracture mechanics theory [Journal]. - [s.l.] : Engineering Fracture Mechanics, 1972. - 2 : Vol. 4.

François D, Pineau A and Zaoui A Mechanical Behaviour of Materials: Vol 2- Fracture Mechanics and Damage [Book]. - [s.l.] : Dordrecht; Springer Science + Business Media, 2013. - 2nd : Vol. II.

Frost N E, Pook L P and Denton K A Fracture Mechanics Analysis of Fatigue Crack Growth Data for Various Materials [Journal]. - [s.l.] : Engineering Fracture Mechanics, 1971. - 2 : Vol. 3.

Griffith A A The phenomena of rupture and flow in solids [Journal]. - [s.l.] : Philosophical transactions of the royal society of london, 1921. - Vols. Series A, containing papers of a mathematical or physical character. - pp. 163-198.

HQUSACE Headquarters, US Army Corps of Engineers Advanced Reliability analysis of fatigue cracking in horizontally framed miter gates [Report]. - Washington, DC : U.S. Army Corps of Engineers, 2010.

Hudson C M A Root-Mean-Square Approach for Predicting Fatigue Crack Growth under Random Loading, Methods and Models for Predicting Fatigue Crack Growth under Random Loading [Journal]. - [s.l.] : ASTM STP 748, American Society for Testing and Materials, 1981. - pp. 41-52.

Irwin G R Fracture: Encyclopedia of Physics (Handbuch der Physik) [Book] / ed. Flugge S. - [s.l.] : Springer-Verlag, 1958. - Vol. VI : pp. 551-590.

Johnson W S Multi-Parameter Yield Zone Model for Predicting Spectrum Crack Growth. Methods and Models for Predicting Fatigue Crack Growth under Random loading [Journal]. - [s.l.] : American Society for Testing and Materials, 1981.

Johnson W S Multi-Parameter Yield Zone Model for Predicting Spectrum Crack Growth. Methods and Models for Predicting Fatigue Crack Growth under Random loading [Journal]. - [s.l.] : ASTM STP 748, American Society for Testing and, 1981. - pp. 85-102.

Jordan Paul R. Fluvial Sediment of the Mississippi River at St. Louis, Missouri [Report]. - Washington : United States Government Printing Office, 1965.

Julien Pierre Y. and Vensel Chad W. Review of Sedimentation Issues on the Mississippi River [Report]. - Fort Collins, CO : UNESCO: ISI, 2005.

Mahmoud H N and Riveros G A Fatigue Repair of Steel Hydraulic Structures (SHS) using Carbon Fiber Reinforced Polymers (CFRP): Feasibility Study [Report]. - Washington, DC : U. S. Army Corps of Engineers, 2013.

Mahmoud H N, Como A and Riveros G A Fatigue Assessment of Underwater CFRP-Repaired Steel Panels using Finite Element Analysis [Report]. - Washington, DC : U. S. Army Corps of Engineers, 2014.

Mertz D Steel Bridge Design Handbook: Design for Fatigue [Report]. - [s.l.] : U.S. Department of Transportation, 2012.

NASA Propeller Thrust [Online]. - <https://www.grc.nasa.gov/www/k-12/airplane/propth.html>.

Newman J R A crack closure model for predicting fatigue crack growth under aircraft spectrum loading [Journal]. - Philadelphia : ASTM STP 748 American Society for Testing and Materials, 1981. - pp. 53-84.

Paris P and Erdogan F A Critical Analysis of crack Propagation Laws [Journal] // Trans. ASME, Ser. D. Journal of Basic Engineering. - 1963.

Pugno N M and Ruoff R S Quantized fracture mechanics [Journal]. - [s.l.] : Philosophical Magazine, 2004. - 27 : Vol. 84.

Riveros Guillermo A. User's Guide: Computer aided inspection forms for hydraulic steel structures(CAIF-HSS), windows version [Report]. - Vicksburg, MS : U.S. Army Corps. of Engineers, 1997.

Schnerch D [et al.] Bond Behavior of CFRP Strengthened Steel Structures [Journal] // Advances in Structural Engineering. - 2006. - 6 : Vol. 9. - pp. 805-817.

Shaat A [et al.] Retrofit of Steel Structures Using Fiber Reinforced Polymers (FRP): State-of-the-Art [Report]. - 2003.

Shield C, Hajjar J and Nozaka K Repair of Fatigued Steel Bridge Girders with Carbon Fiber Strips [Report]. - Springfield, Virginia : National Technical Information Services, 2003.

Tavakkolizadeh M and Saadatmanesh H Fatigue Strength of Steel Girders Strengthened with Carbon Fiber Reinforced polymer Patch [Journal] // Journal of Structural Engineering, Vol. 129, No. 2, February 1, 2003. - 2003. - p. 11.

Tavakkolizadeh M and Saadatmanesh H Galvanic Corrosion of Carbon and Steel in Aggressive Environments [Journal]. - [s.l.] : Journal of Composites for Construction, 2001. - 3 : Vol. 5. - pp. 200-210.

Teng T [et al.] Debonding Failures in CFRP-Strengthened Steel Structures [Conference] // APFIS. - Japan : [s.n.], 2012. - p. 8.

Varma D Fatigue Crack Growth [Journal]. - [s.l.] : New Age International (P) Ltd, 1990.

Walker E K The effect of stress ratio during crack propagation and fatigue for 2024-T3 and 7076-T6 aluminum. In Effect of environment and complex load history on fatigue life, ASTM STP 462 [Journal]. - Philadelphia : American Society for Testing and Materials, 1970. - pp. 1-14.

Wheeler O E Spectrum Loading and Crack Growth [Journal]. - [s.l.] : Journal of Basic Engineering, 1972.

Willenborg J, Engle R M and Wood H A A crack growth retardation model using an effective stress concept [Report]. - Dayton : Air Force Flight Dynamic Laboratory, 1971.

Wu C, Zhao X and Duan W Fatigue of Center Cracked Steel Plates with UHM CFRP Plate Strengthening [Conference] // APFIS. - Japan : [s.n.], 2012. - p. 6.

Wu ZM [et al.] Application of improved hybrid bonded FRP technique to FRP debonding prevention [Journal]. - [s.l.] : Construction and Building Materials, 2011. - Vol. 25.

Yu Q Q, Zhao X L and Chen T Crack propagation prediction of CFRP retrofitted steel plates with different degrees of damage usin BEM [Journal]. - Elsevier : Thin-Walled Structures, 2014. - 2014 : Vol. 82. - pp. 145-158.

Appendix A

Approximate Calculations for Concentration of Fluvial Sediments

Background

Using Bernoulli's Equation

$$P_{\text{total}} = \text{static pressure} + \text{dynamic pressure}$$

Free stream

$$P_{t0} = P_0 + \frac{1}{2} * d * V_0^2$$

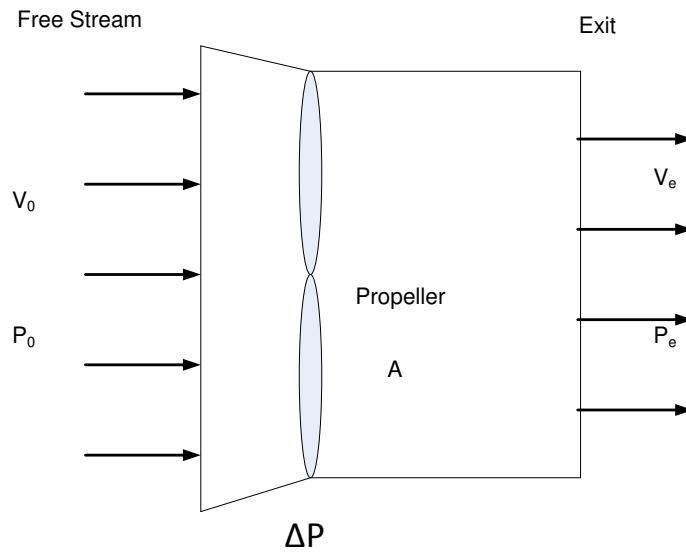
Exit stream

$$P_{te} = P_0 + \frac{1}{2} * d * V_e^2$$

$$\Delta P = \frac{1}{2} * d * [V_e^2 - V_0^2]$$

Putting back in equation of thrust

$$F = \frac{1}{2} * d * A * [V_e^2 - V_0^2] \quad (\mathbf{A1})$$



Using Momentum Theory

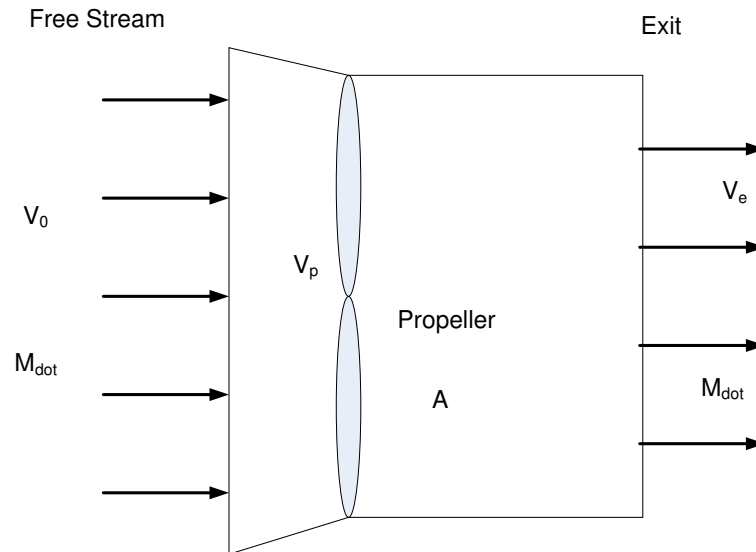
Thrust $[F] = \text{mass flow rate} * \text{change in velocity}$

$$= \dot{m} * V_e - \dot{m} * V_0$$

Through the area of the propeller A , mass flow rate is

$$\dot{m} = \rho * V_p * A$$

$$F = \rho * V_p * A * [V_e - V_0] \quad \text{(A2)}$$



Comparing equation A1 and A2

$$V_p = \frac{1}{2} * [V_e + V_0] \quad (\mathbf{A3})$$

Known Parameters

V_0 = Velocity of tug boat

V_p = Velocity at the propeller = can be found from the angular velocity

A = Area of the propeller

From equation A3, we can get exit velocity.

Calculations for this study

Propeller Diameter = 12 in = 0.3 m

Propeller Radius (r) = 6 in = 0.15 m

Area of propeller (A) = 0.1 m²

Revolutions per minute (RPM) = 500

Density of water (d) = 1000 kg/m³

Angular velocity (ω) = RPM \times $2\pi/60$

$$= 500 \times \frac{2\pi}{60} = 52.35 \text{ rad/sec}$$

Linear velocity at the tip of the propeller blade (V_P) = $r \times \omega = 0.15 \times 52.35 = 7.85 \text{ m/s}$

In this case $V_0 = 0 \text{ m/s}$

From equation 3,

$$V_P = \frac{1}{2} [V_e + V_0]$$

Exit velocity (V_e) = $2V_P - V_0 = 2 \times 7.85 - 0 = 15.7 \text{ m/s}$

Velocity (V) of Mississippi River = 1.2 m/s (Jordan, 1965)

$$\begin{aligned}\text{Mass flow rate } K \text{ [kg/s]} &= \text{Conc.}_{\text{sed}} \text{ [kg/m}^3\text{]} * V \text{ [m/s]} * A \text{ [m}^2\text{]} \\ &= (2200/10^{-3}) \text{ [kg/m}^3\text{]} * 1.2 \text{ [m/s]} * 1 \text{ [m}^2\text{]} && \text{(Julien, et al., 2005)} \\ &= 2.64 \text{ [kg/s]} && \text{(A4)}\end{aligned}$$

After 15 years = $15 * 365 * 24 * 60 * 60$ seconds

$$\begin{aligned}\text{Total mass flow after 15 years } K_{15} &= 2.64 * 15 * 365 * 24 * 60 * 60 \\ &= 1.24 * 10^9 \text{ kg}\end{aligned}$$

To cramp this mass in 20 days

$$1.24 * 10^9 \text{ kg} = m * 20 * 24 * 60 * 60$$

$$m = 717.5 \text{ kg/s}$$

Using equation 4 and volume of water = 2.3 m^3

$$717.5 = (C_{s15}/2.3) * V * A$$

Here V is the exit velocity of the propeller = 15.7 m/s

$$C_{s15} = 105 \text{ kg}$$

Appendix B

Detailed Drawings of Setup

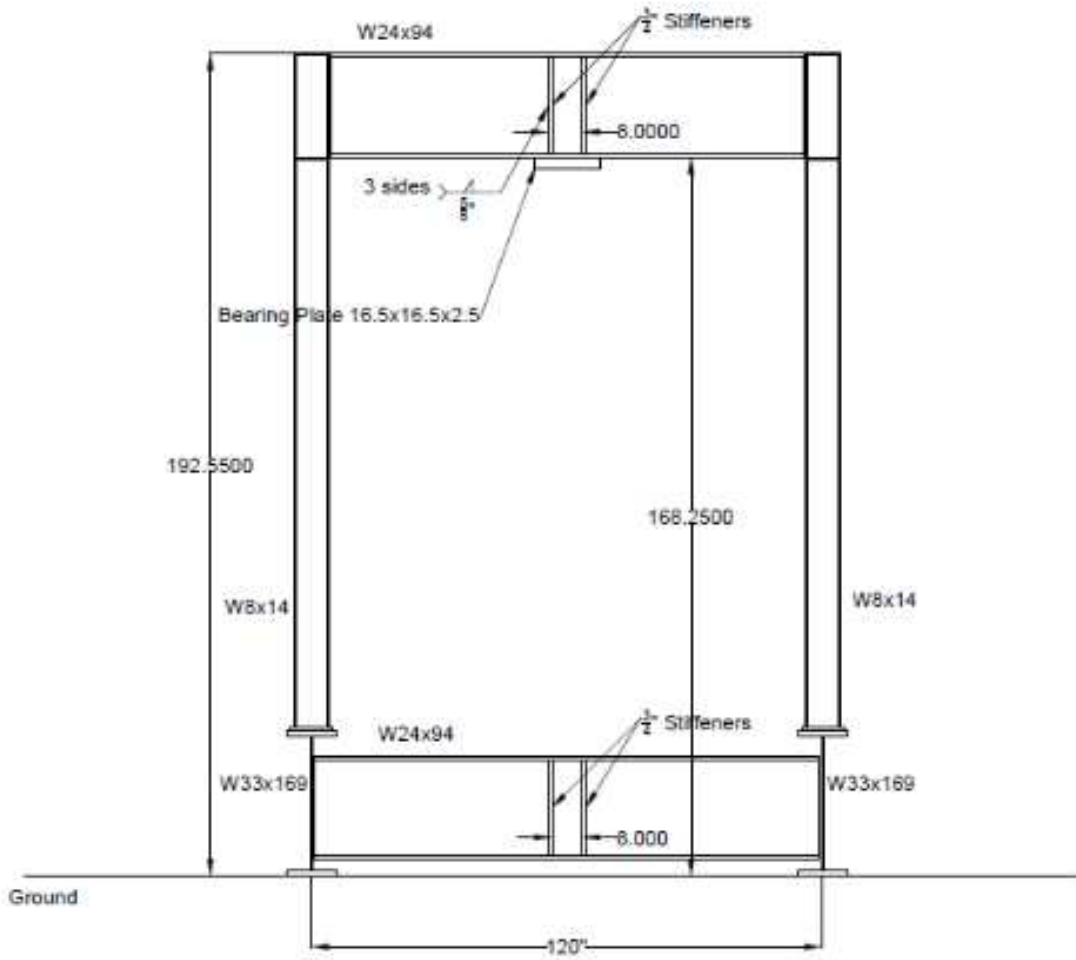


Figure 61. Front view of the test setup frame

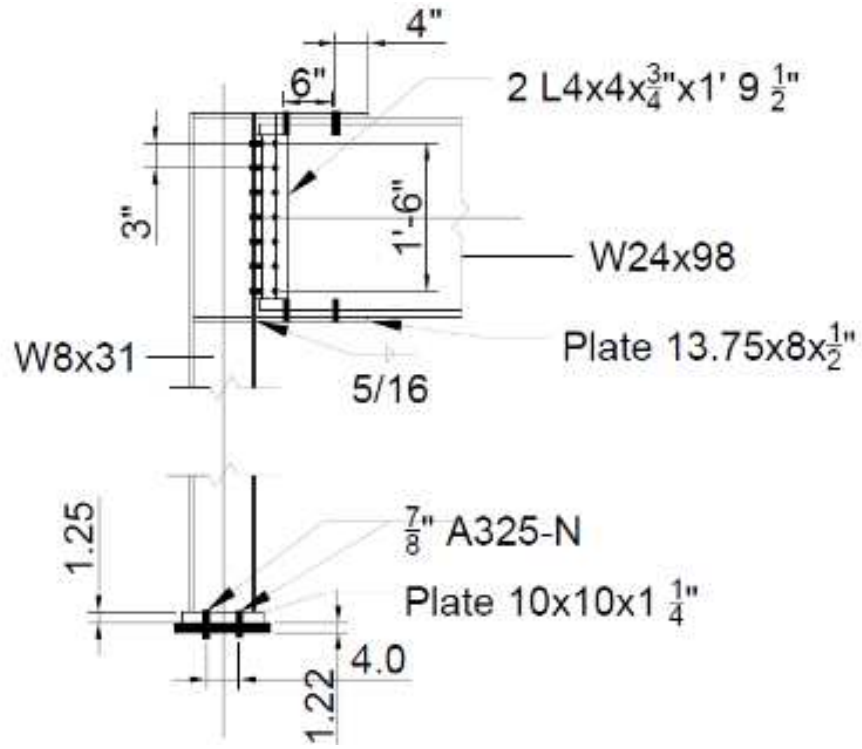


Figure 62. Beam to column shear connection and column base plate connection

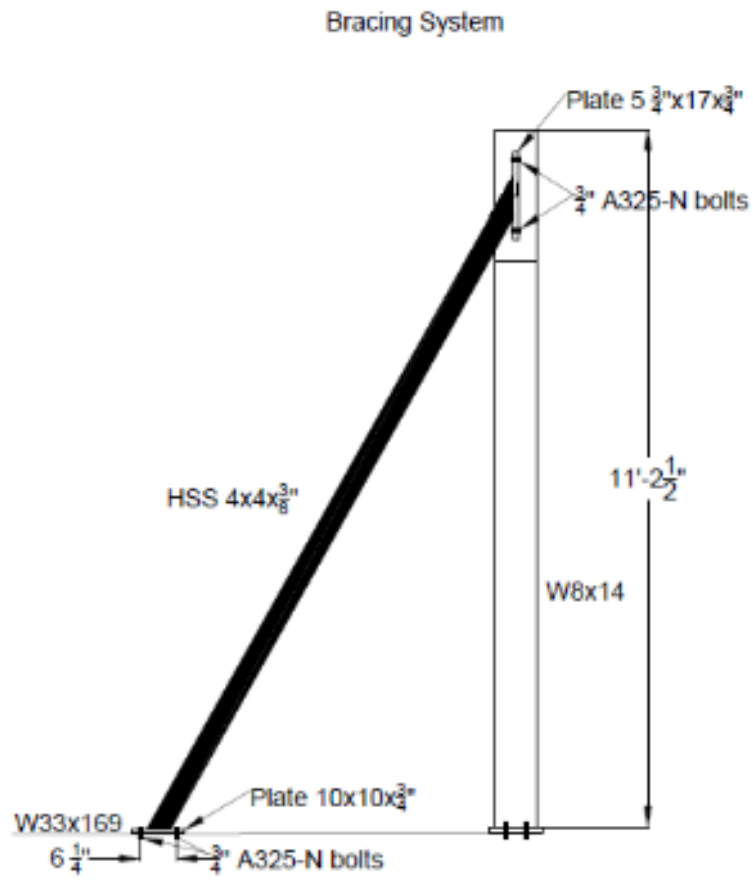


Figure 63. HSS bracing for the frame

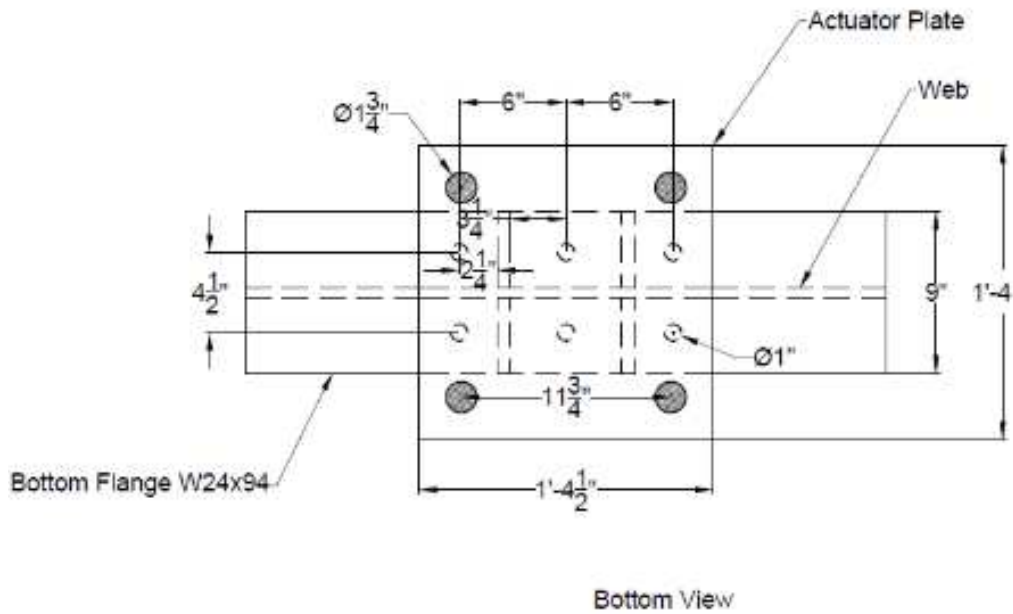


Figure 64. Actuator plate connections to bottom flange of top W24x94 beam

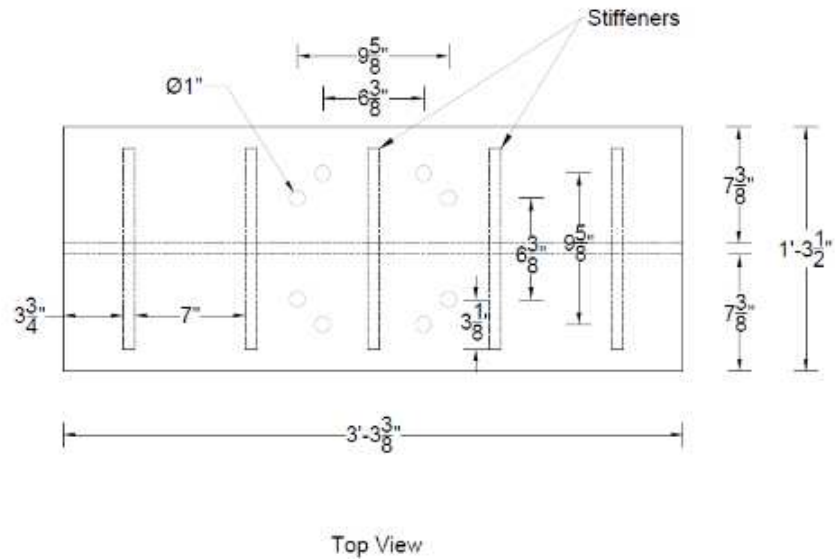


Figure 65. Spreader beam top view with holes to connect actuator swivel

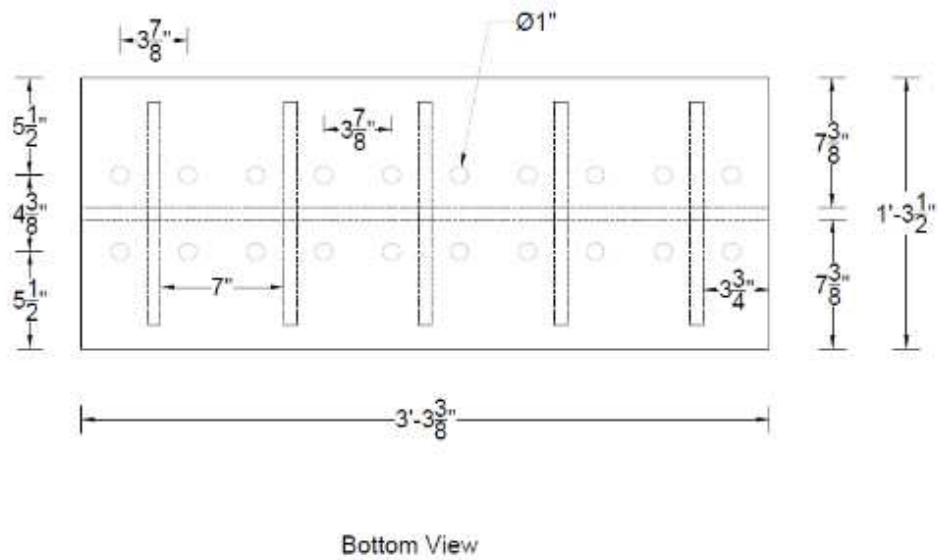


Figure 66. Spreader beam bottom view with holes to connect angles connecting specimen

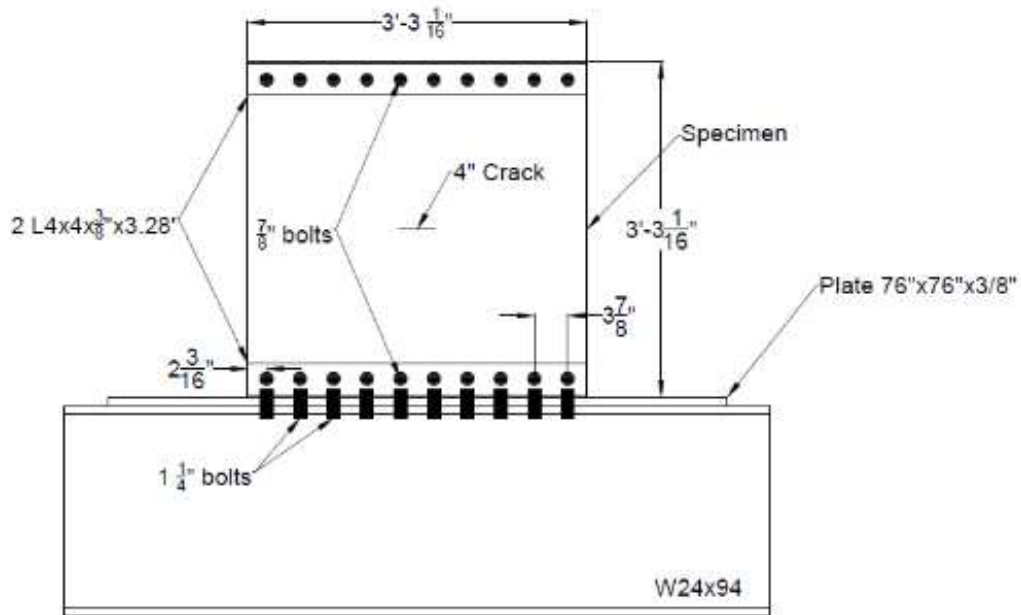


Figure 67. Bottom W24x94 beam and specimen connection

W24x94 and W33x169 Connection

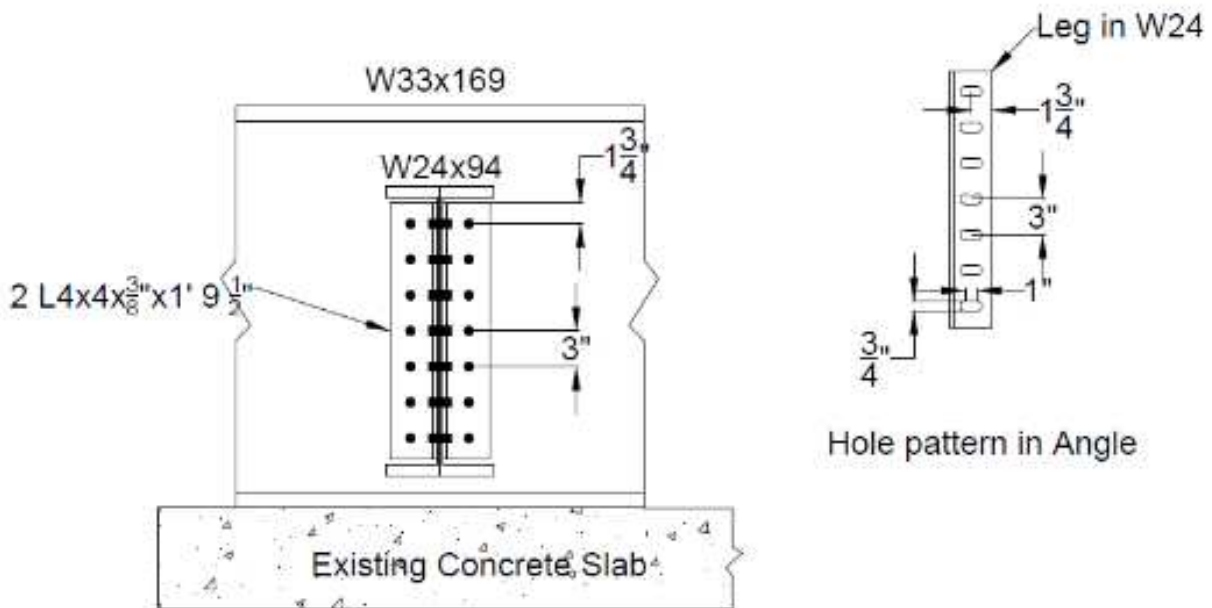


Figure 68. W24x94 and W33x169 beam connection

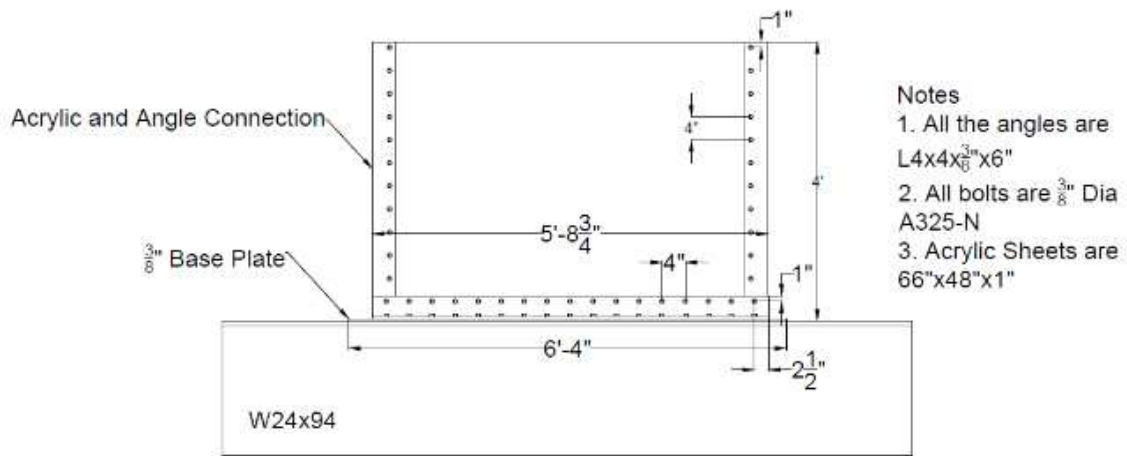


Figure 69. Bottom W24x94 beam and acrylic tank connections

Appendix C

Calculations for Paris Law Constants for Specimen 1

British Standards (BS 7910:1999) give an equation for ΔK for CCT as follows:

$$\Delta K = Y \Delta \sigma \sqrt{\pi a} \quad C1$$

And

$$Y \Delta \sigma = M \times F_W \times M_m \times \sigma_{max} \quad C2$$

Where for through thickness center crack,

$$M = M_m = 1 \text{ and}$$

$$F_w = \left(\sec \frac{\pi a}{W}\right)^{0.5} \text{ here } W \text{ is the width of the plate (1 m)}$$

Paris law is only applicable to cracks obeying linear elastic fracture mechanics laws. Crack showed stable propagation until 250 mm. First few data points were neglected as the tensile residual stresses from the tack welds are affecting this data.

A da/dN versus ΔK scatter was generated for both half crack lengths and linear trendlines along with their equations were obtained for this scatter. As mentioned before, Paris law constant 'C' is the y-intercept of these linear trendlines and 'm' is the slope.

Sample calculations for this study are tabulated in Table.

Table 8. Sample calculations for ΔK for west half crack length of specimen 1

$\Delta \sigma$ (MPa)	Number of cycles 'N'	Change in number of cycles 'dN'	Half crack length 'a' (m)	Change in half crack length 'da'	da/dN	F_w	ΔK (MPa $m^{1/2}$)
55.15	146623	-	0.0908	-	-		
55.15	181118	34495	0.0938	0.003	8.6969×10^{-8}	1.022	30.61036672

List of Abbreviations

ΔK_{eff} = Effective range of stress intensity factors

ΔK_{th} = Change in Stress intensity factor Threshold

ΔK = Range of stress intensity factor

a = Half the crack length

C = Material constants

da = Change in crack length

dN = Change in Number of Cycles

E = Modulus of Elasticity

F_c = Crack shape factor

F_g = Non-uniform stress factor

F_s = Crack surface factor

F_w = Finite width factor

G = Energy Release Rate

K = Stress intensity factor

K_c = Fracture Toughness

K_{max} = Maximum Stress Intensity Factor

K_R = Residual stress intensity factor

m = Material constants

N = Number of cycles

N_T = total number of cycles

R = Minimum load to maximum load ratio

R^{eff} = Effective stress ratio

R_y = Extent of yield zone

y = Wheeler shape factor

Z_{OL} = Overload plastic zone size

γ_w = Walker's Parameter

ΔK_i = stress intensity factor range for i^{th} cycle

ΔK_{rms} = Root mean square value of stress intensity factor range

σ = Nominal stress

σ_{max} = Maximum Nominal Stress

σ_{min} = Minimum Nominal stress